AERODYNAMIC FORCE AND PRESSURE LOSS MEASURMENTS ON LOW ASPECT RATIO PIN FIN ARRAYS

Alan A. Thrift

Thesis submitted to the Faculty of the
Virginia Polytechnic Institute and State University
in partial fulfillment of the requirements for the degree of

Master of Science
In
Mechanical Engineering

Dr. K.A. Thole, Chair
Dr. M.R. Paul
Dr. C.L. Dancey

February 9, 2007
Blacksburg, VA

Keywords: pin fin, cylinder drag, lift, force measurement, pressure drop, internal cooling

AERODYNAMIC FORCE AND PRESSURE LOSS MEASURMENTS ON LOW ASPECT RATIO PIN FIN ARRAYS

Alan A. Thrift

Abstract

The desire to achieve higher heat transfer augmentation for turbine blades is fueled by the increased power output and efficiency that is achievable with high turbine inlet temperatures. The use of internal cooling channels fitted with pin fin arrays serves as one method of accomplishing this goal. Consequently, the addition of pin fin arrays comes at the expense of increased pressure drop. Therefore the pin fin geometry must be judiciously chosen to achieve the required heat transfer rate while minimizing the associated pressure drop.

This project culminates in the measurement of both pin fin force and array pressure drop as they related to changes in the array geometry. Specifically, the effects of Reynolds number, spanwise pin spacing, streamwise pin spacing, pin aspect ratio, and flow incidence angle. Direct two-component force measurement is achieved with a cantilever beam force sensor that uses highly sensitive piezoresistive strain gauges, relating the strain at the base of the beam to the applied force. With proper characterization, forces as small as one-tenth the weight of a paper clip are successfully measured. Additionally, array pressure drop measurements are achieved using static pressure taps.

Experiments were conducted over a range of Reynolds numbers between 7,500 and 35,000. Changes in the spanwise pin spacing were shown to substantially alter the pin fin drag and array pressure drop, while changes in the streamwise pin spacing were less influential. The experimental results also showed a dramatic reduction in the pin fin drag and array pressure drop for an inline flow incidence angle. Finally, changes in the pin aspect ratio were shown to have little effect on the array pressure drop.

Preface

The following thesis is presented in a paper format so that it can be subject to acceptance into a conference or journal. The paper is outlined in a traditional format with an introduction and literature review, followed by a description of the testing facility and the testing methodologies as well as the data reduction techniques employed. Next, a presentation of the experimental results is given, and finally, a summation of the experimental work is offered in the conclusions along with a comparison to heat transfer trends obtained from a parallel project. The supporting appendices are presented last.

Acknowledgements

I would like to express my sincere gratitude to Dr. Karen Thole for providing me the opportunity to work as part of her research lab. In the midst of a new place and surrounded by unknowns it is easy for a young student to lose focus or feel dwarfed by the project at hand. Karen provided a stable horizon for me, always letting me know I belonged and that any expectation can be surpassed. For these things I am grateful and I look forward to working with her in the future as I continue to grow both as a student and a person.

I must also express my gratitude to Pratt and Whitney for the research opportunity they provided. I would like to especially thank Atul Kohli for his support of my work.

To each one of my labmates, I would like to say thank you for your comradery, the relationships I have built with many of you will no doubt last a lifetime. Mike B., Steve, Nick, Joe, Will, Sundar, Cam, Eric, Mike L., Seth, Jason, Scott and Paul have all made my stay in Blacksburg enjoyable. I need to especially thank Scott Brumbaugh for the patience and kind hand he extended toward me when I first arrived at Virginia Tech. His development of the testing methods used during this project were truly unique and his thoughtfulness to aid me so diligently in understanding his work during the time he was writing his thesis is something I will always be in debt to him for. I must also think my good friend, Seth Lawson. With many hours in the lab we have forged a brotherhood that will no doubt continue to grow as we pursue our doctoral degrees. In the not so distance future I imagine that the slight awkwardness we experience by referring to each other has brothers, will all but have disappeared.

To every one in my family, I would like to say that I love you and that your faces were never far from my thoughts. Doll, Grandmaw, Tommy, Donna, Bryan, Aunt Patty, Uncle Eric, Erica, Richard, Aunt Phyllis, Curtis, Miranda, Jennifer, Chad, Kane, and Kaela have all made my trek away from home difficult, but their support is what has made it possible.

In particularly, I would like to thank both of my parents who sacrificed selflessly to afford me the opportunity to succeed in life. As scared as I'm sure they both were when my OCD truly had a strangle hold on my life, they never gave up on me or gave me the impression for a moment that I wouldn't grow up to do extraordinary things. Their investment then will not go wanting, I promise them that.

Contents

Nomenclature

C_D	= Drag coefficient (no subscript indicates value based on mass averaged velocity through the open channel, U)
C_L	= Lift coefficient based on mass averaged velocity through the open channel
d	= Diameter of the sensor pin fin (a subscript indicates the DSC-6 calibration constant (V/V-kg-cm) pertaining to a particular axis, x or y)
dp	= Pressure drop across orifice / venturi flow meter
D	= Orifice / venturi bore diameter
D_H	= Channel hydraulic diameter
f	= Darcy friction factor, vortex shedding frequency
f_{array}	= Array friction factor
F_D	= Aerodynamic drag force
F_L	= Aerodynamic lift force
g	= Acceleration due to gravity, 9.81 m/s²
GF	= Sensor gage factor
H	= Channel height (pin height within the channel)
K	= Orifice / venturi flow coefficient
L	= Total distance between static pressure measurement locations and the array
m	= Mass
n	= Total number of measurements within a set
N	= Number of streamwise rows in an array
Nu	= Nusselt number based on endwall area average
P	= Pressure
Q	= Volumetric flow rate

R = Electrical resistance

Re = Channel Reynolds number (no subscript indicates value based on channel hydraulic diameter, D_H, and mass averaged velocity through the open channel, U)

S1 = Distance between pin fin centers in the spanwise direction

S2 = Distance between pin fin centers in the streamwise direction

T = Temperature

u = Uncertainty

U = Velocity (no subscript denotes mass averaged velocity through the open channel)

V = Voltage

W = Channel width

x = Linear distance in the channel axial direction

Y = Orifice / venturi expansion coefficient

y = Linear distance in the channel traverse direction

Greek:

α = Flow incidence angle

β = Linear least squares regression slope

Δ = Difference in the subsequent quantity

δ = Distance of applied force from DSC-6 beam tip; defined to be positive towards the base of the sensor, negative away from the base of the sensor

μ = Dynamic viscosity, average

ρ = Density

ξ = Cross axis correction coefficient for the x-axis of the DSC-6

ψ = Cross axis correction coefficient for the y-axis of the DSC-6

Subscripts:

0	= Based on an unobstructed channel
array	= pressure measurement across a pin fin array
avg	= Average value of a set
ABS	= Absolute pressure
ATM	= Atmospheric pressure
c	= Cross axis corrected voltage
corr	= Nulled voltage with respect to no load voltage
d	= Indicates Reynolds number based on sensor pin fin diameter and mass averaged velocity through the minimum channel area, U_{max}
e	= Excitation voltage
i	= Individual measurement value within a set
I	= Induced voltage
j	= Individual mass application within a set
L	= Line absolute pressure or temperature
max	= Based on mass averaged velocity through the minimum channel area
measured	= Directly measured pressure drop
median	= median value of a set
o	= Raw output voltage
pins	= Diameter of pin fins
x	= Streamwise direction
y	= Spanwise direction
zero	= No load voltage

List of Tables

List of Figures

Introduction

One feature common to all modern gas turbine engines is that the main gas path temperatures past the combustor are higher than the melting temperatures of various engine components; most importantly the first few blades of the turbine section. Specifically gas temperatures can be around 1650ºC at the turbine inlet, while typical turbine blade and vane materials will melt at 1300ºC. Even if the blades are cooled to temperatures below the melting point, the extreme temperatures still affect the life of the blades. In fact blade temperatures that deviate above the design temperature by just 15ºC can half the service life of the blade. Consequently, gas turbine airfoils must be cooled both internally and externally, particularly for those blades and vanes located within the first few stages of the turbine section.

External cooling is achieved through film cooling holes on the surface of the airfoil while internal cooling is achieved with intricate flow passages within the airfoil. In both cases the coolant air is extracted from the compressor section of the gas turbine engine as to take advantage of the high gas pressures and relatively low gas temperatures. The internal cooling channels used to transport the coolant within the airfoils are rarely simple, open channels. Often, obstructions are added within the channels to promote turbulence and heat transfer. Arrays of circular cylinders, or as they are more commonly referred to as pin fins, spanning the entire height of the internal channels are a common device used to promote enhanced heat transfer. However, a price is paid for the increased heat transfer in the form of pressure loss. The pressure drop required by an array of pin fins places increased demand on the inlet supply pressure requirements.

Presently, most pin fin arrays are designed with correlations developed for an array of uniform pin spacing. However, a uniform array of pin fins may not be the optimal configuration for every cooling situation. This is evident in those circumstances where the airfoil is subject to intense, localized heat flux. Using an array of uniformly spaced pin fins having the same geometry, requires the entire array to be designed to accommodate the intense heat flux that is only present in a local area. Often, this leads to over-designed cooling systems that suffer from unnecessarily large pressure drops. A potential solution to the over-design problem is to use customized pin fin arrays that are not necessarily uniform. As such, the pin fin arrays could be arranged to remove a large heat flux in the localized area while providing a sparser pin fin

configuration where the cooling requirements are not as severe. This would also result in a variable flow distribution through the pin fin array.

With a non-uniform array of pin fin sizes and spacing, predicting the flow distribution in the array is very difficult. Even using CFD, it is problematic because of the intense computational requirements due to the complex geometries. An alternate approach is to develop predictive tools which utilize knowledge of the lift and drag forces experienced on a single element within the array.

The work presented in this paper is to provide a better understanding of not only the pressure drop through a pin fin array as it is related to different array geometries, but also the drag and lift force experienced by an individual pin fin. The results presented in this paper are for a range of spanwise pin spacings between 2 and 12 pin diameters for both single and multiple row pin fin arrays. In the case of multiple row arrays, the rows were staggered. Pin aspect ratios, ratios of height-to-diameter, ranged from 0.5 to 1. Additionally, the effects of streamwise pin spacing are considered in multiple row arrays for spacings of 1.73 and 3.46 pin diameters. Reynolds numbers, based on pin diameter and the minimum free flow velocity, ranged as high as 34,000 and as low as 4200. The remainder of this paper documents the conclusions regarding pressure drop and drag from the relevant literature, provides a description of the test facility and testing methodology, presents the pressure drop and force results and supporting flow visualizations and, finally, presents comparisons between pressure drop and heat transfer trends.

Review of Relevant Literature

The heat transfer and pressure drop augmentation associated with flow normal to pin fin arrays is a subject of great significance based on the importance of cooling within many of today's engineering applications. The most imperative of these is convective internal cooling within gas turbine airfoils as the hot gasses passing over the blades tend to exceed the melting temperature of the constituent metals. Due to blade size and manufacturing constraints these pin fins ordinarily have height-to-diameter ratios in the range of 0.5 to 4 [1]. Since the most intense increase in heat transfer through pin fin arrays is associated with turbulent flow, there are no analytical solutions that exist which can accurately predict the heat transfer or pressure drop for actual operating flow conditions. As a result, several experimental and numerical studies have been conducted by numerous researchers to investigate how the heat transfer and pressure drop

augmentation provided by pin fin arrays changes with array geometry and flow condition. While the target outcome is an increase in overall cooling there is an inevitable penalty in the form of pressure loss.

This review will provide discussions on the effects of pin spacing, pin aspect ratio, and Reynolds number as they are related to array pressure drop in the form of a friction factor and row-by-row pin fin drag in the form of a drag coefficient. While experimental techniques for measuring pressure losses are well developed and accessible, the same cannot be said for the current methods of making force measurements, especially when the subject of interest is a pin fin confined in a channel. Consequently, there are substantially more research papers within today's available scientific literature devoted to obtaining array pressure drops than pin fin drag measurements.

Effects of Array Geometry on Pressure Drop

The available literature on pressure loss in pin fin arrays suggests that decreasing the spanwise pin spacing and increasing the streamwise pin spacing both correspond to an increase in the pressure drop through a pin fin array, with the effects of spanwise pin spacing being more dominant than streamwise pin spacing. Additionally, the effects of streamwise pin spacing become less significant with increasing spanwise pin spacing, specifically above a spanwise pin spacing of 2 and below a streamwise pin spacing 3 [2].

For staggered, long tube arrays in external cross flow, Zukauskas [3] and Jacob [4] reported that reducing the spanwise pin spacing increases the pressure drop while changes in the streamwise pin spacing have little effect. Similarly, for a staggered pin fin array with a pin aspect ratio of 1 and a spanwise pin spacing of 2.5, Metzger et al. [5] reported that the pressure losses are relatively insensitive to streamwise pin spacing over a range of 1.05 to 5. Metzger et al. [5] also found that their results were reasonably predicted by the established correlation for long tube arrays by Zukauskas [3] over a range of spanwise to streamwise pin spacing ratios of 0.5 to 2.38.

Peng [6] studied the combined effect of simultaneously increasing equal spanwise and streamwise pin spacings from 2 to 4 with pin aspect ratios of 4 and 6. Peng [6] showed the effect that simultaneously increased spanwise and streamwise pin spacings have little influence on pressure drop. Although Peng [6] studied larger pin aspect ratios, his data agree quite well with

the correlation provided by Metzger et al. [5] for pressure losses. While both researchers predict slightly larger pressure drops than those for long tube arrays, the differences become smaller with decreasing spanwise pin spacing. Similar to Zukauskas [3] and Jacob [4], Damerow et al. [7], who studied the effect of various spanwise pin spacings above 4.24 for pin aspect ratios ranging from 2 to 4, showed that the pressure loss through a staggered pin fin array increases with decreasing spanwise pin spacing. The increasing effect was more significant than for long tube arrays. The Damerow et al. [7] correlations predict results that are well above the correlation of Metzger et al. [5] and the long tube correlation of Jacob [4]. The differences between these correlations are much smaller when Damerow's correlation is evaluated at those spanwise pin spacings above 4.

Hamilton et al. [2] computationally modeled a staggered pin fin array with a pin aspect ratio of 1. Hamilton et al. [2] varied the spanwise and streamwise pin spacings independently from one another over a range of spacings from 1.25 to 3 with his results indicating an increase in pressure drop with decreasing spanwise pin spacing. Contrary to those trends observed in long tube arrays and by Metzger et al. [5] for short pin fins, the results of Hamilton et al. [2] indicated increases in pressure losses with increases in streamwise pin spacings. They reported the effects being less pronounced at the larger spanwise pin spacings, in fact, the differences in pressure loss at the largest spanwise pin spacing of three were insignificant among those streamwise pin spacings below 3. Interestingly, Metzger et al. [5] who reported that the pressure losses were relatively insensitive to streamwise pin spacing, stated that their data were correlated to within ±15%. With such a large bound on their correlation, at the spanwise pin spacing they studied, the effects of streamwise pin spacing on pressure losses may have been undetectable. Similar to Peng [6], Hamilton et al. [2] showed little difference in pressure drop at simultaneously increasing but equal spanwise and streamwise pin spacings. This observation is likely explained by the tradeoff in pressure loss associated with increasing both spanwise and streamwise pin spacing, where the former decreases the pressure drop and the latter increases the pressure drop as predicted by Hamilton et al. [2].

Regarding inline and staggered pin fin arrays, data from the available literature suggest that the inline array causes a much smaller pressure drop than the staggered. For long tube arrays, Zukauskas [3] and Jacob [4] reported that there is a considerable decrease in pressure drop associated with an inline array and that the effect is amplified with an increase in the

streamwise pin spacing. For a pin aspect ratio of one and equal spanwise and streamwise pin spacings of 2.5, Chyu [8] reported that the pressure drop associated with an inline array is smaller by a factor of nearly two as compared to a staggered array. For the same pin aspect ratio and spanwise pin spacing as Chyu [8] but with a streamwise pin spacing of 1.5, Metzger et al. [9] reported a decrease in pressure loss of approximately 27 percent for a staggered pin fin array that is angled to the flow such that it appears nearly inline to the incoming flow as compared to the non-angled arrangement. Again by angling the staggered pin fin array so that it is inline to the incoming flow for a pin aspect ratio of nine having a spanwise pin spacing of 2.06 and 1.46 and a streamwise pin spacing of 1.03 and 1.46, Evenko and Anisin [10] reported a pressure drop decrease of approximately 26 and 15 percent relative to the respective non-angled cases.

The available literature suggests that increasing the pin aspect ratio from unity has little influence on the pressure drop through a staggered pin fin array [11]. Data by both Metzger et al. [5] and Peng [6] appear to be well-predicted by correlations developed by Jacob [4] for long tube arrays indicating that the pressure drop has little dependence on the pin aspect ratio. Damerow [7] also found that his data had no dependence on the pin aspect ratio.

While all researches report that the non-dimensional pressure drop decreases monotonically with Reynolds number, there is still some variability among researchers concerning the exact Reynolds number dependence of the pressure drop associated with pin fin arrays. Relative bounds can be placed on the range of the Reynolds number exponent by comparing pressure losses through a long tube array with that of an unobstructed rectangular duct. For a turbulent duct, Kakac et al. [12] reported a channel Reynolds number exponent of -0.3 but indicated a slightly weaker Reynolds number dependence with exponent -0.25 at higher Reynolds numbers. For staggered long tube arrays, Jacob [4] reported a single pin Reynolds number exponent of -0.16, predicting a much lower influence on pressure losses than for duct flow. For an inline long tube array, Jacob [4] reports a reduction in the pin Reynolds number exponent to -0.15.

Damerow [7] found that his data for spanwise pin spacings above 4.24 and for pin aspect ratios ranging from 2 to 4 were well-correlated using the same Reynolds number exponent as Jacob [4] for staggered, long tube arrays. Similar to Kakac et al. [12], Metzger et al. [5] also reported a change in Reynolds number dependence but indicated the transition occurring at a much lower Reynolds number. Metzger et al. [5] showed an increase in Reynolds number

dependence instead of a decrease with an exponent increase from -0.132 to -0.318 at a pin Reynolds number of 10,000.

Effects of Array Geometry on Drag

While no row-by-row drag force data is available in the literature for multiple row arrays, there are detailed results regarding row-by-row static pressure distributions around an individual pin fin [13]. Integration of such static pressure distributions yield the pressure drag force but do not include the viscous drag. It is well known that the drag on a single infinitely long circular cylinder in external crossflow has a ratio of viscous drag to total drag that decreases rapidly with increasing Reynolds number. It is probable that at the Reynolds numbers associated with internal turbine blade cooling that the viscous drag makes up an insignificant portion of the total drag given the confined channel arrangement.

Ames et al. [13] made detailed static pressure measurements about the midline of an individual pin fin in each of the first five rows within an eight row staggered pin fin array. The pin aspect ratio was two and the array had an equal spanwise and streamwise pin spacing of 2.5. Integration of their published pressure coefficients yields the pressure drag coefficient. Their data shows two separate trends with Reynolds number indicating that the flow is developing within the first few rows and becoming fully developed within the subsequent rows. For the low Reynolds number regimes ($Re_d < 10^4$) the pressure drag in the first five rows appears to be similar except for the first row, where it is lower. With increasing Reynolds number the pressure drag coefficient in the first and second rows exhibit a slight positive slope with the first row pressure drag always being lower. In the subsequent rows, however, the pressure drag coefficients are similar in value and show a decrease with increasing Reynolds number. Some caution should be taken in the observed trends predicted by the pressure drag coefficients since the values were obtained from pressure distribution measurements around the midline of the pin fin. However, Ames and Dvorak [14] reported that the pressure distribution is essentially uniform along the span height of the channel for the pin fin with respect to the midline pressure.

Kakac et al. [12] reported the pressure drag coefficient as a function of Reynolds number for a long tube in the inner rows of a staggered array with an equal spanwise and streamwise pin spacing of 2. The pressure drag coefficient decreased with increasing Reynolds number similar to that found by the investigation of Ames et al. [13] pressure distribution data.

Regarding the difference between the drag on a long tube within a staggered and inline array, Kakac et al. [12] reported a considerable decrease in the pressure drag coefficient. These results lead to the deduction that the total drag will also be considerably lower on a pin fin within an inline array than a staggered array. This conclusion is also supported by the pressure drop trends previously discussed.

Due to the lack of available literature on the drag force of a multiple row array, there are no assessments that can be made has to the effects of spanwise and streamwise pin spacing or pin aspect ratio. Additionally, the work of Ames et al. [12] can only be interpreted to provide limited insight into the row-by-row drag of a multiple row array in channel flow. This research is unique, in that it will fill a void left by the pin fin studies discussed above as the literature review did not yield any studies that quantified total drag or lift on a pin fin in channel flow. This paper will present trends in pin fin drag and lift as related to Reynolds number, spanwise pin spacing in a single row array, and row number within a multiple row array

Experimental Test Facilities and Measurement Methodologies (Pressure and Force)

Experimental testing was performed in order to obtain non-dimensional array pressure drop, friction factor, and pin fin force, drag and lift coefficient, data. The goal was to observe the influence of Reynolds number, pin aspect ratio, spanwise pin spacing, streamwise pin spacing, and flow incidence angle on these two parameters.

To measure the aerodynamic forces on a single pin fin within an array as well as measuring the static pressure drop across a pin fin array in a high aspect ratio channel required a specialized test facility. While using static pressure taps to measure pressure drop is a readily understood technique, the task of making force measurements on a single pin fin constrained by the boundaries of the channel floor and ceiling is much more difficult. First, the pin fin had to be decoupled from the channel walls so the deflection of the pin fin could be related to the applied forces. It was important that the decoupling take place without changing the flow dynamics around the pin fin. Additionally, the difficulty of the technique was compounded by the intricate sensitivities of the chosen force sensor. The development of the test facility and the force sensor, including characterization and calibration, along with the methodology used for making pin fin force measurements were accomplished by a previous student [15]. The following sections

describe the test facility where the pin fin force and array pressure drop measurements were made, along with a detailed description of the chosen force sensor, how it works, and the important testing considerations.

Experimental Test Facility

The testing facility was designed to operate in a closed loop, recirculating flow configuration. Figure 1 provides a schematic representation of the test facility, highlighting the four major components including the following: plenum, test section, flow measurement section, and flow recirculation section. The flow follows a clockwise path as indicated by the arrows. To ensure acceptable resolution of pin fin force measurements it was necessary that the pin fin geometries be scaled up from actual engine size. The scaling of the pin fin geometries governed the size of the test section and therefore the test facility has a whole.

The plenum in Figure 1, which had a flow area relative to the test section of 110:1, contained a two plate baffle used to evenly distribute the entering jet of air over the entire plenum cross sectional area. The first plate encountered by the flow was a splash plate while the second plate was a hollow rectangle, through which the air passed through the center. The flow next entered the tube and fin heat exchanger, which was used to maintain a steady inlet air temperature into the test section. Finally before entering the test section, the flow encountered rounded inlets constructed from large PVC pipes that were halved in order to provide a smooth contraction for the entering flow.

Downstream of the test section, the flow exited into an extension that transitioned from the rectangular test section to the circular pipe of the flow measurement section, increasing three-fold in flow area during the transition. The circular pipe was fed into one of two interchangeable flow meters including either a venturi or orifice of which combined with the appropriate sized pressure transducers provided proper measurement of the volume flow rate. The flow measurement section was designed with 15 hydraulic diameters of pipe upstream of the flow measurement device and nine hydraulic diameters extending downstream to the entrance of the blower. This configuration provided ample upstream and downstream extension of the smooth circular pipe as specified by the manufacturer. To circulate the air through the test facility an 11.2 kW, 3-phase electric motor having a variable frequency drive was used to power the blower that provided the required pressure difference.

The air then flowed from the blower outlet back to the plenum through the flow recirculation section consisting simply of circular pipe and a butterfly valve. Also shown in Figure 1 are two regulator valves, each available to be open to atmosphere, with one located slightly upstream of the blower and the other downstream of the blower but upstream of the butterfly valve. This arrangement of valves was used to adjust the flow such that the absolute pressure in the test section could be balanced with the atmospheric pressure when necessary.

Test Section

The test section, where all drag force and pressure drop measurements were made, was designed as a parallel plate channel. The channel was 1.33m long, with an open flow area of 61 cm wide by 0.96 cm high giving a width to height ratio of 64:1. The height and width of the channel were constrained by the requirements discussed in the previous section while the test section length was constrained by a combination of the desired pin fin array and flow uniformity requirements. The parameters used in describing the geometry of a staggered pin fin array are illustrated in Figure 2

Figure 3 provides a schematic representation of the test section. The channel floor was constructed from a single Lexan plate while the ceiling was constructed of two separate Lexan plates to allow for installation of the force sensor and assembly to the plenum. The ceiling and floor of the test section were separated by a spacer on each side. Through holes with counterbores were machined into the floor plate and the downstream ceiling plate to provide a clearance hole for the force sensor pin fin through the channel. Pressure taps were also placed in the ceiling plates to obtain static pressure measurements throughout the channel. The pressure taps were constructed from brass tubing with the flow end of the pressure tap beveled and mounted flush with the inner surface of the channel ceiling. Appendix A provides further details on the locations of the pressure taps.

The force sensor assembled to the test section floor via an adjustable mount bolted to the bottom side of the plate. A Lexan cup, painted black to shield the sensor from light, encompassed the force sensor and the mount such that the force sensor could be submerged in a silicone oil bath and so that the clearance gap between the force sensor pin fin and the test section floor could be filled with silicone oil. Silicone oil was fed into the reservoir cup by emptying a plastic bottle, filled with silicone oil, connected by tubing to the reservoir cup. The

silicone reservoir on top of the channel ceiling was achieved with the counterbore in the downstream Lexan ceiling plate. For a more thorough description of the test facility with all accompanying mechanical parts drawings as well as all test facility component data sheets reference Brumbaugh [15].

Channel Benchmarking

Two requirements were imposed upon the flow in the test section before reaching the pin fin array. The velocity profile of the channel flow had to be hydrodynamically fully developed and the flow needed to be uniform across the width of the channel. Spanwise static pressure uniformity ensured that the spanwise velocity was consistent across the width of the test section.

Hydrodynamic development in the test section was evaluated by measuring pressure distributions along the channel and comparing the Darcy friction factor over a range of flow conditions to known correlations. The Darcy friction factor represents a non-dimensional static pressure loss for a given channel length when normalized with the average unobstructed channel velocity. For hydrodynamically, fully developed flow conditions, the Darcy friction factor is constant, meaning the static pressure drop is linear with respect to channel distance in the streamwise direction. For the case of turbulent flow analytical solutions for the friction factor do not exist so empirical correlations must be referenced in order to predict the friction factor in the channel. Kakac et al. [12] provides Fanning friction factor correlations for turbulent flow in a rectangular duct, as in the case of this test channel, which are related to the Darcy friction factor by a multiple of 4. Equations 1 and 2 provide these correlations as Darcy friction factors.

$$f = \frac{0.5072}{\mathrm{Re}^{0.3}} \qquad \text{for } 5{,}000 \leq \mathrm{Re} \leq 30{,}000 \tag{1}$$

$$f = \frac{0.3472}{\mathrm{Re}^{0.25}} \qquad \text{for } 12{,}000 \leq \mathrm{Re} \leq 120{,}000 \tag{2}$$

Kakac et al. [12] state that Equation 1 is preferable to Equation 2 for those flows in the overlap region of $12{,}000 \leq \mathrm{Re} \leq 30{,}000$.

Figure 4 plots the measured friction factor for the test channel over a range of channel Reynolds numbers and compares these values to the correlations. The measured friction factors

showed agreement with the published correlations to within 2.5%. This supported the conclusion that the flow is fully developed and that the desired channel flows are in place. From the onset of the linear pressure drop, indicating a hydrodynamically, fully developed flow, it was determined that the flow became developed approximately 26 hydraulic diameters into the test channel. The smallest entrance length encountered during force and pressure drop testing was for the array with S1/d = 4, S2/d = 3.46, 7 row, staggered configuration angled at 30° to the incoming flow with the force sensor pin fin located in the fifth row. The entrance length in this case was 28 hydraulic diameters, which is still greater than the required entrance length for development

The second channel benchmarking was achieved by examining the spanwise pressure uniformity upstream of the pin fin array before each series of pin fin force or pressure drop measurement tests. For a single row of pin fins and for a non-angled pin fin array the upstream static pressure across the width of the test channel never varied by more than 2.5% from the average upstream static pressure, when normalized by the dynamic pressure head. Figure 5 provides a typical plot of the upstream spanwise static pressure distribution for four different flow conditions. The plot shows that all four cases fall within the 2.5% criterion and that the pressure distributions appear random across the span. For an angled pin fin array however this was not the case since the flow is affected by the non-symmetric obstruction. In this situation the upstream static pressure distribution is necessarily non-uniform across the span since the flow is incompressible and must begin accommodating for the downstream obstruction prior to reaching it. For arrays angled at 30º to the incoming flow the variation from the average upstream static pressure could be as large as 11% when normalized with the dynamic pressure head. For a more detailed explanation on how empty channel friction factor and spanwise pressure uniformity measurements were made see Appendix A.

General Description and Operation of the DSC-6 Force Sensor

The selection, characterization, and calibration of all force sensors were performed by Brumbaugh [15]. The technique made use of an elastic measuring device, which is a Kistler Morse DSC-6 sensor, whose output voltage was proportional to the applied force and was capable of two axis force measurements. A total of ten DSC-6 sensors were purchased in support of this research. Two single axis sensors were ordered for the purpose of exploring the

behavior of the DSC-6 and eight dual axis sensors were ordered for conducting pin fin force measurement tests. Appendix B gives further details on the specific sensors. While several force sensors were used during calibration and investigation of the DSC-6 force sensors behavior, only one sensor was used for obtaining pin fin force measurements.

The DSC-6 force sensor had a full scale force limit of 2.45 N and made use of a cantilever beam as shown in a dimensioned diagram in Figure 6. The sensor cantilever beam is constructed of 17-4 precipitation hardened stainless steel. The sensor pin fin is threaded onto the sensor using 2-56 UNC-2A threads tapped in the end of the cantilever beam. A counterbore through hole at the base of the sensor allows the sensor to be rigidly secured to a stationary mount.

The DSC-6 force sensor detects the applied force by measuring the induced strain at the base of the cantilever beam, 2.54 cm from the end of the beam, where two pairs of semi-conductor strain gauges are located 90° apart from each other. Each strain gauge pair consists of two gauges located 180° apart from each other. The strain gauge pairs, each pair corresponding to one axis of sensitivity, are encapsulated in silicone rubber for protection. The pair of gauges forms what is commonly known as a half bridge, type II Wheatstone Bridge. In this configuration, bending in one direction places one strain gauge in a pair in compression while the other gauge is symmetrical loaded in tension. These bending stresses result in an equal and opposite resistance change within the pair of strain gages, unbalancing the bridge and causing a voltage potential across the circuit bridge. Equation 3 provides the relationship that is published by Kistler Morse [16] to relate the DSC-6 force sensor output voltage to the applied force.

$$F = \frac{V}{V_e} \frac{g}{d(2.54-\delta)} \tag{3}$$

Here, V_e represents the excitation voltage applied to the Wheatstone bridge, while V represents the output voltage across the bridge for a given axis. The term $(2.54 - \delta)$ is identified as the effective cantilever beam length of the force sensor where the distance from the end of the sensor beam, δ, is defined to be positive towards and negative away from the base of the beam. A single constant of proportionality, d, contains the influences of the strain gauge factor and the cantilever beam mechanical properties. The gravitational constant ,g, converts the force from

kilograms to Newtons. From Equation 3 it can be seen that the constant of proportionality has units of V/V·kg·cm.

Although Equation 3 can be used to ideally describe the output of the DSC-6 force sensor, the voltage ratio (V/V_e) must be corrected for cross axis effects. Cross axis effects mean the output voltage of one axis is affected by the loading on the perpendicular axis. The cross axis-phenomenon was unexpected, as it theoretically should not exist and is not documented by the manufacturer. This effect was identified while studying the output voltage from both sensor axes during calibration testing where one axis is loaded parallel with gravity leaving the other axis perpendicular to gravity. The perpendicular axis should have theoretically had zero voltage output, as there was no loading in that direction. Figure 7 plots the output voltage ratio of the perpendicular axis to the gravity aligned axis for both sensor axes for two different DSC-6 force sensors. The results of Figure 7 show that a voltage was indeed still produced in the perpendicular axis.

Two key observations can be made from Figure 7. First, the cross axis sensitivity is not consistent between force sensors, or even between axes on the same force sensor. Second, the ratio of the output voltage in the perpendicular axis to the gravity aligned axis is very nearly constant for a given sensor axis. Inspection of Figure 7 shows that that this is true except below an applied force of approximately 5×10^{-3} N. This corresponds to a voltage output on the order of 1×10^{-6} V in the perpendicular axis, which due to insufficient measurement resolution leads to the apparent ratio change at the low forces.

A voltage output of 1×10^{-6} V is approximately 2 orders of magnitude smaller than any voltages measured by the DSC-6 force sensor during testing so the assumption that the output voltage ratio is constant is applicable. This suggests that the cross-axis effects can be nulled by subtracting a fraction of the aligned axis' output. Equation 4 provides an equation for the linear correction of the cross axis effects in the force sensor x and y axes.

$$\begin{aligned} \text{X-axis:} \frac{V_{cx}}{V_{ex}} &= \frac{V_{ox}}{V_{ex}} - \xi \frac{V_{oy}}{V_{ey}} \\ \text{Y-axis:} \frac{V_{cy}}{V_{ey}} &= \frac{V_{oy}}{V_{ey}} - \psi \frac{V_{ox}}{V_{ex}} \end{aligned} \tag{4}$$

Here, the corrected voltage ratio for a given axis is represented as V_c/V_e and the raw voltage ratio as V_o/V_e. The cross-axis correction coefficients, ξ and ψ, can be experimentally determined from calibration testing. Equation 5 provides the definition of ξ and ψ.

$$\xi = \frac{V_{Ix}/V_{ex}}{V_{oy}/V_{ey}} \qquad \psi = \frac{V_{Iy}/V_{ey}}{V_{ox}/V_{ex}} \tag{5}$$

Here, V_{Ix} represents the voltage induced in the x-axis when a load is applied solely to the y-axis. Conversely, V_{Iy} represents the voltage induced in the y-axis when a load is applied solely to the x-axis. It can be seen from Equation 5 that the ξ and ψ coefficients represent the voltage induced in the unloaded respective sensor axis as a percentage of the voltage in the loaded perpendicular axis. The corrected voltage ratios provided by Equation 4 are the values that should be substituted into Equation 3 to calculate the applied force. While the cross-axis correction coefficients are different between sensor axes, no sensor axis was found to require a voltage offset of more than 13% of the induced voltage in the opposed axis.

The DSC-6 force sensor is sensitive to several environmental factors including temperature and light exposure, but with proper control of these factors the force sensor can be expected to function as intended with an unloaded drift rate of less than 0.25% per minute of the smallest drag force measured on a single pin fin during testing when the sensor axis bridges are supplied with 2 volts of excitation, V_e in Equation 3. For a detailed explanation of the influencing environmental factors and there affects see Appendix B.

Data Acquisition and Methodology

Selection of an adequate data acquisition system was an important aspect of developing the force measurement methodology. The signal conditioning equipment must be able to provide: a stable excitation voltage to the Wheatstone Bridge, precision resistors to complete the static arm of the Wheatstone Bridge, and a potentiometer to balance the Wheatstone Bridge.

The signal conditioning system used was a National Instruments SCXI 1520. This system was able to provide a Wheatstone Bridge balance range of ± 4% of the excitation voltage. Bolted to the front of the SCXI 1520 was a SCXI 1314 terminal block which allowed for the connection of the DSC-6 force sensor. The SCXI 1520 signal conditioner and the SCXI 1314 terminal block were both housed in the SCXI 1000 chassis. The DSC-6 force sensor is connected to the SCXI signal conditioning equipment via Alpha 6010C Sl005 cable. Each sensor axis requires its own individual cable meaning that there are two cables for each dual axis sensor. Within a single cable are three individually shielded, twisted pairs of 22 AWG wires. Electrostatic noise reduction is achieved by connecting the shielding from each wire to a ground located within the SCXI 1314 terminal block. Further noise reduction was achieved by attaching a drain wire to the aluminum mount that the force sensor is attached to and grounding that wire to the SCXI 1000 chassis.

Two additional SCXI 1102 signal conditioners with attached SCXI 1303 terminal blocks are also housed in the SCXI 1000 chassis, adjacent to the SCXI 1314 terminal block. These signal conditioners are used to obtain temperature and pressure data.

Data was collected from the signal conditioners via the National Instruments PCI-6280M DAQ card which provides 18-bit resolution for analog to digital conversion. The 6280M DAQ card is housed in a Dell 4550 Dimension computer with a 2.4 GHz Pentium 4 processor and 1.5 GB of RAM. Control of the signal conditioners was achieved using virtual instrument modules, created and controlled by Labview 7.1 software. Excitation voltage, bridge completion resistance, signal filtering, and data collection parameters are easily controlled by using the software. All data is sampled at a rate of 1,000 samples per second. The 1,000 samples are then averaged to provide a single data point for one second.

Sensor Calibration and Data Reduction

In order to obtain the d_x, d_y, ξ, and ψ parameters discussed previously, the force sensor had to be calibrated. Calibration of the sensor was performed by hanging known masses from the sensor while replicating the test conditions as much as possible. This included submerging the sensor in silicone oil and applying the masses in ascending order. The sensor proportionality constant for a given axis was obtained by performing a linear regression of that axis' sensor output with respect to the applied masses when that axis was aligned with gravity. The cross

axis correction coefficient for a given axis was calculated at each mass application according to Equation 5 when the axis was aligned perpendicular to gravity. The median value of the cross axis correction coefficient was selected as the representative test value from the test sequence since the median is a better indicator of central tendency than the mean. The calculated value of the cross axis correction coefficient was generally skewed at the low end of the force range due to measurement resolution as mentioned earlier. These outlying values may distort the mean but the median remains unaffected.

To sample d_x and ψ, masses were hung from the sensor with the x-axis aligned vertically with gravity. Conversely, d_y and ξ were obtained by aligning the sensor y-axis with gravity. For a given sensor d_x and d_y were determined from the averages of d_x and d_y obtained from individual calibration tests while the values for ξ and ψ were determined from the averages of the median values of ξ and ψ obtained from individual calibration tests. After determining the d_x, d_y, ξ, and ψ parameters the relative error between the measured force and the actual force for a given axis on the sensor used to make all pin fin force measurements was never more than 2% for forces above the lowest measured pin fin drag force. This result provides the level of accuracy that can be achieved by the DSC-6 force sensor with proper calibration and when the environmental factors are properly controlled. For a detailed description of the force sensor calibration methodology see Appendix B.

Sensor Mounting Considerations

The ability to make accurate force measurements on a pin fin in a channel after successful calibration of a sensor hinged on the properties of the silicone oil and the alignment of the sensor pin fin within the channel clearance hole.

The fluid used in the pin fin clearance gap could not exhibit any elastic or shear memory properties, as this would distort the force sensor output. Dow Corning 200 silicone oil is a Newtonian fluid so in the application of a constant force on the sensor pin fin the silicone oil surrounding the pin fin in the clearance gap will provide no biased force on the pin fin. The 200 silicone oil was available in viscosities up to 100,000 cST. Since the fluid was Newtonian the oil viscosity had no effect on the force measurement, but a high viscosity oil was desirable to prevent fluid from being sheared out of the channel floor and ceiling pin fin clearance gaps. In general, 200 silicone oil with a viscosity of 100,000 cST was used in both the floor and ceiling

silicone wells. The silicone oil also acted as a thermal sink for maintaining the sensor at a constant temperature. Because the silicone oil is static, conduction was the dominant heat transfer mode. The thermal conductivity of Dow Corning 200 silicone oil was approximately 0.159 W/mK [17]. Thus, the silicone oil was more thermally conductive than air (k = 0.0263 W/mK), but less conductive than water (k = 0.613 W/mK) [18]. Additionally, Dow Corning 200 silicone oil is an exceptional electrical isolator, commonly used as a dielectric fluid in high voltage transformers. This characteristic is very important as the exposed wires of the force sensor are submerged within the silicone oil. Another favorable quality of the silicone oil, as stated by Dow Corning [17] is a relatively low surface tension of 0.0215 N/m as compared to 0.0717 N/m for water [18]. Surface tension will tend to pull the silicone fluid through the pin fin clearance gap and into the channel creating a small fillet around the top and bottom of the force sensor pin fin within the channel. The varying height of the silicone oil around the base of the pin fin can cause a resultant force on the sensor pin fin that is dependent on the oil's surface tension. With such a low surface tension however these effects are minimized with the silicone oil.

The diameter of the clearance hole for the force sensor pin fin to protrude through the floor and ceiling of the channel had to be large enough to allow free deflection of the sensor, yet small enough to prevent substantial amounts of silicone oil from flowing out of the clearance gaps. As shown in Figure 8 these criteria were satisfied for a channel floor and ceiling clearance hole diameter of 1.003 cm coupled with a force sensor pin fin diameter of 0.975 cm. This left a clearance gap size of 0.014 cm. It is important to note that the diameter of the force sensor pin fin was slightly larger than the other pins which were 0.953 cm in diameter. This difference decreases the H/D aspect ratio from 1.00 to 0.98 at the sensor pin fin. This small change was assumed to be negligible in light of the expected real world manufacturing tolerances. Ideally, the force sensor pin fin would be placed coaxially in the clearance hole and orthogonal to the flow direction.

Volume Flow Rate and Pressure Measurement Considerations

As previously discussed the volume flow rate was calculated from pressure drop measurements made across either a venturi or orifice flow meter. While the orifice meter provides a larger pressure drop for a given flow range than does the venturi, therefore requiring a

less sensitive pressure transducer, it is unable to cover a large as range of flow rates. The orifice meter, the Oripac Model 4150-P-06-2.500-150, and the venturi, Model 2300-06-3.58, were both manufactured by Lambda Square of Babylon, New York. The advertised accuracy for the venturi and orifice meters was ± 0.75% and ± 0.6% respectively [19].

Pressure differences measured across the flow meters and within the test channel were obtained using Setra Model 264 differential pressure transducers ranging in size from 0 – 0.025 kPa to 0 – 1.25 kPa, with accuracies of ± 0.4% of full scale [20]. In general the venturi meter, coupled with an appropriate sized Setra 264 pressure transducer to account for the required resolution at low flow rates, was used to measure the volumetric flow rate. For a more thorough description of each flow meter along with the accompanying physical parameters and volumetric flow rate correlations reference Brumbaugh [15].

Testing Methodologies and Data Reduction

The following sections detail the methodologies used to make pin fin force and array pressure drop measurements as well as the data reduction techniques employed for obtaining non-dimensional parameters. Additionally, the associated experimental uncertainties are presented.

Force Measurements

Special consideration had to be given to the conditioning of the sensor pin fin and the silicone oil before a force test could be conducted. Careful inspection of the sensor pin fin and the silicone oil before and after an attempted force test was required in order to ensure the validity of the measurements. The following section will discuss the key points in conducting a successful force measurement as well as the data reduction methodology used to obtain the drag lift coefficients from the raw voltage output of the sensor.

Before conducting a force test the extension piece between the test section and the flow measurement section was detached. This was done so that any excess silicone leakage from either silicone reservoir into the test channel could be wiped away before conducting a test. It was also important that there be no air bubbles within either silicone reservoir, as bubbles rising through the fluid can apply a dynamic force to the sensor pin fin. Static bubbles in contact with the sensor pin fin caused an imbalance of hydro-static pressure. The presence of both static and

dynamic bubbles was observable in the sensor output. Once the silicone oil was level in both the ceiling and floor clearance gaps and all excess silicone had been removed from the test channel the extension piece was reattached. Next, the test section was covered with several dark cloths in order to provide additional shielding for the sensor from the ambient lighting. Once an acceptable drift rate was realized by the sensor output, the blower, which was set to a desired rotational speed, was turned on and the sensor output was recorded. Data was recorded for 15 minutes at the end of which the blower was turned off. After the test, the extension piece and the cloths covering the test section were removed and the condition of the sensor pin fin and the silicone oil were inspected. Specifically, the channel was examined for excess silicone oil leakage from either reservoir or any air bubbles which may have formed in either reservoir. If enough silicone oil was sheared from the reservoirs during a flow test it would form a small bulb shaped fillet behind the sensor pin fin. This fillet could act to reduce drag, biasing the sensor output by changing the trailing edge shape of the pin fin. Although the occurrence of either of these phenomena was usually apparent in the sensor output, a visual check was warranted. Force tests that showed excessive silicone oil in the test channel, or a bubble in either reservoir, were discarded. If all the prior conditions were satisfactory and the sensor output reached a steady value then the data was reduced to provide a drag and lift coefficient.

The drag and lift force were calculated according to Equation 3 after applying the cross axis corrections defined by Equation 4. In order to obtain the drag and lift coefficients the forces were normalized by the product of the dynamic pressure head, based on the velocity through the open flow area, and the projected frontal area of the sensor pin fin as shown in Equation 6. The volume flow rate was calculated from the pressure drop measurements made across the flow measurement device during testing and along with the average temperature of the channel flow, the Reynolds number was calculated.

$$C_D = \frac{F_D}{\frac{1}{2}\rho U^2 H d}$$
$$C_L = \frac{F_L}{\frac{1}{2}\rho U^2 H d} \qquad (6)$$

It is important to note that the data analysis was not conducted using the entire 15 minutes of data recorded during the force measurement test. Instead, a 60 second analysis window was chosen, and the data within that window was analyzed. The 60 second analysis window was chosen to begin as soon as the sensor output reached a steady state value after the initial transient. In general the data analysis window was chosen from 360 to 420 seconds after the start of the blower, as this was the time that most successful tests had reached a steady value. Figure 9 illustrates the shape of a typical output curve by plotting the cross-axis corrected voltages from the DSC-6 sensor output, specifically a Re = 24,000 flow for a single row of pin fins with an S1/d = 2. Note that the output voltage corresponding to the lift in Figure 9 is essentially zero as was the case for all force tests when the array was symmetric across the width of the test channel. The time required for the force sensor output to reach a steady value was not consistent, and appeared to be dependent upon the flow rate, spacing and, in the case of multiple row arrays, the row position of the sensor pin fin.

For a single row of pin fins above an S1/d = 2 at flows greater than Re = 18,000, it was often necessary to analyze the data taken from 90 to 150 seconds after the start of the blower as eventually excess silicone oil being sheared from the clearance gaps became significant enough to cause the sensor output to decay. Conversely, the data analysis window for measurements made in the inner rows of a multiple row array often had to be chosen much later than 360 seconds after the start of the blower as the sensor output exhibited a much slower rise to a steady value than those outputs from the first row. The 60 second data analysis window in these cases ranged any where between 560 to 860 seconds after the start of the blower. For a more detailed description of the force testing and data reduction methodology as well as an at length discussion on the effects of air bubbles and silicone oil leakage on the sensor output see Appendix C.

Pressure Drop Measurements

Compared to the force measurements, tests conducted to obtain the pressure drop across a particular pin fin array were relatively simple. Static pressure taps spanning the width of the test channel located both upstream and downstream of the array being tested were used to obtain an average upstream and downstream pressure relative to the array. The difference in these average pressures yielded the pressure drop between the measurement points.

Individual pressure measurements were made by using the first pressure tap at the entrance to the test channel as the reference high pressure and switching the corresponding low pressure reference using a dial operated switch valve. In all cases the upstream and downstream static pressure taps used for making pressure measurements were located at least three hydraulic diameters from the entrance and exit of the array. These locations were chosen to eliminate any entrance or exit effects propagating from the location of the array. Consequently, this method of measurement required the subtraction of the pressure drop due to the empty test channel between the measurement locations. The empty channel pressure losses were estimated using the correlations in Equations 1 and 2. Similar to other researchers, the measured pressures were only extrapolated to a distance S2/2 both upstream and downstream of the array so that those pressure drops inherent to the entrance and exit effects of the array were still considered. For single row arrays, which had no streamwise spacing, the entire distance between pressure measurement points was used to subtract off the pressure due to the empty test channel since entrance and exit effects were assumed negligible.

Once the pressure drop due to the array was found it was reduced to a non-dimensional array friction factor. This was done by normalizing the array pressure drop by four times the product of the dynamic pressure head, based on the maximum velocity through the minimum flow area between pin fins, and the number of pin fin rows in the streamwise direction as shown in Equation 7.

$$f_{array} = \frac{\Delta P_{array}}{2\rho U_{max}^2 N} \tag{7}$$

This particular definition of array friction factor was one commonly used by other researchers so for the sake of comparison it was also employed for the current results. Again the volume flow rate was calculated from the pressure drop measurements made across the flow measurement device during testing and along with the average temperature of the channel flow, the Reynolds number was calculated.

Experimental Uncertainty

Uncertainty analyses were conducted on the drag coefficient (C_D), lift coefficient (C_L), array friction factor (f_{array}), channel Reynolds number (Re), and pin Reynolds number (Re_d) according to the methodology of Moffat [21]. This technique includes reducing the desired calculation down to a function of only the directly measurable quantities. The partial derivative of the reduced equation is then calculated with respect to each measurable quantity and then multiplied by the uncertainty in that single variable. A measurable quantity could contain uncertainty due to both a bias error, which is based on the accuracy of the measuring device, and precision error, which is based on a statistical analysis from several measurements of the same quantity. The root sum square of all these terms is the overall uncertainty of the calculated result.

The uncertainty analysis was conducted on representative tests at the lowest (Re < 10,000) and highest flow rates (Re > 30,000) for several different geometries, providing bounding uncertainty estimates. Table 1 summarizes the results of the uncertainty analyses at a 95% confidence level. Details regarding the uncertainty estimates are provided in Appendix D.

Studying Table 1, one immediately notices that the uncertainty values pertaining to the low flow rate measurements are significantly higher than those measured at the high flow rates. As mentioned previously most of the volume flow rate measurements were made with the venturi meter. At low flow rates the pressure drop across the venturi could be as low as 0.02 kPa. The pressure drop was measured using an appropriate sized pressure transducer so the high uncertainty must be taken in context with the small magnitude of the pressure drop. In comparison, the uncertainty in the drag coefficient at the low flow rate for the single row array with S1/d = 2 is much smaller since the orifice meter, which provided a larger pressure drop, was used for measuring the volume flow rate. Reference to Appendix D shows that the majority of the uncertainty values presented in Table 1 are due to the uncertainty within the volume flow rate and the channel height.

Pin Fin Force Measurements

The following three sections detail the current experimental force trends observed on single row and staggered multiple row arrays for a variety of effects. The effects of row number and Reynolds number are first discussed, with a comparison to detailed row-by-row pressure

drag measurements obtained from the literature [13]. Next, the effects of spanwise pin spacing on single row array drag results are considered. Finally, the dependence of pin fin force on flow incidence angle in a multiple row array, specifically the special case of an inline incidence angle, is presented.

Reynolds Number Effects on Single and Multiple Row Pin Fin Arrays

The drag on a pin fin showed two different trends with Reynolds number between a single and a staggered, multiple row array. Figure 10 compares drag coefficients from a single row array with a S1/d = 4 to measurements made in several rows of a multiple row array with a similar spanwise pin spacing and a streamwise pin spacing of S2/d = 3.46. It is important to note that this particular streamwise pin spacing corresponds to an equilaterally triangular spaced array for a S1/d = 4, where the straight line distance between pin centers is uniform. Both arrays have a H/d = 1.

The results from Figure 10 indicate that the drag coefficient for a single row increases up to a pin Reynolds number of approximately Re_d = 10,000, at which point the drag coefficient becomes essentially constant. The initial increase in drag can be related to the flow separation occurring on the pin fin. As the Reynolds number is increased the momentum effects begin to dominate and the flow is unable to follow the curvature of the pin fin. The drag force increases proportionately more than the square of the velocity due to the separation point moving toward the stagnation side of the pin fin. As the separation location moves forward, the pressure drag increases. Once the separation point has reached a stable position, the drag becomes well scaled by the square of the velocity, remaining essentially constant as compared to the initial increase with Reynolds number.

Contrary to the single row results, the multiple row drag coefficient from each row tested decreases with Reynolds number as shown in Figure 10. The pin Reynolds number dependence ranges from -0.16 to -0.07 based on fitted power curves, with the dependence being highest for the first row of pin fins and lowest for the sixth row. The first row of pin fins is the only row not subject to an upstream wake, so it is expected that these results show a greater dependence on Reynolds number. The Reynolds dependency can be attributed to the wake interactions among the converging and diverging streamlines that the flow follows through the staggered rows. To

the contrary, the wakes from the single row of pin fins are unforced and are allowed to simply diffuse out while proceeding downstream.

The results in Figure 10 also indicate that the single row drag is larger than the multiple row drag. Again, this effect is most likely attributed to the row-by-row wake interactions in the staggered, multiple row array. The first row wakes are forced to converge between pins in the subsequent row with the net result being a decrease in the drag compared to the single row case. In addition to the converging wakes, the inner rows of the array are subject to incoming diverging wakes which serve to relieve those rows of the stronger Reynolds number dependence seen in the first row.

Figure 10 suggest that at this particular pin spacing the differences in drag among the rows of a multiple row array are small. Additionally, the row-by-row drag exhibits similar trends with Reynolds number. This is in contrast to the pressure drag coefficients shown in Figure 11. Figure 11 compares the same multiple row array drag results from Figure 10 with pressure drag coefficients obtained from the integration of static pressure distributions around the midline of a pin fin. The drag coefficients in Figure 11 are normalized with the velocity through the minimum flow, corresponding to the maximum velocity, as this was the reduction technique employed by Ames et al. [13]. Ames et al. [13] measured midline static pressure distributions around pin fins in the first five rows of an eight row staggered array. The array spacing used by Ames et al. [13] was tighter than those in comparison with an equal S1/d and S2/d of 2.5. Additionally, Ames et al. [13] used a large pin aspect ratio of H/d = 2.

The results of Ames et al. [13] show differences in Reynolds number dependency within the first few rows as compared to the subsequent inner rows. The pressure drag in the first and second rows scale well with the square of the velocity as the pressure drag coefficients remain essentially unchanged with Reynolds number. The third row results indicate a slope change while the pressure drag coefficients in the subsequent rows decrease with Reynolds number, similar to that seen in the current experimental results. There is, however a greater Reynolds number dependency for the inner row results of Ames et al. [13] than for the current experimental results. As a whole, the pressure drag results are less than the total drag comparison since the total drag includes the contributions from the viscous drag. Differences between the data in Figure 11 may indicate why the directly measured drag results do not show a dramatic

difference in Reynolds number dependency. Additionally, the effects of a tighter spaced array as well as the increased pin aspect ratio may be contributing to the severity of the development.

Pin Spacing Effects on a Single Row Pin Fin Array

Although the same trend with Reynolds number was observed in all the single row arrays, there were significant differences in the magnitude of the drag coefficient among different spanwise pin spacings. Figure 12 plots the drag coefficient versus pin Reynolds number for three different spanwise pin spacings, S1/d = 12, 4, and 2 with H/d = 1. The key feature concerning Figure 12 is that the drag increases with decreasing spanwise pin spacing. This effect is attributed to the increased pressure drag resulting from the increase in blockage area associated with the tighter spaced rows.

While the transition from S1/d = 12 to S1/d = 4 is indicative of an increased blockage area effect, the shift from S1/d = 4 to S1/d = 2 is much larger and suggests an additional augmentation of the flow field around the pin fins. This phenomenon is likely related to the influence of spanwise pin spacing on the flow separation point. At the tightest spanwise spacing, the velocity between pins is much higher than in the other two cases. The higher velocity is accompanied with a lower pressure, causing the flow to detach at an earlier location on the pin fin and substantially increasing the drag.

It is important to point out that the drag coefficient from the S1/d = 12 array reaches a constant value at approximately the same pin Reynolds number as the S1/d = 4 array of Re_d = 10,000. This is in contrast to the S1/d = 2 array where, over the Reynolds number range tested, the drag coefficient remains essentially constant. This again can be attributed to the effect of the tighter spanwise pin spacing. It is likely, however, that drag coefficients at pin Reynolds numbers less than Re_d = 7,500 would decrease in a similar fashion to those wider spaced arrays.

Flow Incidence Angle Effects on Multiple Row Pin Fin Arrays

For the staggered, equilaterally triangular spaced array, a critical angle is reached when the flow approaches the array at 30° to the channel cross section normal. At this angle the array appears inline to the incident flow. Instead of following converging and diverging streamlines the majority of the flow is able to pass, unobstructed, between rows oriented in the streamwise direction. Figure 13 compares the multiple row drag coefficient results from Figure 10 with the fifth row results from an identical array angled at 30° to the incoming flow. Note the array is

angled with respect to the flow in order to simulate an inline flow incidence angle. Also shown in Figure 13 are the associated components of the first row non-angled results obtained from the decomposition of the force vector if the array were turned by 30°.

As might be expected the drag on the pin fin within the inline array is considerably smaller than the drag from the staggered array. Additionally, due to the non-symmetric angled array, there is a significant lift force present. In the case of the non-angled staggered arrays the lift coefficients were in general less than 5% of the drag coefficient, indicating that the lift was essentially zero. Another observation from Figure 13 is that the lift and drag coefficients from the angled array appear to be independent of Reynolds number. Unlike the non-angled array the pin fin wakes are not forced to interact in the spanwise direction and instead interaction is confined mainly to the streamwise direction. This is analogous to the single row wake interactions thus the dependence on Reynolds is similar. Final inspection of Figure 13 shows that the non-angled drag results can not simply be decomposed into there respective orthogonal components in order to predict the drag and lift on an angled array. The decomposed results fall above the results for an inline array and continue to exhibit a dependency on Reynolds number. The fact that the decomposed results are disconnected suggests that the flow fields between staggered and inline arrays are fundamentally different.

Array Pressure Drop Measurements

The following four sections detail the pressure drop trends observed on single and staggered multiple row arrays. Reynolds number dependency and the effect of single versus multiple staggered rows are first discussed, with a comparison to correlations provided by Metzger et al. [5]. Next, the effects of spanwise and streamwise pin spacing on single and multiple row arrays are considered. Again the effects of flow incidence angle are investigated in a multiple row array, for an inline incidence angle and an intermediate angle as well. Finally, the influence on pressure drop with a reduction in the pin aspect ratio for multiple row arrays is presented.

Reynolds Number Effects on Single and Multiple Row Pin Fin Arrays

Like the pin fin drag results, array pressure drop showed two separate trends with Reynolds number between a single and staggered, multiple row array. Figure 14 compares the

array friction factor results between a single and multiple row array with similar spanwise pin spacings, S1/d = 4, and a streamwise pin spacing of S2/d = 3.46. Again it is important to note that this particular streamwise pin spacing corresponds to an equilaterally, triangular spaced array. Both arrays have a H/d = 1.

On first inspection of Figure 14, it is evident that the pressure drop trends between a single and staggered, multiple row array are very similar to the single and multiple row array trends for drag coefficient shown in Figure 10. Friction factor for arrays, are a measure of non-dimensional pressure drop across the array which is directly related to the drag experienced by the array. It comes to reason that the friction factor trends are predictive of the drag coefficient trends. Additionally, the causes for these trends are similar to those discussed for the drag forces.

Comparing the single row results in Figures 10 and 14 shows that both trends reach a constant value at approximately Re_d = 10,000. However, unlike the drag results in Figure 10 where the single row results are larger than the multiple row results, the single versus multiple row results in Figure 14 converge at approximately Re_d = 22,000.

Array friction factor results for a staggered, multiple row array show an increase in the pin Reynolds number dependency at approximately Re_d = 17,500. Figure 15 compares the results of several array friction factor measurements for a S1/d = 4, S2/d = 3.46 multiple row array with those correlations provided by Metzger et al. [5] for a multiple row array with S1/d = 2.5. The results of Metzger et al. [5] show an increase in Reynolds number dependence from -0.132 to -0.318 at a pin Reynolds number of Re_d = 10,000. The current experimental results also show a similar increase in Reynolds number dependency from -0.071 to -0.287, but the change occurs at a higher pin Reynolds number of approximately Re_d = 17,500. The differences may lie in the fact that Metzger et al. [5] correlations were fitted to within ± 15% for a range of streamwise pin spacings, S2/d = 1.05 to 5.0. In contrast, those correlations presented for the current results were fitted to within ± 3% for a single array geometry. Additionally, the correlations of Metzger et al. [5] predict a higher pressure drop than those correlations in comparison. This is an effect of spanwise pin spacing and is discussed in further detail in the following section.

Pin Spacing Effects on Single and Multiple Row Pin Fin Arrays

Figure 16 shows the array friction factor results for several different spanwise and streamwise pin spacings for both single and staggered, multiple row arrays with an H/d = 1. Similar to the drag results in Figure 12, the array friction factors also increase with a decrease in spanwise pin spacing. Again, this effect is related to the increased blockage area inherent to a tighter spaced array. The current experimental results for a multiple row array with S1/d = 2 and S2/d = 1.73, which is the streamwise pin spacing corresponding to an equilaterally triangular spaced array, show good agreement with the correlated results of Metzger et al. [5]. Metzger et al. [5], who studied a multiple row array with a S1/d = S2/d = 2.5, have results that fall just below the S1/d = 2 results as would be expected for a slightly wider spaced array. However, as discussed in the previous section, the Reynolds number dependency transition occurs around Re_d = 17,500 instead of Re_d = 10,000.

Additionally, Figure 16 illustrates the effects of streamwise pin spacing for two different spanwise spaced arrays, S1/d = 2 and 4. Note that the streamwise pin spacings used, S2/d = 1.73 and 3.46 are not random values. Instead, they correspond to the associated equilateral triangle streamwise pin spacing for both spanwise pin spacings. At the tighter spanwise pin spacing, an increase in the streamwise pin spacing corresponds to a slight increase in the pressure drop. At the wider spanwise pin spacing this effect appears to be present but the increase is marginal. This phenomenon can be explained by the fact that the wakes are allowed to mix for a longer distance in the streamwise direction before encountering the next row of pins. Consequently, the pressure drop is higher through the array with a larger streamwise pin spacing. As discussed previously, the S1/d = 2 array presents an interesting case where the interaction among pin wakes is stronger due to the relatively high velocities between pin fins; therefore, a change in the streamwise pin spacing has a greater influence on the associated pressure drop than for the wider spanwise pin spacing of S1/d = 4. In either case, the effect of changing streamwise pin spacing is less influential on the pressure drop than a change in the spanwise pin spacing.

These trends are similar to those seen in a numerical study by Hamilton et al. [2], who also showed an increase in the pressure drop with both a decrease in the spanwise pin spacing and an increase in the streamwise pin spacing. Again with the effects of the streamwise pin spacing being less influential than that of the spanwise pin spacing. Additionally, Hamilton et al.

[2] showed that the effect of increasing streamwise pin spacings below three is essentially negligible on pressure drop for a S1/d > 2.

Flow Incidence Angle Effects on Multiple Row Pin Fin Arrays

Figure 17 compares the changes in array friction factor with flow incidence angle for two equilaterally, triangularly spaced arrays, specifically, S1/d = 2 and 4 with H/d = 1. Similar to the pin fin drag results in Figure 13, a large drop in pressure loss is observed for the flow incidence angle, $\alpha = 30°$, compared to non-angled arrays because the flow geometry lends itself to a more inline array. Here again the relative reduction in pressure drop achieved with the inline flow incidence angle is larger for the tighter spaced array for those reason discussed previously.

Another interesting feature in Figure 17 is that at an intermediate angle of 15°, there is essential no change in the pressure drop for the wider spaced array. For the tighter spaced array, from what has been observed from other effects related to geometry changes, it is likely that there would be some noticeable reduction in pressure drop at an intermediate angle.

Pin Aspect Ratio Effects on Multiple Row Pin Fin Arrays

The available literature suggests that an increase in pin aspect ratio as little effect on array pressure drop. The same appears to be true with the data presented in Figure 18. Figure 18 shows the results for an equilaterally, triangular spaced, multiple row array with S1/d = 2 for H/d = 0.5 and 1. Additionally, Figure 18 shows the results from each pin aspect ratio case for an inline flow incidence angle. It is important to note that the pin aspect ratio was decreased by increasing the diameter of the pin fins by a factor of two while keeping the test channel height the same.

Inspection of Figure 18 shows that there is no change in the array friction factor between the H/d = 0.5 and 1 cases. There is, however, a difference associated with the pin aspect ratio when the effects of an inline flow incidence angle are considered. Figure 18 shows a relative reduction in pressure loss associated with an inline flow incidence angle that is larger in the H/d = 1 case than in the H/d = 0.5 case. This difference may be explained by the fact that the flow resembles that between parallel plates moreso in the H/d = 0.5 case since, relative to the pin diameters, the channel height is smaller.

Flow Visualization Methodology and Results

The following sections discuss the technique employed for performing and recording flow visualization. The results of the flow visualization experiment consist of selected still images as well as an estimated calculation of the Strouhal number. Flow visualization was performed on the third, fourth, and fifth row of a staggered, eight row array. Specifically an array with a spanwise pin spacing of S1/d = 4 and a streamwise pin spacing of S2/d = 3.46. Unfortunately, the channel Reynolds numbers at which successful flow visualizations were able to be performed are well below those in which the other experimental results were obtained and for that matter below flows associated with gas turbine internal cooling. Nevertheless, there is some merit in the investigation of flow fields at these Reynolds numbers as it gives insight into the how the flow develops.

Flow Visualization Methodology

Flow visualization was performed using an X-Stream VISION, model 3 (XS-3), high speed motion camera, manufactured by Integrated Design Tools (IDT). As shown in Figure 19 the camera was attached to a tripod and set up directly over the viewing area. The viewing area was illuminated from several sides using fluorescent lighting. Figure 20 shows a schematic of the viewing area, which consisted partly of the third, fourth, and fifth pin rows of a staggered, eight row array. The pin fins were set on top of black carpet tape. The dark back drop was used to highlight the contrasting white fog, which was introduced on the upstream side of the plenum as shown in Figure 21 using a simple water-based fog machine. As shown in Figure 22, in order to keep from densely polluting all the air flow with fog, the test rig was ran open loop by disconnecting the recirculation pipe from the downstream side of the blower. In this way the fog was allowed to escape into the room.

Flow visualization was performed by first turning the blower on. Once the blower completed its initial start up and the flow was steady the fog machine was turned on and the fog was allowed to fill the plenum. The fog would then quickly begin to enter the test channel at which point the camera was turned on and the flow visualization was recorded.
While several flow visualization images were recorded only a few were selected based on there resolution and quality.

Flow Visualization Results

The first flow visualization image presented corresponds to a channel Reynolds number of approximately Re = 1,000. Figure 23 presents a single still image of the flow visualization pattern captured at this Reynolds number. Kakac et al. [12] state that channel flow trips to turbulent at a channel Reynolds number of approximately Re = 5,000. Although the pin fins are active in causing this transition at a lower Reynolds number, it appears as if the flow is still laminar. The convergence and divergence of the streamlines are also evident as the fog travels downstream. Additionally, there doesn't appear to be any discrete vortices breaking away from the pin fins. Instead there are two standing eddies on the downstream side of the pin fins as evident by the dark bands, indicating an absence of fog, on the backside of the pin fins. This is similar to that observed behind an infinite cylinder in external crossflow for Re < 40 [22].

The second set of flow visualization images corresponds to a channel Reynolds number of approximately Re = 2,000. Figure 24 presents several annotated images showing a distinctly different flow pattern than the one shown in Figure 23. The flow appears to be transitioning to turbulence if it is not turbulent already. Even though the flat duct correlations of Kakac et al. [12] predict turbulence occurring at Re = 5,000 for an empty channel, the pin fin array is influential in causing the early transition. Additionally, the attached eddies of Figure 23 have given way to vortices that alternatively form and then shed from the back of the pin fins. Specifically, Figure 24 shows a series of images that depict the formation and separation of a single vortex from the left side of a single pin fin in the fourth row. The images were recorded at 610 frames per second so the six images shown cover approximately 0.01 seconds. The frequency of this vortex shedding oscillation, f, when non-dimensionalized by the pin fin diameter and the free-stream velocity is called the Strouhal number as defined in Equation 8.

$$St = \frac{fd}{U} \tag{8}$$

For a single infinitely long cylinder in external cross flow the Strouhal number varies slightly with Reynolds number but is roughly equal to 0.2 over a wide range of Reynolds number [22]. Calculations of the Strouhal number from the flow visualizations recorded predict a Strouhal number in the range of approximately 0.22 to 0.27. The similarities between these

Strouhal numbers and that for an infinitely long cylinder indicate that the effects driving the formation and shedding of vortices in internal flow are similar to those for external flow.

Conclusions

This paper summarizes the experimental pin fin force and array pressure drop results as they are related to changes in Reynolds number, spanwise pin spacing, streamwise pin spacing, flow incidence angle, and pin aspect ratio for both single and multiple row arrays. This final chapter comments on the viability of the testing methods, presents an overview of the observed trends obtained from the experimental results, compares trends between pressure drop and heat transfer augmentation, and provides recommendations for future testing.

Viability of Test Facility and Experimental Methodology

The test facility was benchmarked with static pressure taps to demonstrate flow uniformity across the width of the test channel and full hydrodynamic development along the length of the test channel. Flow uniformity was shown to be achieved to within 2.5% across the width of the channel while the channel friction factor was shown to match published correlations to within 2.5%. Additionally, it was shown that the flow reaches the fully developed state approximately 26 hydraulic diameters into the test channel. This distance was well before the presence of any of the pin fin arrays tested. These benchmarking experiments indicate that the velocity profile within the channel reached full hydrodynamic development as well as spanwise uniformity before impingement on the pin fin array.

While pressure loss measurements made using static pressure taps is a well understood technique, the methodology used for making pin fin force measurements is not. The force measurement methodology hinged on the use of a force sensor, the DSC-6, which was shown to be able to measure forces as low as 3.4×10^{-2} N to within 2%. Additionally, the pin fin force results are an accumulation of several repeated measurements of which the average result was presented. In almost all cases the scatter of the data was within ± 5% of the average. Given the successful calibration of the force sensor and the repeatability of the measurements, it is reasonable to assume that this methodology is fully capable of resolving two-axis forces on an individual pin fin in channel flow.

Overview of Results

Pin fin force and array pressure drop were found to have substantially different trends with Reynolds number between a single and multiple row array. For a single row the results showed an initial increase in both the pin fin drag and array pressure drop to a constant value at approximately Re_d = 10,000. In contrast, multiple row array results showed a reduction with increasing Reynolds number over the entire flow range tested. Additionally, a similarity in trends between array pressure drop and pin fin drag was found to be present.

Both single row pin fin drag and array pressure drop were found to increase with a decrease in the spanwise pin spacing. For multiple row arrays an increase in the streamwise spacing was found to increase the array pressure drop but less so than for a decrease in the spanwise pin spacing. In fact, the effects of streamwise pin spacing were found to be mostly confined to the spanwise pin spacing of S1/d = 2.

In examining the effect of inline flow incidence angle it was found that both pin fin drag and the array pressure drop substantially decrease with an inline flow incidence angle. Here again this reduction effect was larger in the case of the tightest spanwise pin spacing of S1/d = 2. In fact, all the experimental results suggest that spanwise pin spacings of $S1/d \leq 2$ represent a critical range where the effects of array geometry changes are amplified.

While a reduction in pin aspect ratio showed no influence on the array pressure drop it did effect the reduction in array pressure drop that was observed with an inline flow incidence angle. At a pin aspect ratio of H/d = 0.5 the reduction in array pressure drop was smaller for an inline flow incidence angle than for an array with a pin aspect ratio of H/d = 1 for a spanwise pin spacing of S1/d = 2.

Comparison of Heat Transfer and Pressure Drop Augmentation

The purpose of a pin fin array is to enhance the heat transfer by providing both turbulence augmentation and increased surface area. Consequently, the features of a pin fin array that benefit heat transfer are often the same ones that adversely affect the pressure drop. However, by comparing results between heat transfer and pressure drop trends as they are related to changes in array geometry, an optimal pin fin array can be designed that takes advantage of the beneficial augmentations. All heat transfer results presented were obtained from a parallel experimental project performed and documented by Lawson [23].

Figure 25 plots the heat transfer and pressure drop augmentation versus channel Reynolds number for four staggered, seven row arrays with pin aspect ratio's of H/d = 1. Note that arrays with spanwise pin spacings of S1/d = 2 and 4 have equilaterally triangular spacing for streamwise pin spacings of S2/d = 1.73 and 3.46 respectively. Heat transfer augmentation is represented as the ratio of the area averaged Nusselt number, averaged over the endwall area of the entire array, to the Nusselt number for fully developed channel flow. Pressure drop augmentation is represented as the ratio of the array friction factor to the fully developed channel friction factor. In both augmentation ratios the normalizing channel term is evaluated at the same Reynolds number as the corresponding experimental result.

The augmentation results in Figure 25 show that both heat transfer and pressure drop augmentation increase with a decrease in spanwise pin spacing from S1/d = 4 to 2. For heat transfer a reduction in the streamwise pin spacing corresponds to an increase in the heat transfer augmentation, with the effects being greater at the larger spanwise pin spacing of S1/d = 4. This is in contrast to the pressure drop results, where a reduction in the streamwise pin spacing corresponds to a decrease in the pressure drop augmentation, although less substantial than the increase seen in heat transfer augmentation. Additionally, unlike the heat transfer augmentation trends, the effects of streamwise pin spacing on pressure drop augmentation are essentially confined to the tighter spanwise pin spacing of S1/d = 2.

Figure 26 plots the heat transfer and pressure drop augmentation versus channel Reynolds number for a staggered, seven row array with S1/d = 2 and S2/d = 4. Specifically, Figure 26 illustrates the effects of inline flow incidence angle and pin aspect ratio. Both heat transfer and pressure drop augmentation decrease with a reduction in the pin aspect ratio from H/d = 1 to 0.5. Additionally, pressure drop augmentation is reduced for an inline flow incidence angle, with the effects being greater for the larger pin aspect ratio of H/d = 1. This is in contrast to the heat transfer augmentation results, which show little change with flow incidence angle for both pin aspect ratios.

The best pin fin array design is one that will maximize heat transfer augmentation while minimizing pressure losses. Due to this opposing relationship between heat transfer and pressure drop it is evident that the most can be gained from considering those trends which are also opposite in nature. From the above discussion it was shown that a reduction in streamwise pin spacing corresponds to an increase in heat transfer augmentation but a decrease in pressure drop

augmentation. Additionally, while an inline flow incidence angle corresponds to a substantial reduction in pressure drop, heat transfer augmentation remains essentially unaffected. These two observations are paramount in the design process of a pin fin array as the correct balance of these effects will yield the optimal pin fin array geometry.

Recommendations for Future Testing

Several interesting features of this project remain to be explored. First is a benchmarking test on an individual pin fin. The array pressure drop trends are quite similar to the pin fin drag trends since a majority of the total drag is pressure drag. However, the actually contributions to the total drag from the pressure and viscous drag are unknown. Therefore it may be of interest to independently quantify the pressure drag and viscous drag on the pin fin. The pressure drag could be obtained by measuring the static pressure distribution over the entire pin fin surface as done by Ames et al. [13]. Quantification of the viscous drag is however more difficult, but may be possible via an oil interferometry method. Consequently, the small size of the pin fin makes spatial resolution a problem with oil interferometry. Another approach may be the use of particle image velocimetry (PIV) to examine the wake behind the pin fin and the boundary layer on the pin fin surface. In doing so, one could respectively calculate the pressure and viscous drag on the cylinder. Regardless, an innovative benchmarking technique is needed to truly validate the results of this experiment and resolve the discrepancies with the integrated pressure drag coefficients calculated from the data of Ames et al. [13].

Second is the investigation of sources of possible force measurement biasing. Using a similar experimental methodology, DeTurris et al. [24] used the DSC-6 force sensor to measure two-component skin friction forces in a supersonic combustion flow. Unlike with this project the flat element attached to the force sensor and in contact with the supersonic flow only had to be decoupled from one wall, the channel floor. DeTurris et al. [25] mentioned the presence of a lip force that is generated by a pressure gradient in the gap between the force sensor element and the channel wall. In order to minimize this force DeTurris et al. [25] used a taper on the force sensing element just below the test channel surface. Additionally, Schetz [26], who also made skin friction measurements using a similar technique, stated that the pressure gradient can be decreased in severity, thus minimizing the lip force, by filling the gap with a viscous fluid. While an extremely viscous silicone oil, 100,000 cST, was used as the filler fluid in this project there

still could be pressure gradients present that are large enough to effect the measurements. In order to further investigate this phenomenon a taper could be machined into the top and bottom of the sensor pin fin just above and below the walls of the test channel. If measurements remain unchanged it is likely that the viscous silicone oil is effective in reducing the lip force so that it is insignificant compared to the pin fin forces being measured.

Finally, in order to decrease the time required for obtaining viable pin fin force results, a new installation technique could be designed that automatically centers the sensor pin fin in the channel floor and ceiling holes. The difficulty in manually performing this task is the main reason why the pin fin force results were not in a great of multitude as the array pressure drop results. Additionally, if force results are needed on a pin fin geometry that is not cylindrical, a new testing methodology may be required since the gap around the sensor element will be more complex. Future investigators would be well served to consider a small detachable section that contains the force sensor and the corresponding channel ceiling and floor pieces so that installation and assembly time is reduced.

References

[1] Lau, S. C., Kim, Y. S., and Han, J. C., 1985, "Effects of Fin Configuration and Entrance Length on Local Endwall Heat/Mass Transfer in a Pin Fin Channel," ASME Paper No. 85-WA/HT-62.

[2] Hamilton, L. J., Adametz, D. S., Lind, E. K., and Gopinath, A., 2002, "Numerical Analysis of the Performance of a Staggered Cross-Pin Array Heat Exchanger," AIAA Paper 2002-3008

[3] Zukauskas, A. A., 1972, "Heat Transfer from Tubes in Cross Flow," *Advances in Heat Transfer*, Vol. 8, pp. 116-133.

[4] Jacob, M., 1938, "Heat Transfer and Flow Resistance in Cross Flow of Gases Over Tube Banks," *ASME Transactions*, Vol. 60, pp. 384-386.

[5] Metzger, D. E., Fan, Z. X., and Shepard, W. B., 1982, "Pressure Loss and Heat Transfer through Multiple Rows of Short Pin Fins," *Heat Transfer* 1982, Vol. 3, U. Grigull et al., eds., Hemisphere, Washington, pp. 137-142 .

[6] Peng, Y., 1984, "Heat Transfer and Friction Loss Characteristics of Pin Fin Cooling Configurations," ASME *Journal of Engineering for Gas Turbines and Power*, Vol. 106, pp. 246-251.

[7] Damerow, W. P., Murtaugh, J. C., and Burgraf, F., 1972, "Experimental and Analytical Investigation of the Coolant Flow Characteristics in Cooled Turbine Airfoils," NASA CR-120883.

[8] Chyu, M. K., 1990, "Heat Transfer and Pressure Drop for Short Pin-Fin Arrays with Pin-Endwall Fillet," ASME *Journal of Heat Transfer*, Vol. 112, pp. 926-932.

[9] Metzger, D. E., Fan, C. S., and Haley, S. W., 1984, "Effects of Pin Shape and Array Orientation on Heat Transfer an Pressure Loss in Pin Fin Arrays," ASME *Journal of Engineering for Gas Turbines and Power*, Vol. 106, pp. 252-257.

[10] Evenko, V. I. and Anisin, A. K., 1976, "Increasing Efficiency of Heat Transfer by Bundles of Tubes in Transverse Flow," *Teploenergetika*, Vol. 23, pp. 21-24.

[11] Armstong, J. and Winstanley, D., 1988, "A Review of Staggered Array Pin Fin Heat Transfer for Turbine Cooling Applications," ASME *Journal of Turbomachinery*, Vol. 110, pp. 94-103.

[12] Kakac, S., Shah, R. K., and Aung, W., 1987, *Handbook of Single Phase Convective Heat Transfer*, New York, NY: Wiley.

[13] Ames, F. E., Dvorak, L. A., and Morrow, M. J., 2005, "Turbulent Augmentation of Internal Convection over Pins in Staggered Pin Fin Arrays," ASME *Journal of Turbomachinery*, Vol. 127, pp. 183-190

[14] Ames, F. E. and Dvorak, L. A., 2006, "The Influence of Reynolds Number and Row Position on Surface Pressure Distributions in Staggered Pin Fin Arrays," ASME Turbo Expo 2006: Power for Land, Sea and Air, Barcelona, Spain, GT2006-90170.

[15] Brumbaugh, S. J., 2006, "Development of a Methodology to Measure Aerodynamic Forces on Pin Fins in Channel Flow," Master's Thesis, Department of Mechanical Engineering, Virginia Polytechnic Institute and State University.

[16] Kistler Morse, 1998, "Displacement Sensor (DS-6) Inspection and Operation Instructions," brochure (Bothell, WA: Kistler Morse, August 1998).

[17] Dow Corning Corporation, 2000, "Product Information: 200 Fluid 10,000 cs, 12,500 cs, 30,000 cs," brochure (Dow Corning Corporation, October 9, 2000).

[18] Incropera, F. P. and DeWitt, D. P., 1996, *Fundamentals of Heat and Mass Transfer*, 4th ed. (New York, NY: John Wiley & Sons, 1996).

[19] Lambda Square Inc./LSI, 1996, "Installation Instructions for the Oripac (Model 4150-P, 4150, Model 5200)," brochure (Babylon, NY: Lambda Square Inc./LSI, February 3, 1996).

[20] Setra Systems Inc, 2001, "Model 264 Very Low Differential Pressure Transducer," brochure (Boxborough, MA: Setra Systems Inc., April 19, 2001).

[21] Moffat, R. J., 1988, "Describing the Uncertainties in Experimental Results," *Experimental Thermal and Fluid Science*, Vol 1, no. 1, January 1988, pp. 3-17.

[22] Panton, R. L., 2005, *Incompressible Flow*, 3rd ed. (Hoboken, NJ: John Wiley & Sons, 2005)

[23] Lawson, S. A., 2007, "Heat Transfer from Multiple Row Arrays of Low Aspect Ratio Pin Fins," Master's Thesis, Department of Mechanical Engineering, Virginia Polytechnic Institute and State University.

[24] DeTurris, D. J., Schetz, D., and Hellbaum, R. F., 1990, "Direct Measurements of Skin Friction in a SCRAMjet Combustor," AIAA Paper 90-2342, July 1990.

[25] DeTurris, D. J., 1992, "A Technique for Direct Measurement of Skin Friction in Supersonic Combustion Flow," Doctor of Philosophy Dissertation, Department of Aerospace and Oceanographic Engineering, Virginia Polytechnic Institute and State University.

[26] Schetz, J. A., 2004, "Direct Measurement of Skin Friciton in Complex Flows using Movable Wall Elements," AIAA Paper 2004-2112, July 2004

Table 1. Experimental Uncertainties

		Value		Uncertainty		% Uncertainty	
		Low	**High**	**Low**	**High**	**Low**	**High**
(N = 1) S1/d = 2	C_D	4.04	4.03	± 0.16	± 0.14	± 3.95%	± 3.51%
	f_{array}	0.106	0.108	± 0.02	± 0.008	± 20.74%	± 7.56%
(N = 7) S1/d = 4, S2/d = 3.46	C_D	2.16	1.79	± 0.26	± 0.06	± 12.20%	± 3.55%
	f_{array}	0.071	0.064	± 0.011	± 0.005	± 15.13%	± 7.24%
(N = 7) S1/d = 4, S2/d = 3.46 α = 30°	C_D	1.55	1.49	± 0.12	± 0.05	± 7.55%	± 3.51%
	C_L	0.71	0.61	± 0.05	± 0.02	± 7.64%	± 3.58%
	Re	9,313	32,129	± 544	± 301	± 5.84%	± 0.94%
	Re_d	6,410	22,113	± 413	± 632	± 6.44%	± 2.86%

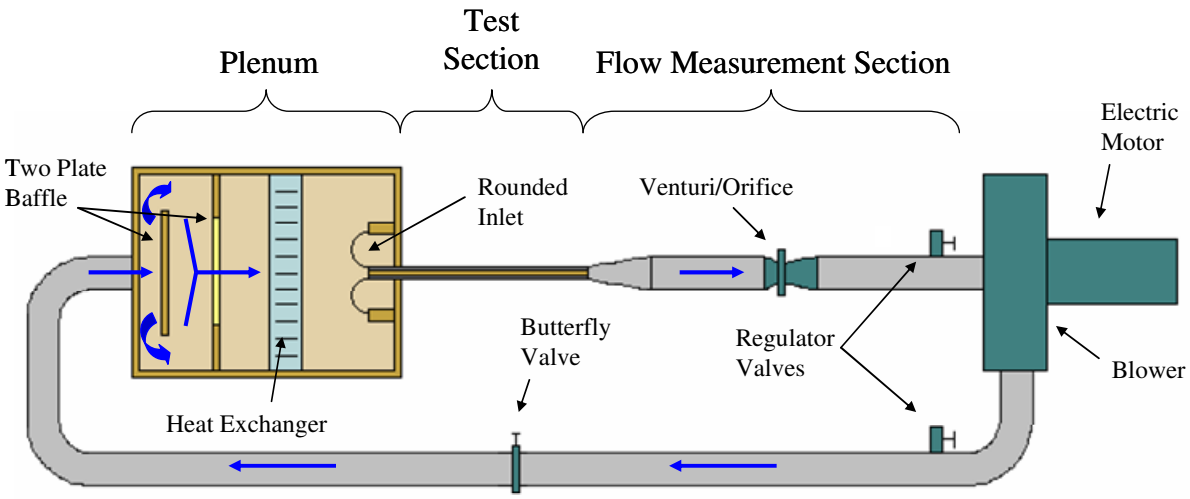

Figure 1. Schematic of the overall test facility used for all pin fin array testing.

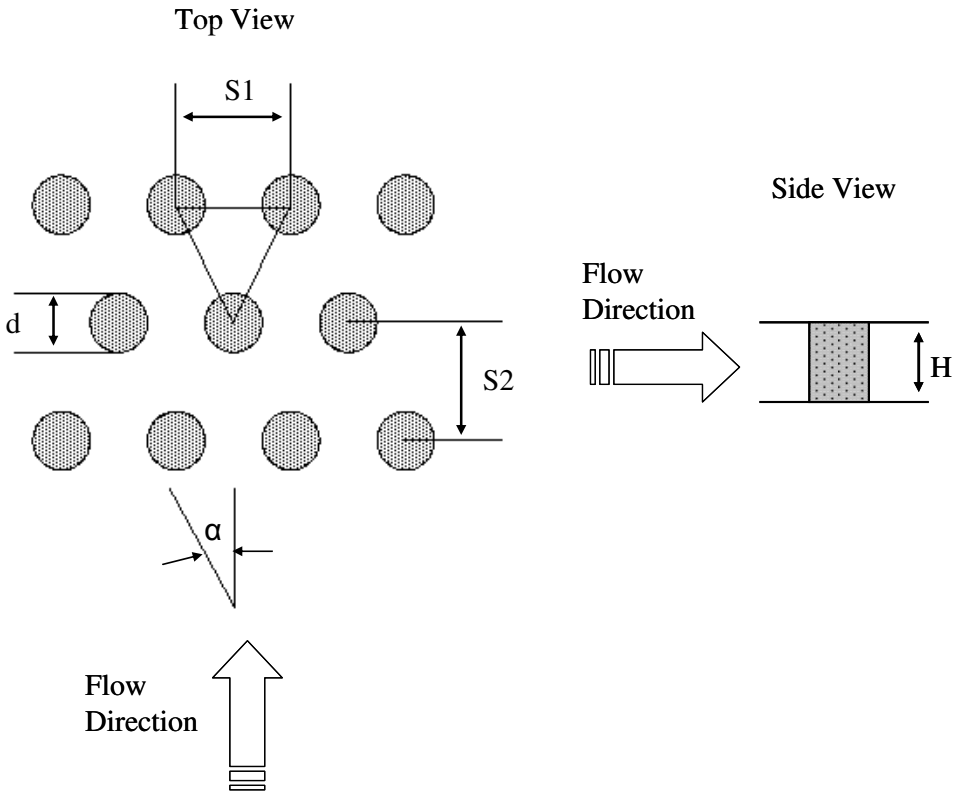

Figure 2. Pin fin array geometry and nomenclature.

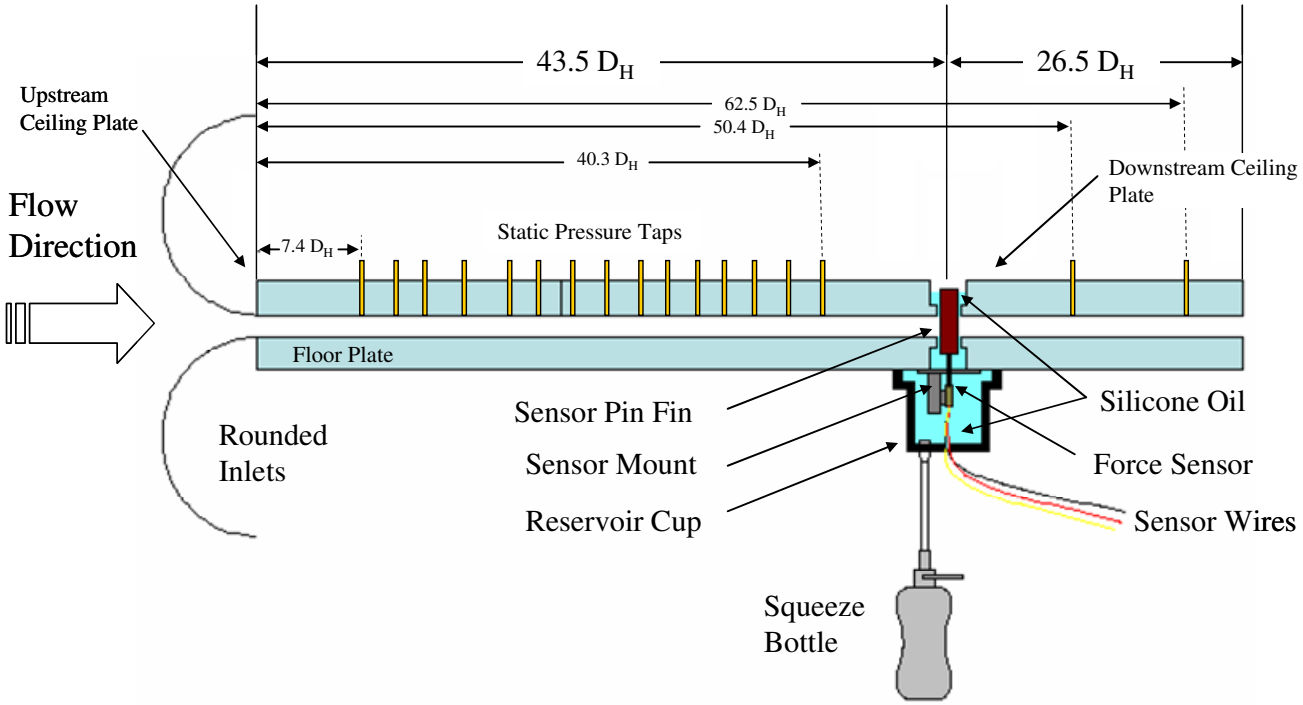

Figure 3. Schematic of the test section where all pin fin force and pressure drop measurements were made.

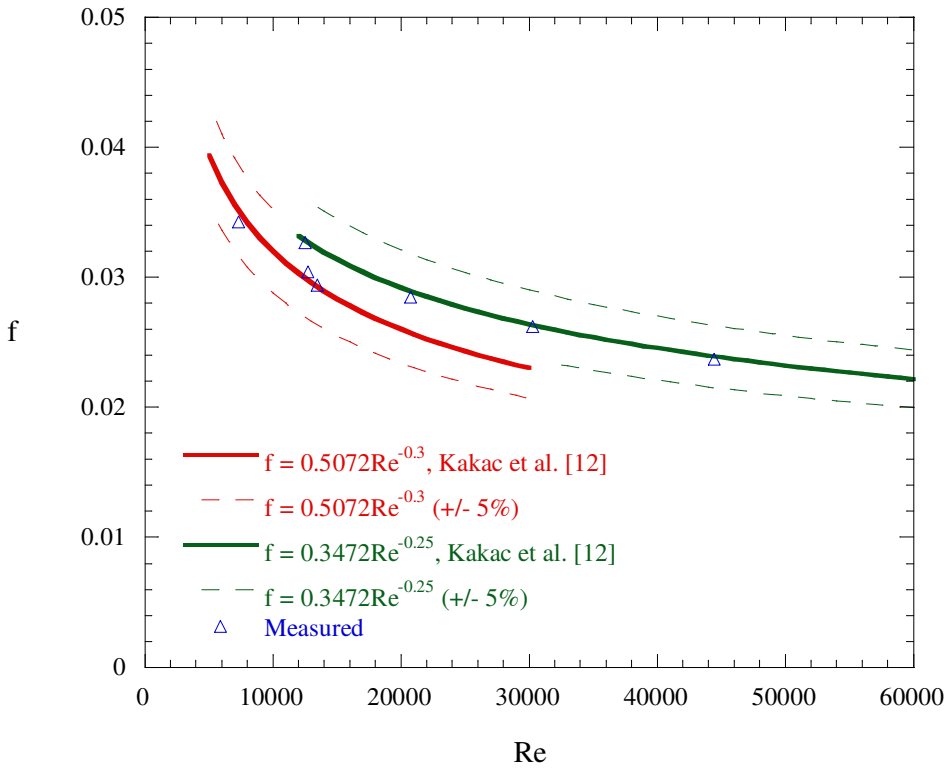

Figure 4. Plot of the empty channel friction factor results [15].

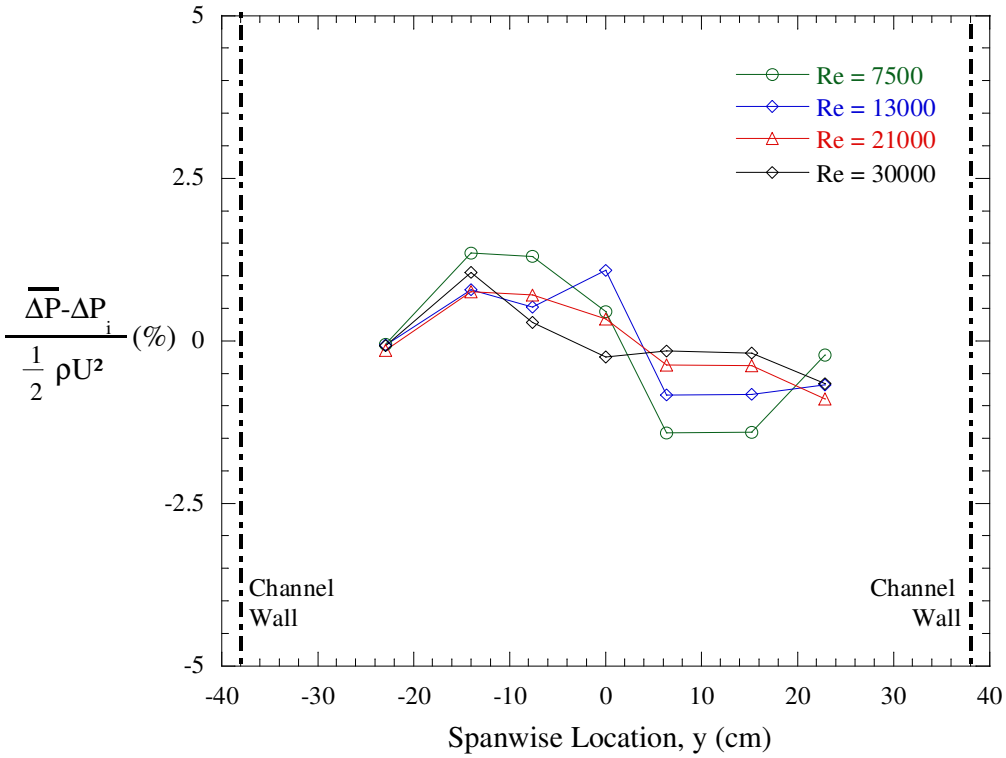

Figure 5. Plot of typical upstream spanwise static pressure distributions [15].

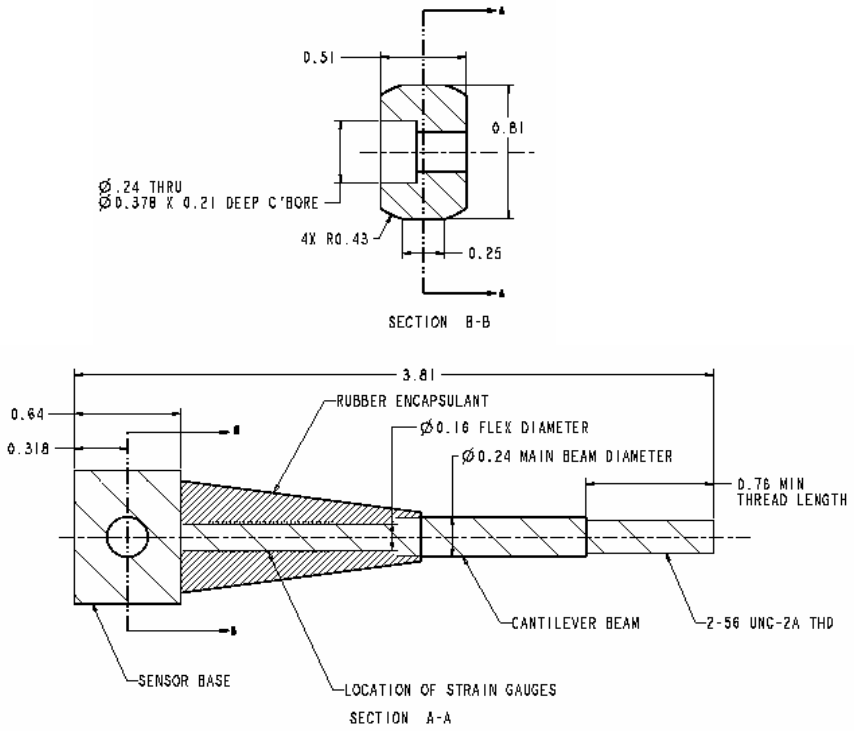

Figure 6. Diagram of pertinent DSC-6 force sensor dimensions in cm [16].

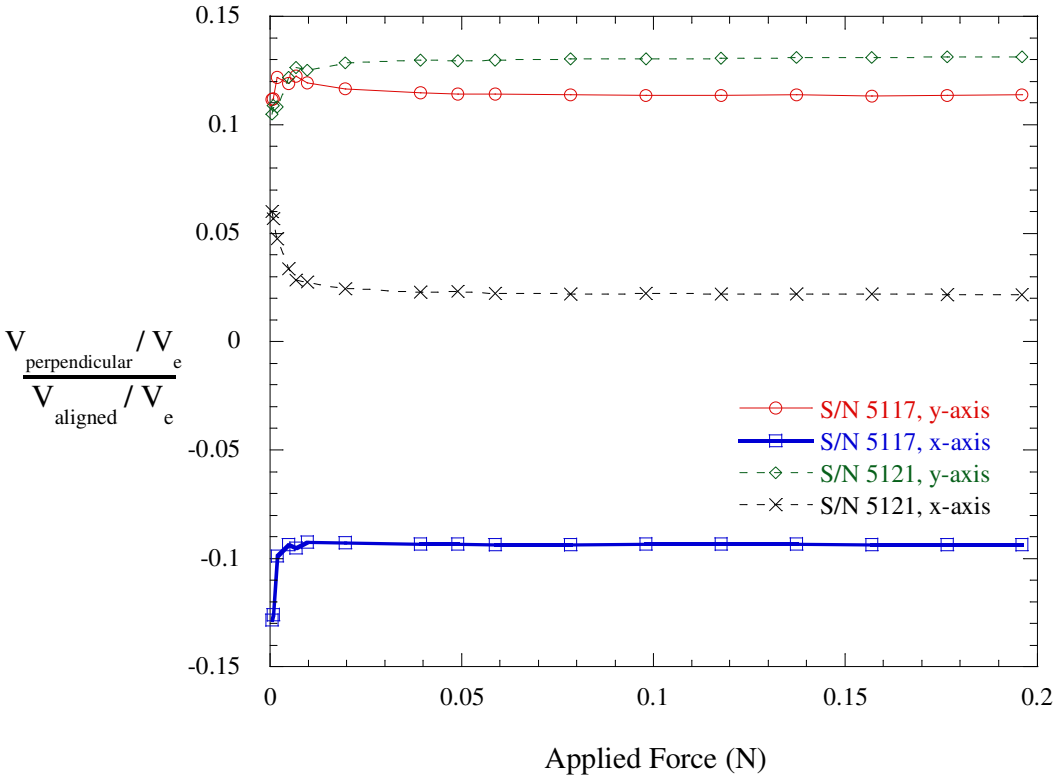

Figure 7. Plot demonstrating the cross axis sensitivity of four different sensor axes [15].

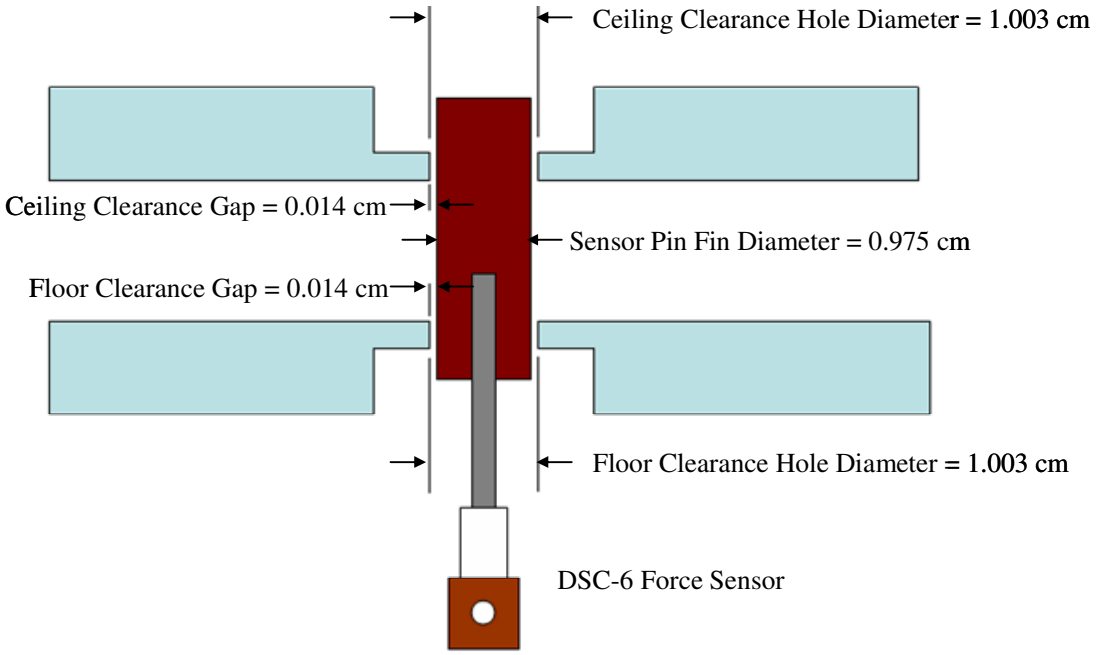

Figure 8. Dimensioned schematic of pertinent geometric information for the sensor pin fin clearance hole.

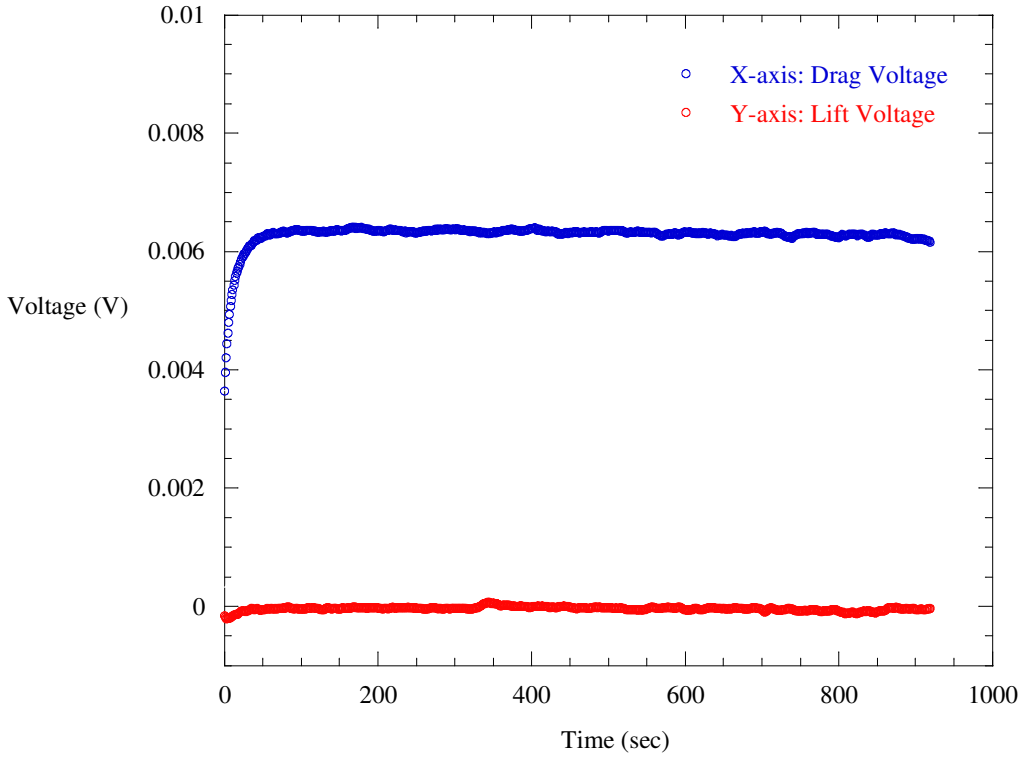

Figure 9. Plot of the cross-axis corrected voltages from the DSC-6 sensor output, specifically a Re = 24,000 flow for a single row of pin fins with an S1/d = 2.

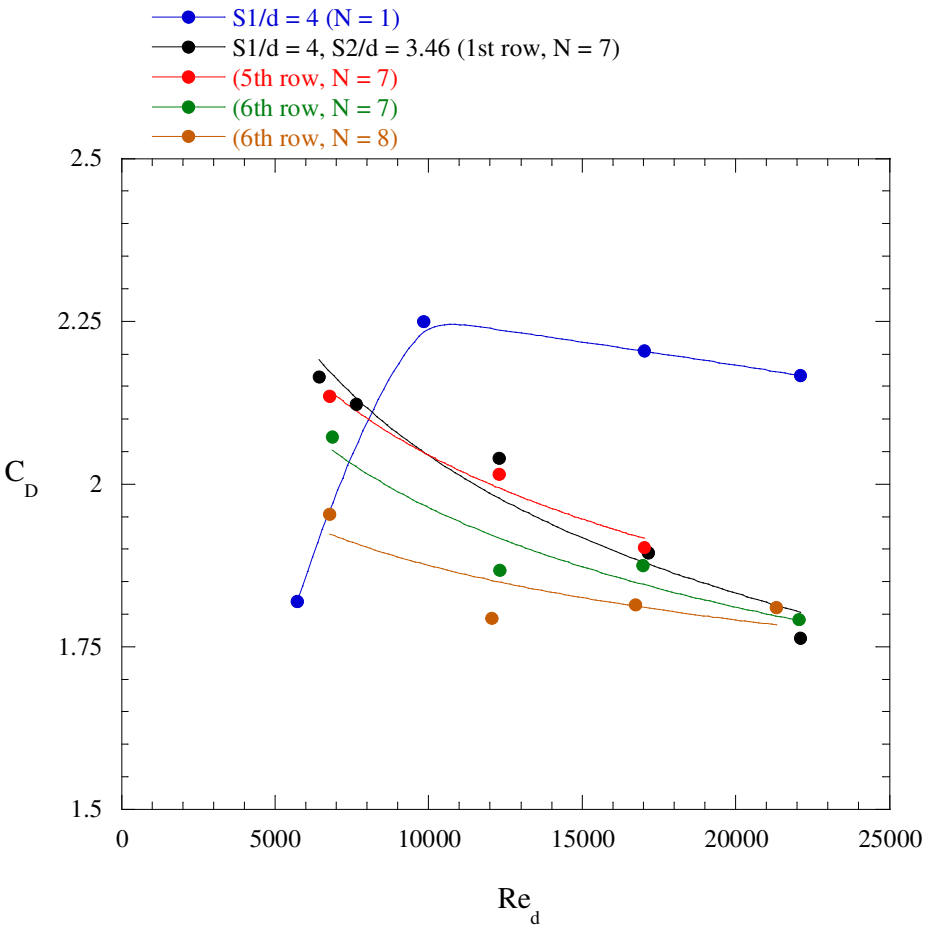

Figure 10. Plot comparing single versus staggered, multiple row array drag coefficients versus pin Reynolds number.

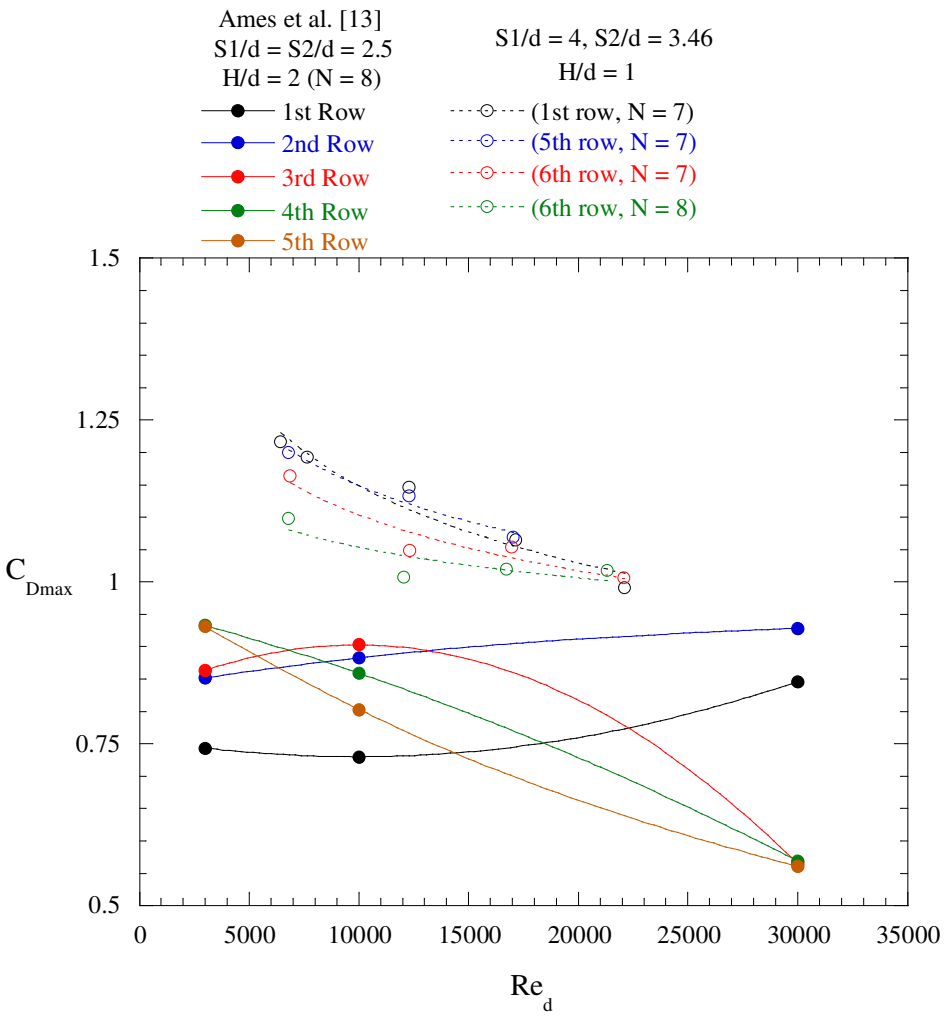

Figure 11. Plot comparing staggered, multiple row array drag coefficient results with pressure drag coefficient results obtained from Ames et al. [13] versus pin Reynolds number.

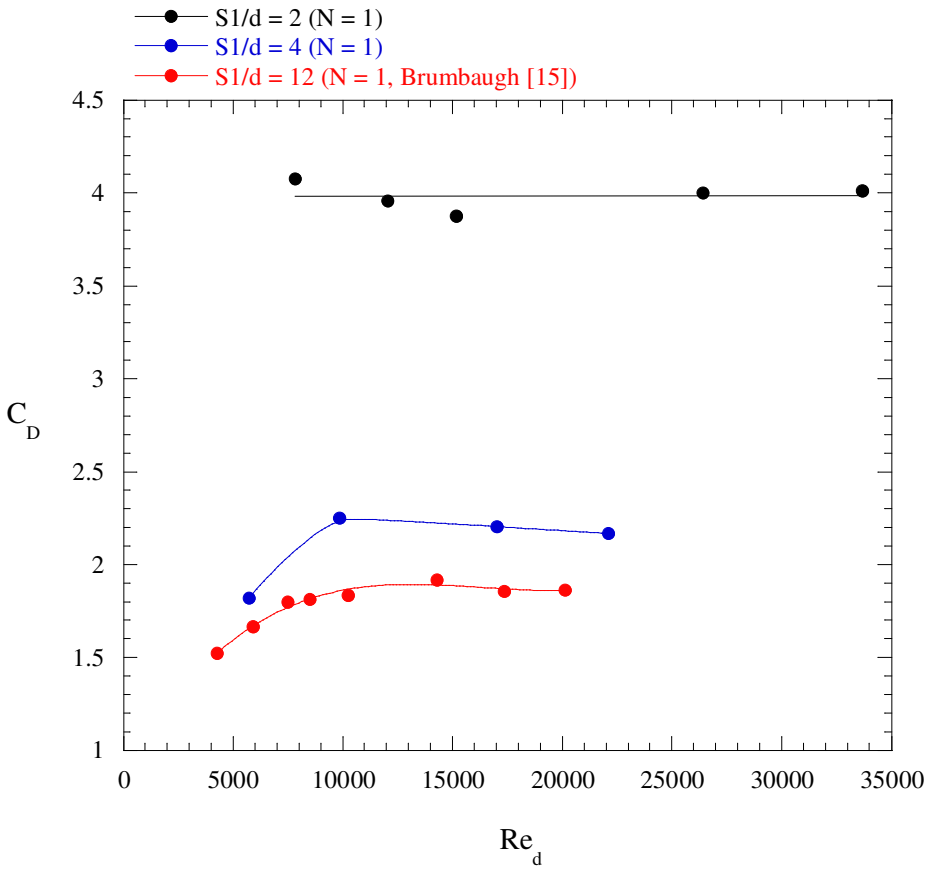

Figure 12. Plot comparing single row drag coefficient results for three different spanwise pin spacings versus pin Reynolds number.

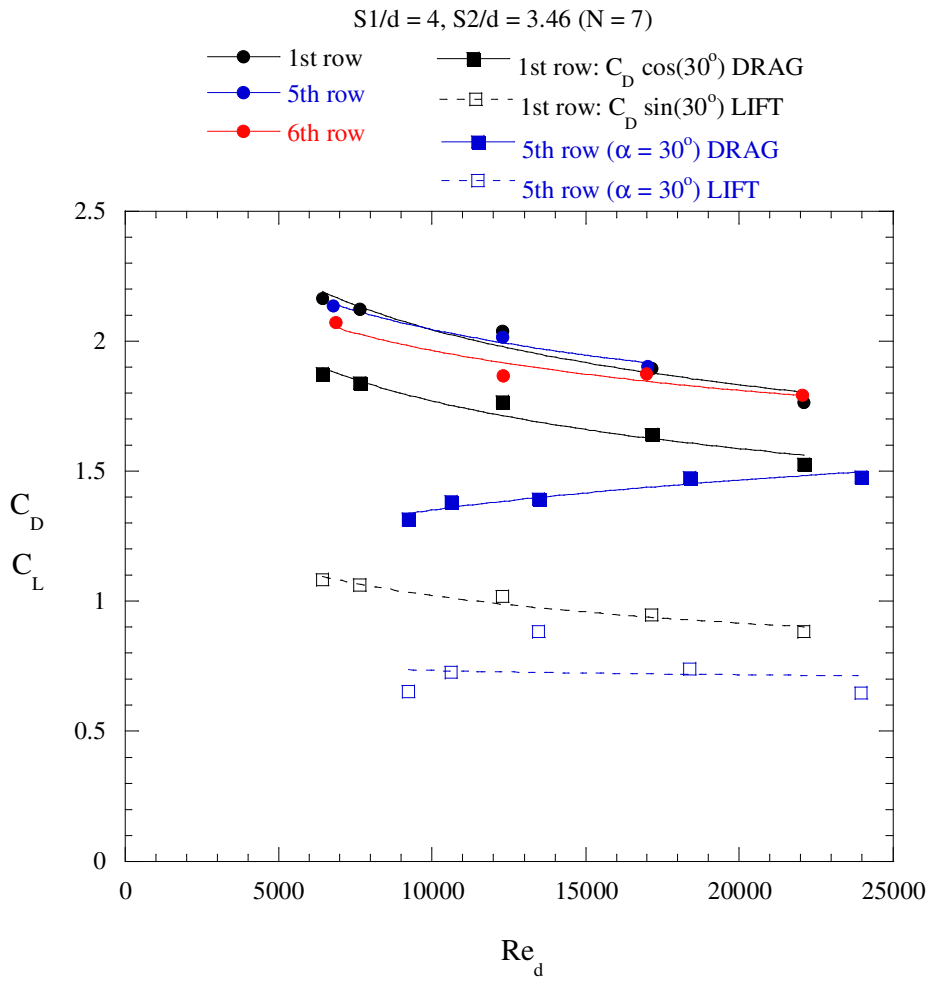

Figure 13. Plot comparing multiple row array drag and lift coefficient results for staggered and inline flow incidence angles versus pin Reynolds number.

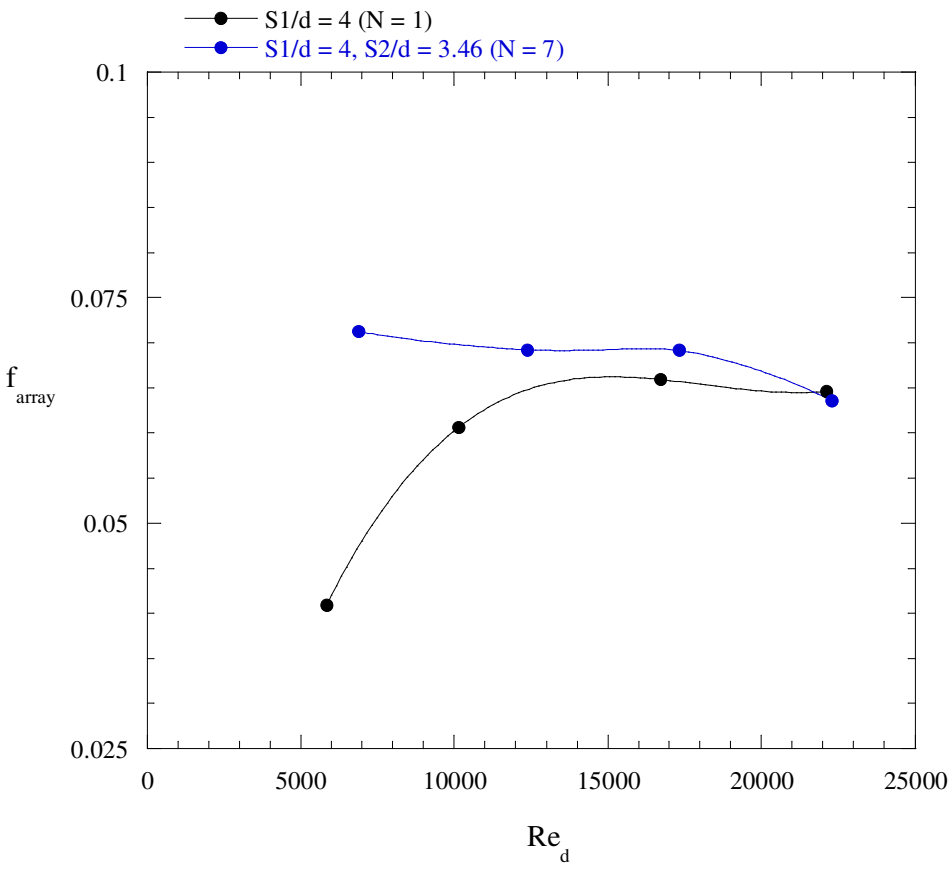

Figure 14. Plot comparing array friction factor results for both a single and multiple row array with identical spanwise pin spacings versus pin Reynolds number.

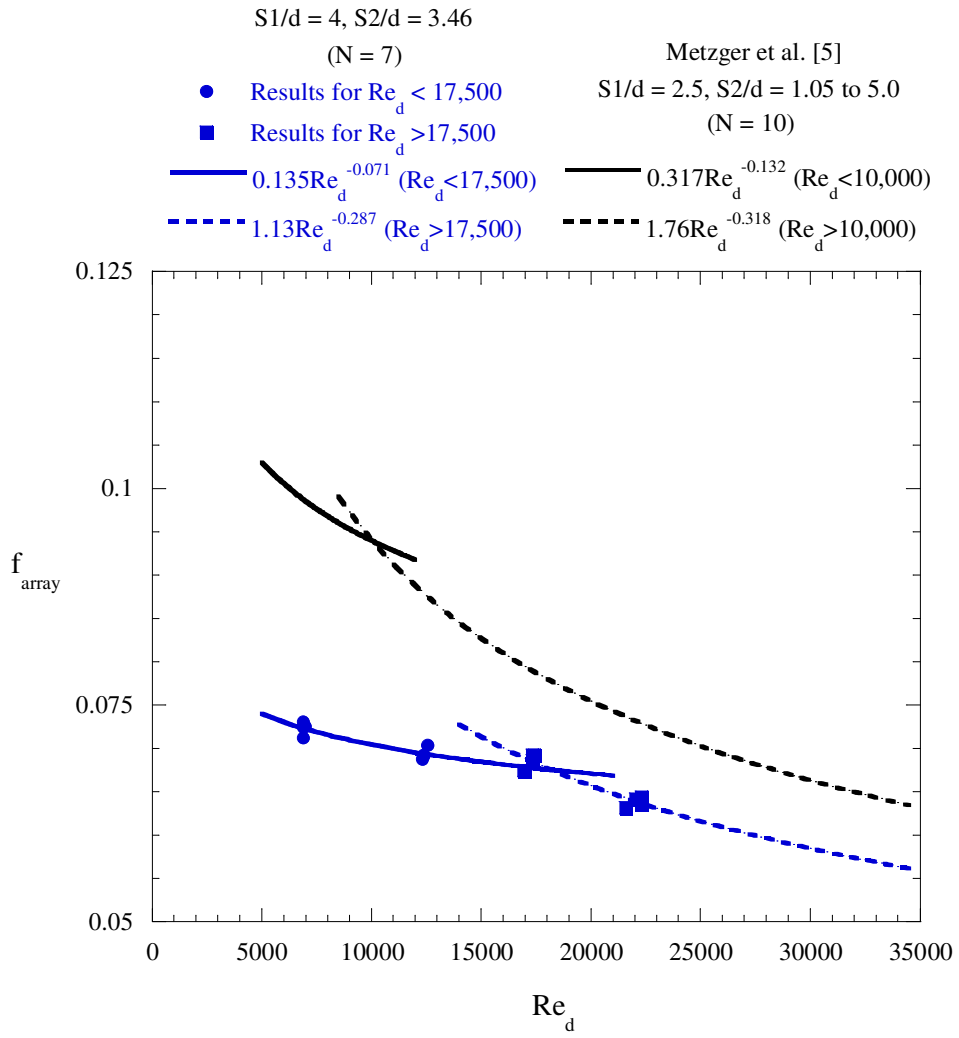

Figure 15. Plot comparing the dependence of array friction factor on pin Reynolds number with the correlated results of Metzger et al. [5] for multiple row arrays.

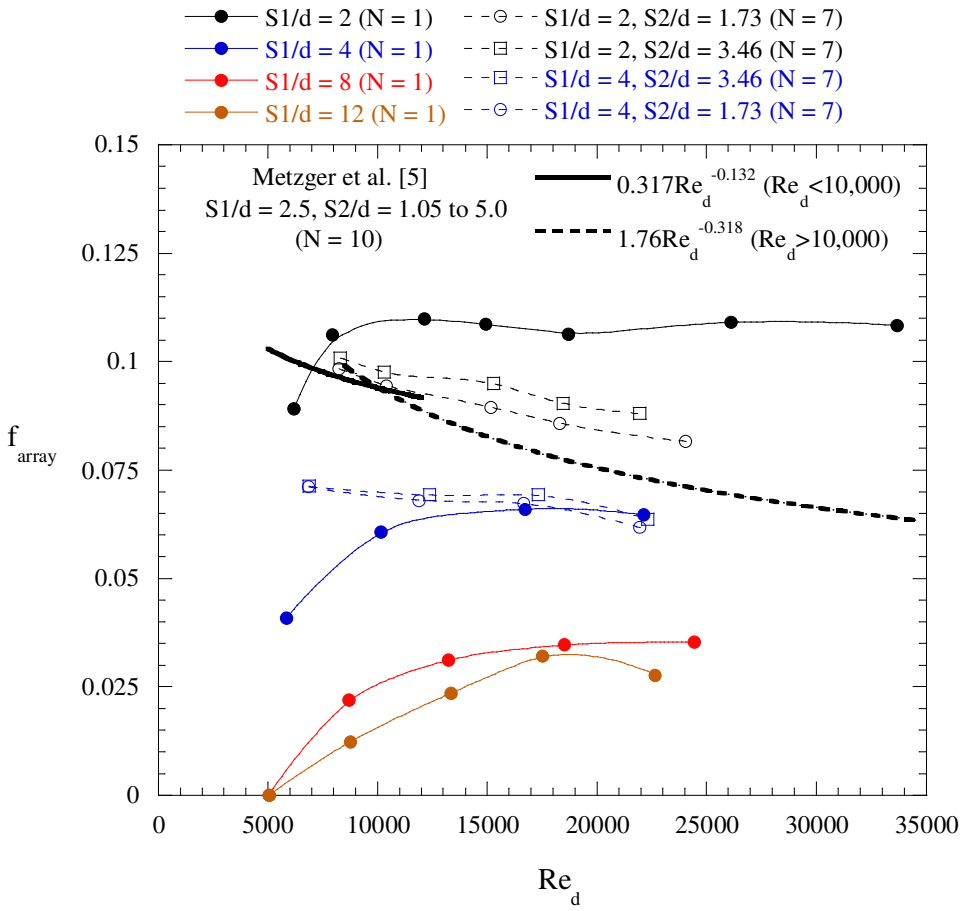

Figure 16. Plot comparing array friction factor trends for both single and multiple row arrays for several different spanwise and streamwise pin spacings with the correlated results of Metzger et al. [5] versus pin Reynolds number.

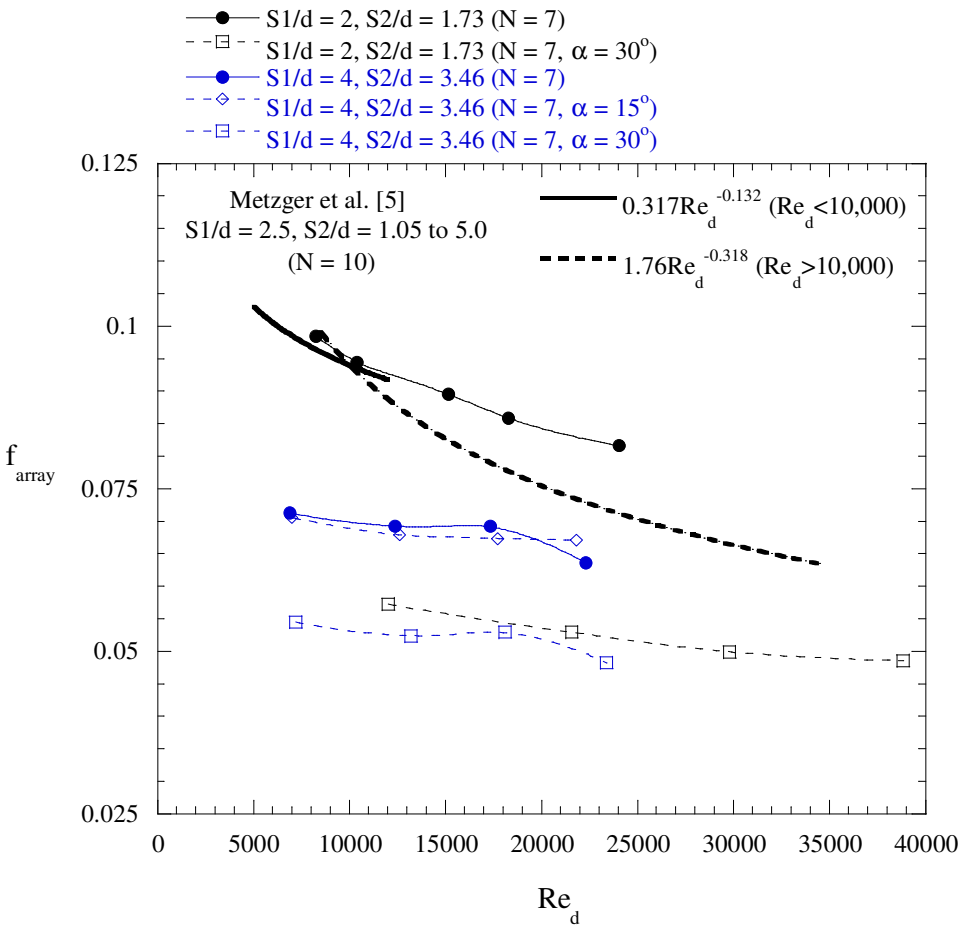

Figure 17. Plot comparing friction factor results for two differently spaced, multiple row arrays and there dependence on flow incidence angle with the correlated results of Metzger et al. [5] versus pin Reynolds number.

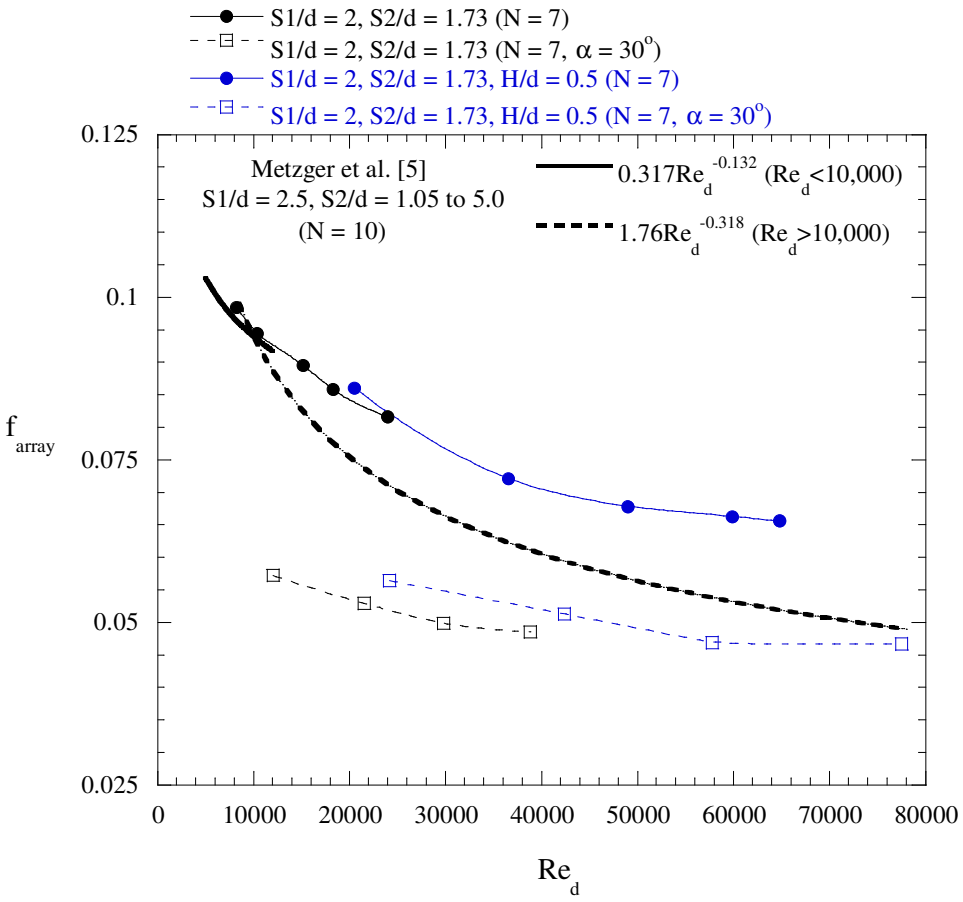

Figure 18. Plot comparing array friction factor results for two different pin aspect ratios and the effect of an inline flow incidence angle with the correlated results of Metzger et al. [5] versus pin Reynolds number.

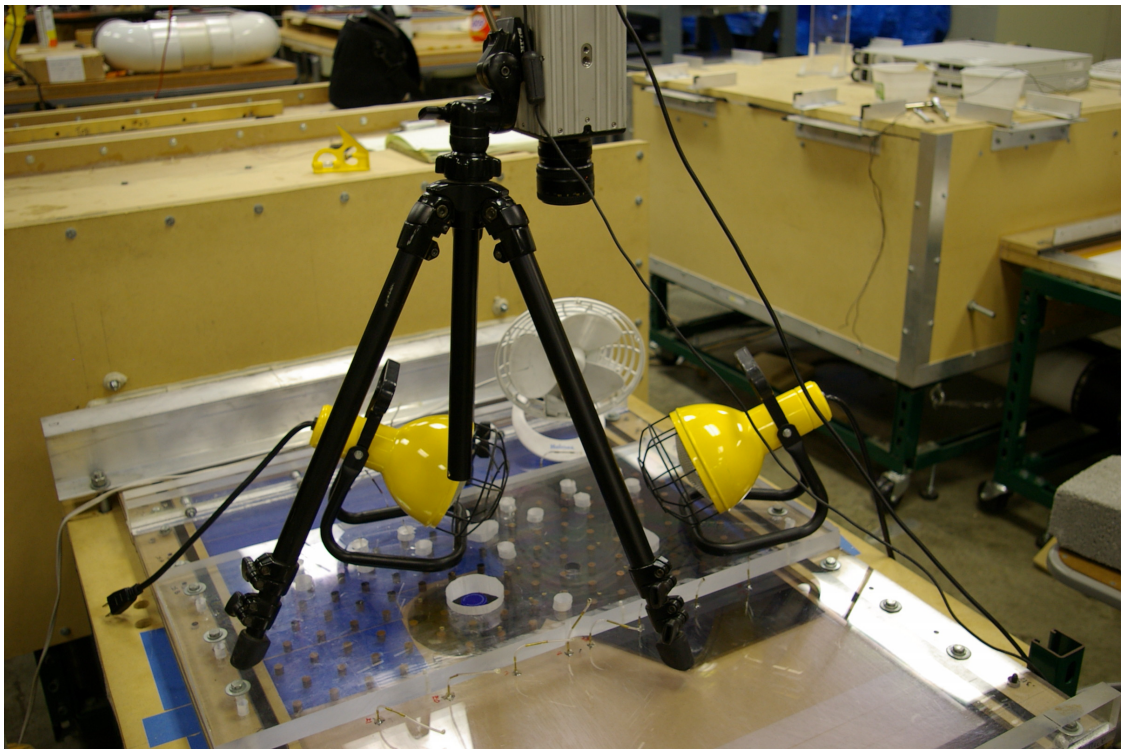

Figure 19. Photograph showing the setup of the high speed camera over the test channel viewing area. Also shown are the lights used to illuminate the area and the black background underneath the pins on the right side of the test channel.

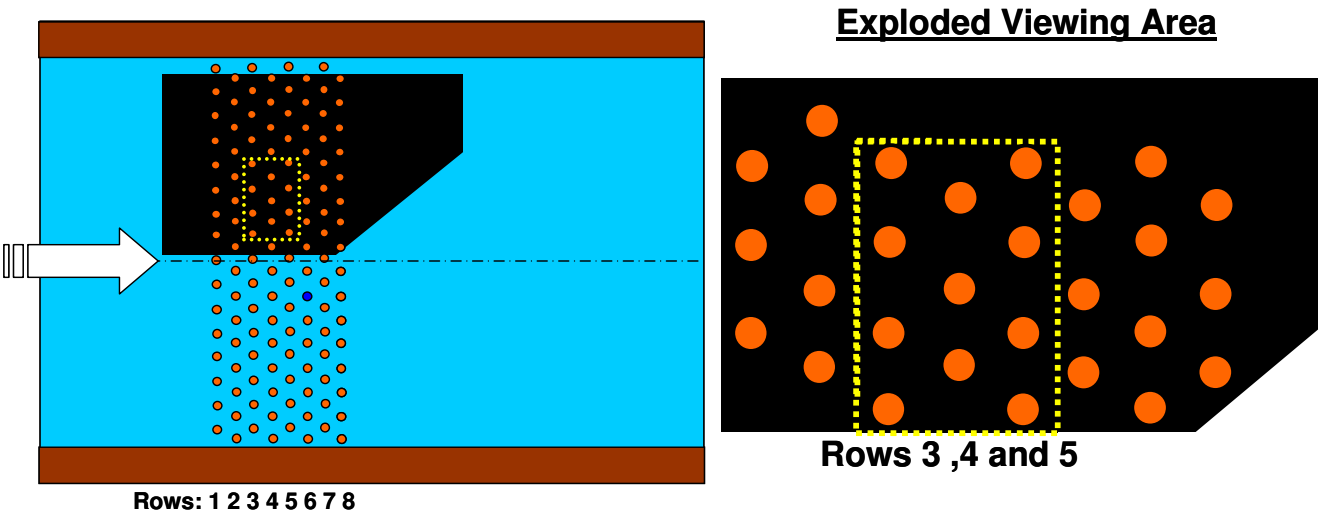

Figure 20. Schematic illustrating the location of the viewing area.

Figure 21. Photograph showing the location of the fog machine on the upstream side of the plenum.

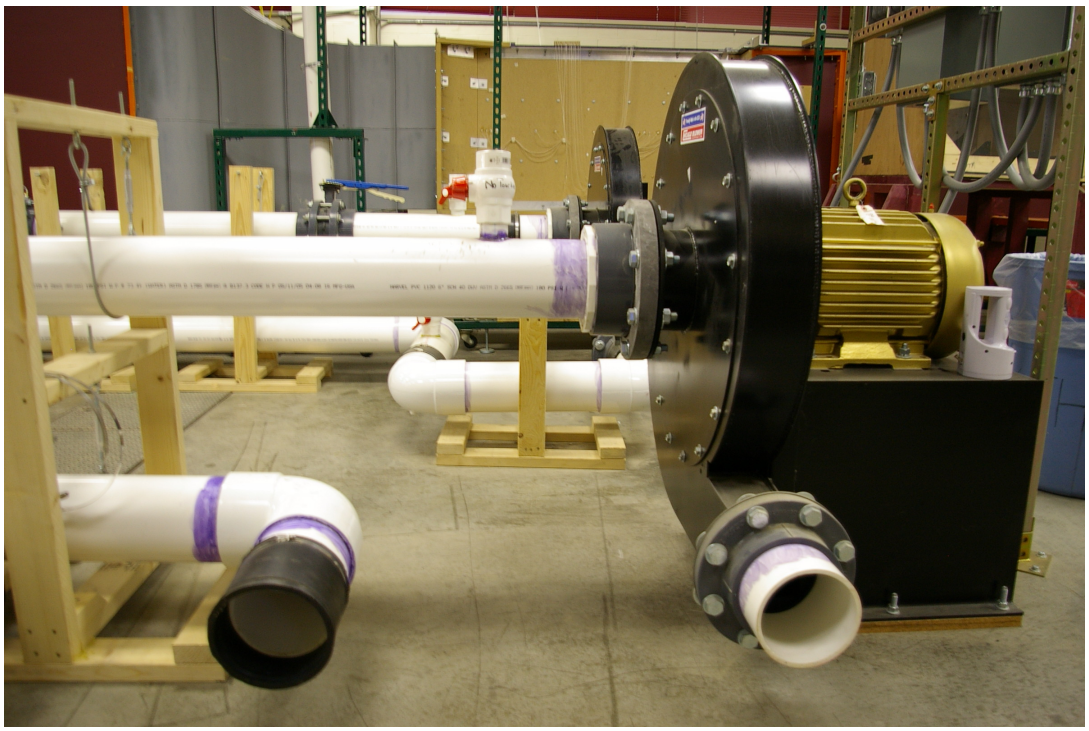

Figure 22. Photograph showing the recirculation pipe disconnected from the blower exit so that the rig could be operated under open loop conditions.

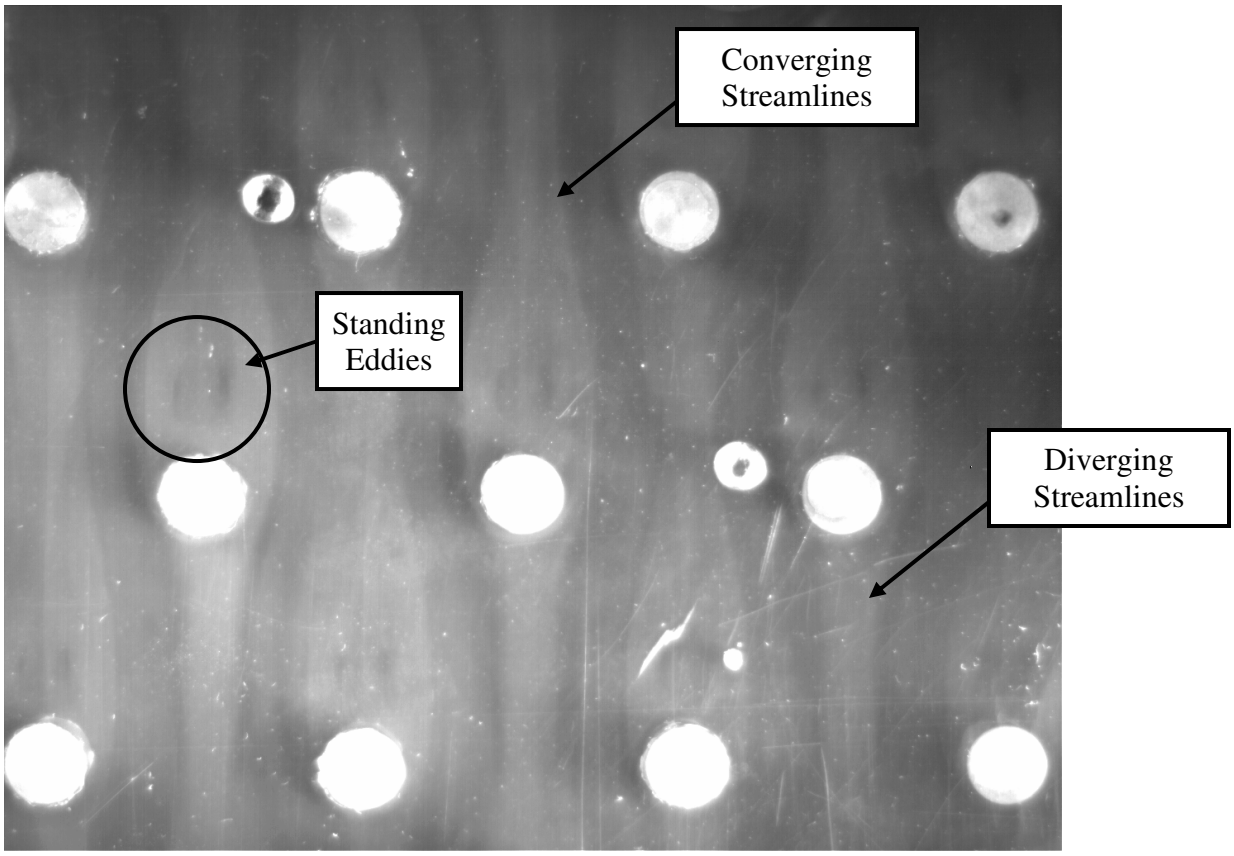

Figure 23. Annotated photograph showing the diverging and converging streamlines through the staggered pin fin array at a Re = 1,000. The location of two standing eddies on the downstream side of the pin fins are also shown.

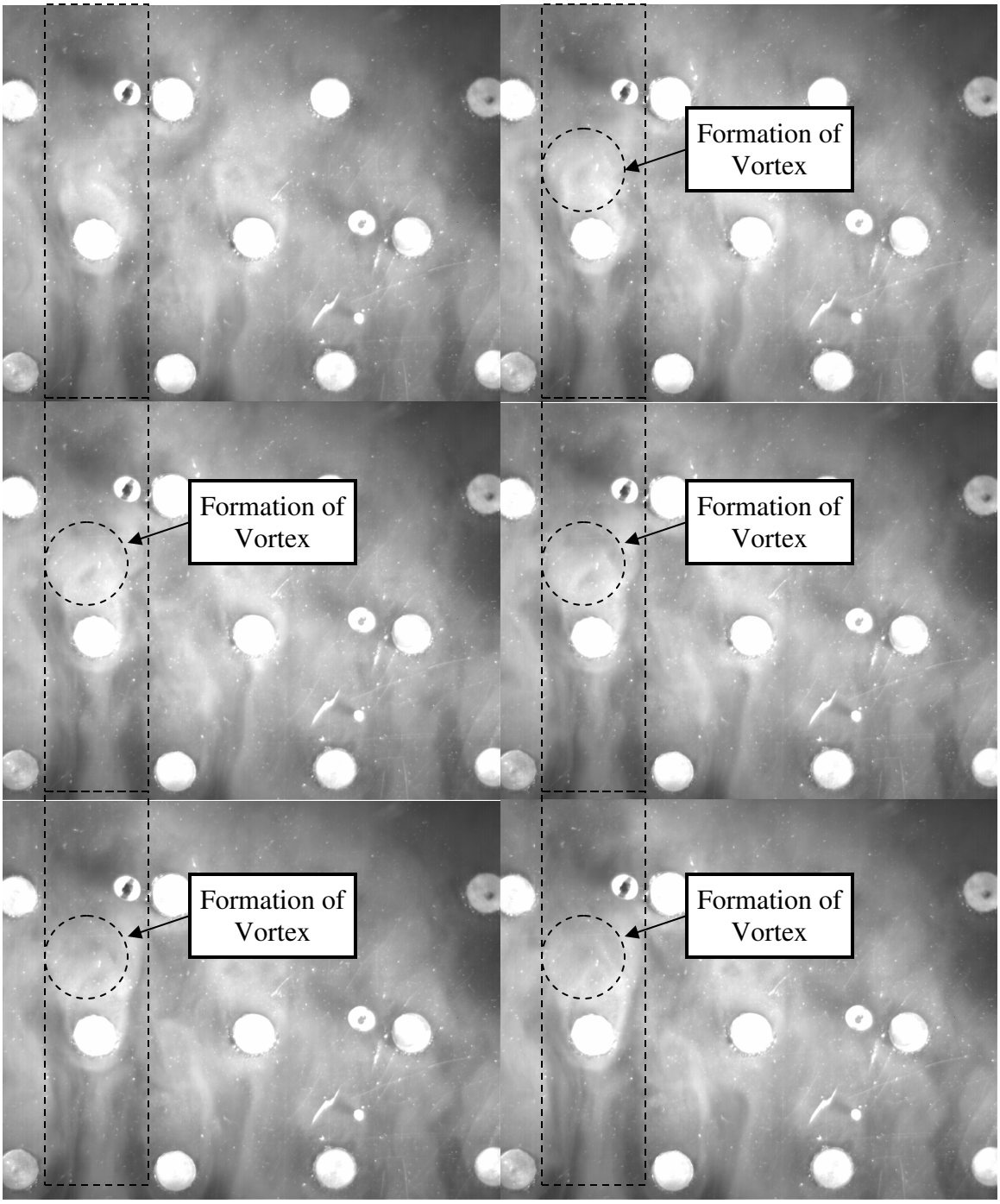

Figure 24. Annotated photographs showing the formation and shedding of a single vortex on the left side of a pin fin in the fourth row. The flow corresponds to a Reynolds number of approximately Re = 2,000.

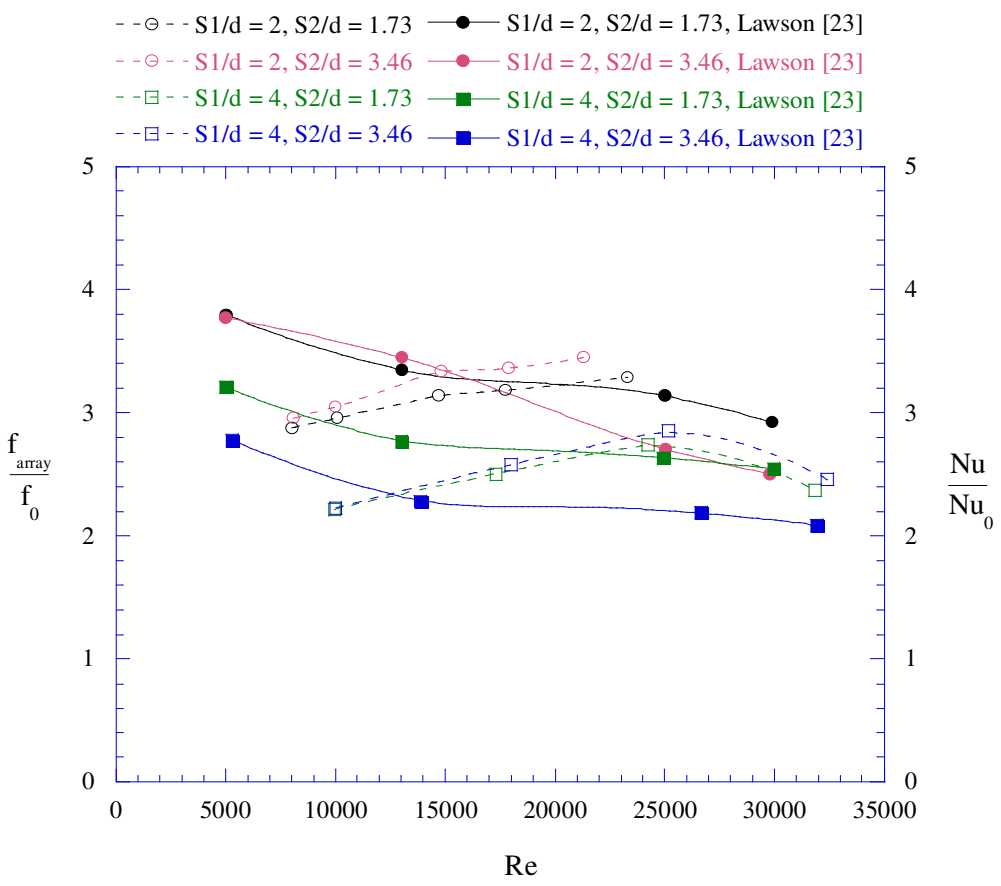

Figure 25. Plot comparing heat transfer and pressure drop augmentation trends for different spanwise and streamwise pin spacings versus channel Reynolds number.

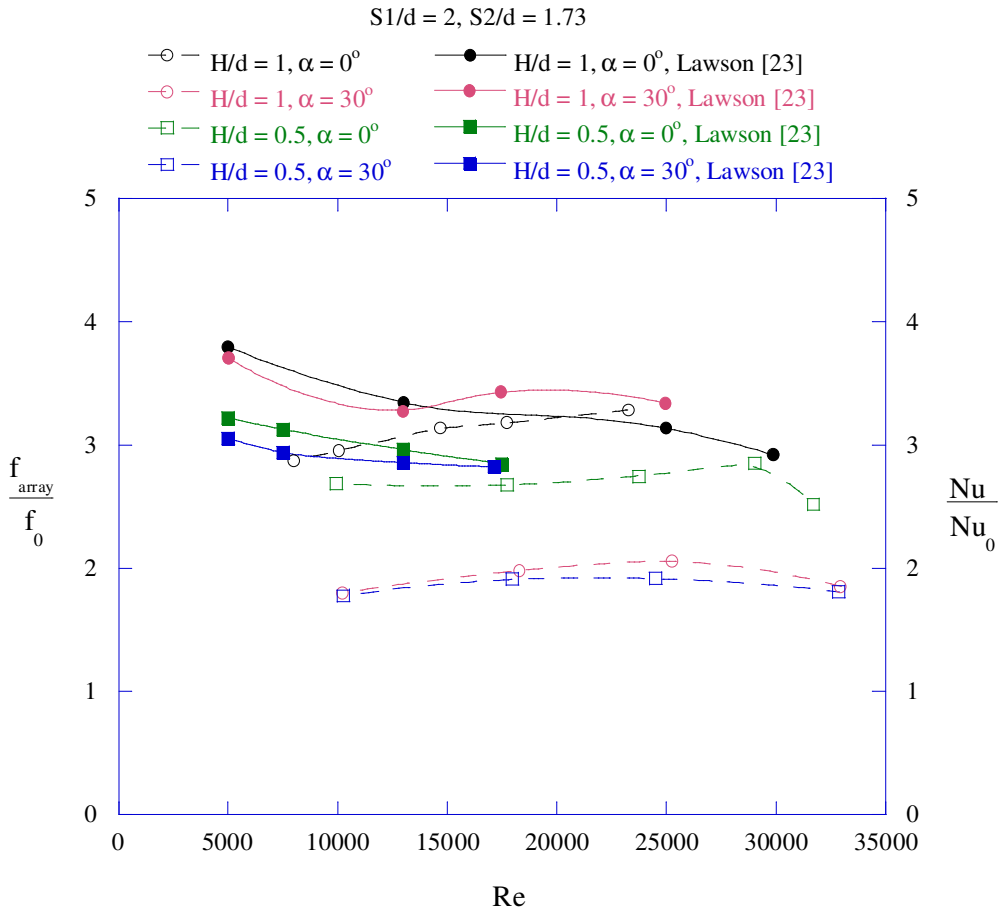

Figure 26. Plot comparing heat transfer and pressure drop augmentation trends related to flow incidence angle and pin aspect ratio for a multiple row array versus channel Reynolds number.

Appendix A: Test Section Benchmarking

The empty channel Darcy friction factor was calculated from static pressure measurements obtained from pressure taps 1-8, 15-17, 24, 32, 33 as listed in Table A.1 and as illustrated in Figure A.1. The pressure difference was found by using the first pressure tap as the reference high pressure and subtracting the pressure at each streamwise location. In this manner, the static pressure drop relative to the first pressure tap was plotted on a curve at the locations of the pressure taps mentioned above. The slope of the linear portion of the curve, obtained using a linear regression, represented the fully developed friction factor. Figure A.2 plots the relative static pressure drop for a Re = 13,000 flow and indicates the portion of the curve chosen for the calculation of the linear pressure drop. Figure A.2 shows that the slope of the pressure drop curve increases across the ceiling junction. This phenomenon, seen in every channel friction factor test, can be attributed to the slight area decrease that occurs across the junction of the two ceiling plates. The acceleration of the flow and thus the increase in pressure drop across the junction could not be completely eliminated and was instead tolerated because the flow still reaches a fully developed state, as indicated by the onset of the linear pressure drop in Figure A.2, approximately 26 hydraulic diameters from the entrance of the test channel. As shown in Figure 3 for a single row of pin fins the flow is allowed to develop for 43.5 hydraulic diameters. However, the entrance length could vary when testing was performed on a pin fin array depending on which row the sensor pin fin was located in since the array had to be shifted with respect to the sensor pin fin, as its location was fixed. Furthermore, if the array were angled with respect to the flow the entrance length would be even smaller. The smallest entrance length encountered during force and pressure drop measurement testing was for the array with S1/d = 4, S2/d = 3.46, 7 row, staggered configuration angled at 30° to the incoming flow with the sensor pin fin located in the fifth row as shown in Figure A.3. The entrance length in this case is 28 hydraulic diameters, which is still greater than the required entrance length for development ensuring that the flow is fully developed before encountering the pin fin array.

The measured friction factors showed agreement with the published correlations to within 2.5% over the Reynolds number range tested. Table A.2 summarizes the friction factor results from Figure 4 and also shows that the R^2 value, from the linear regression used in calculating the pressure drop, for each friction factor result exceeded 0.98 indicating that the

static pressure decreased linearly in the channel. This supported the conclusion that the flow is fully developed and that the desired channel flows are in place.

Spanwise uniformity was assessed using those pressure taps shown in Figure A.1 which span the width of the test section and are located at least upstream of the force sensor pin fin. For a single row of pin fins and for a non-angled pin fin array the static pressure of any given pressure tap in a given row of upstream pressure taps never varied by more than 2.5% from the average static pressure of that row, when normalized by the dynamic pressure head. Here again the static pressure was being measured in reference to the first pressure tap in the channel. Figure 5 provides a typical plot of the upstream spanwise static pressure distribution for four different flow conditions. The plot shows that all four cases fall within the 2.5% criterion and that the pressure distributions appear random across the span. For angled pin fin arrays however this was not the case since the flow is affected by the non-symmetric obstruction as shown in Figure A.3. In this situation the upstream static pressure distribution is necessarily non-uniform across the span since the flow is incompressible and must begin accommodating for the downstream obstruction prior to reaching it. As shown in Figure A.4 for four different flow conditions for a S1/d = 4, S2/d = 3.46, 7 row, staggered array angled at 30° to the incoming flow, the static pressure is higher on the side of the channel where the angled array is protruding upstream resulting in a negative variation from the average row static pressure. The plot shows that the variation from the average row static pressure can be as large as 11% when normalized with the dynamic pressure head. For a pin fin array angled at 15º to the incoming flow the spanwise pressure uniformity upstream of the array shows a similar trend across the width of the channel, but due to the less extreme angle the variation was still never more than 2.5% from the average static pressure, when normalized with the dynamic pressure head.

Table A.1. Test section Pressure Tap Locations.

Pressure Tap	x - Streamwise (cm)	y - Spanwise (cm)	x - Streamwise (D_H)	y - Spanwise (D_H)
1	14.0	0.0	7.4	0.0
2	19.1	0.0	10.1	0.0
3	21.6	0.0	11.4	0.0
4	30.5	0.0	16.1	0.0
5	30.5	3.8	16.1	2.0
6	35.6	0.0	18.8	0.0
7	38.1	0.0	20.2	0.0
8	45.7	0.0	24.2	0.0
9	48.9	-7.6	25.9	-4.0
10	48.9	-15.2	25.9	-8.1
11	48.9	-22.9	25.9	-12.1
12	48.9	7.6	25.9	4.0
13	48.9	15.2	25.9	8.1
14	48.9	22.9	25.9	12.1
15	49.5	0.0	26.2	0.0
16	53.3	1.3	28.2	0.7
17	57.7	0.0	30.5	0.0
18	57.7	-7.6	30.5	-4.0
19	57.7	-15.2	30.5	-8.1
20	57.7	-22.9	30.5	-12.1
21	57.7	7.6	30.5	4.0
22	57.7	15.2	30.5	8.1
23	57.7	21.6	30.5	11.4
24	62.2	0.0	32.9	0.0
25	66.0	0.0	34.9	0.0
26	66.0	-6.4	34.9	-3.4
27	66.0	-15.2	34.9	-8.1
28	66.0	-22.9	34.9	-12.1
29	66.0	7.6	34.9	4.0
30	66.0	14.0	34.9	7.4
31	66.0	22.9	34.9	12.1
32	71.1	0.0	37.6	0.0
33	76.2	-1.3	40.3	-0.7
34	95.3	-1.3	50.4	-0.7
35	95.3	-7.6	50.4	-4.0
36	95.3	-15.2	50.4	-8.1
37	95.3	-22.9	50.4	-12.1
38	95.3	1.3	50.4	0.7
39	95.3	7.6	50.4	4.0
40	95.3	15.2	50.4	8.1
41	95.3	22.9	50.4	12.1

42	118.1	0.0	62.5	0.0
43	118.1	-8.9	62.5	-4.7
44	118.1	-15.2	62.5	-8.1
45	118.1	-22.9	62.5	-12.1
46	118.1	7.6	62.5	4.0
47	118.1	15.2	62.5	8.1
48	118.1	22.9	62.5	12.1

Table A.2. Summary of Friction Factors Obtained from Linear Curve Fits [15].

Re	Measured f	R^2	Predicted f Kakac, et al. [12]	%△
7340	0.034	1.000	0.0351	-2.45%
12526	0.033	1.000	0.0328	-0.46%
12714	0.030	0.999	0.0298	2.17%
13440	0.029	0.986	0.0293	0.43%
20776	0.028	0.999	0.0289	-1.61%
30286	0.026	0.998	0.0263	-0.38%
44445	0.024	0.992	0.0239	-0.95%

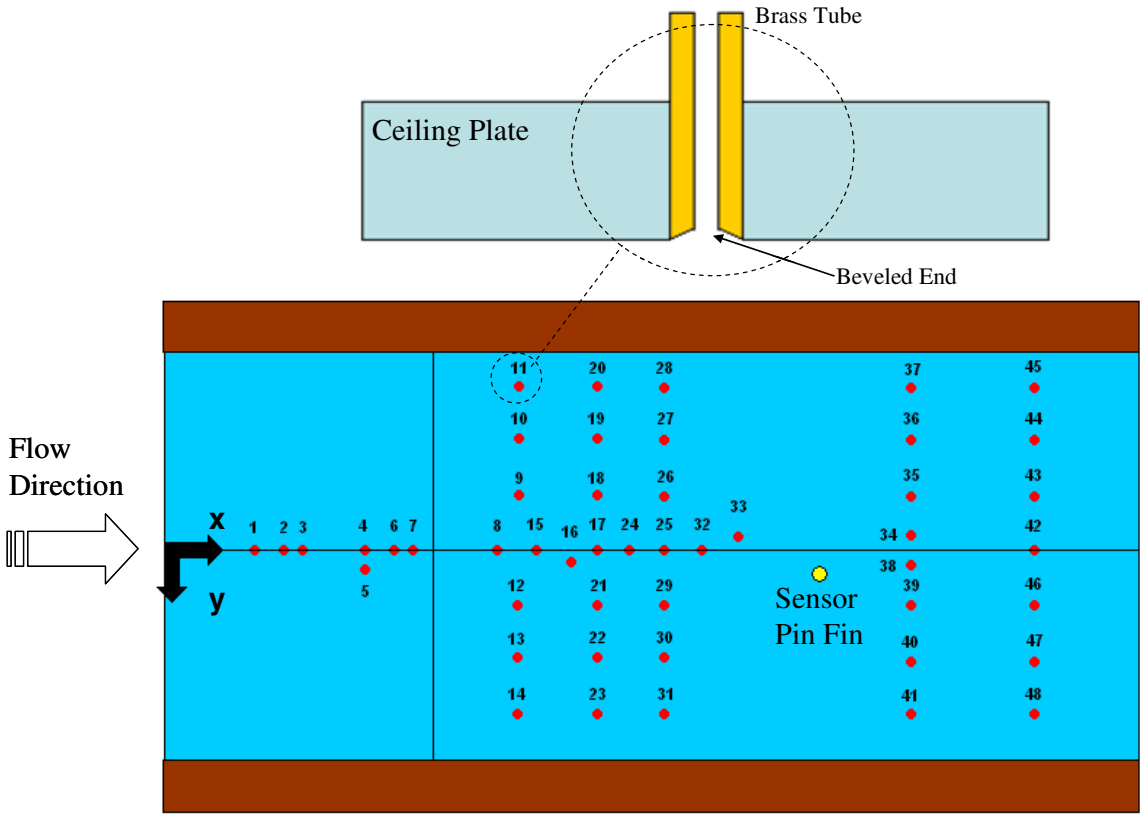

Figure A.1. Schematic of the static pressure tap layout in the test section ceiling.

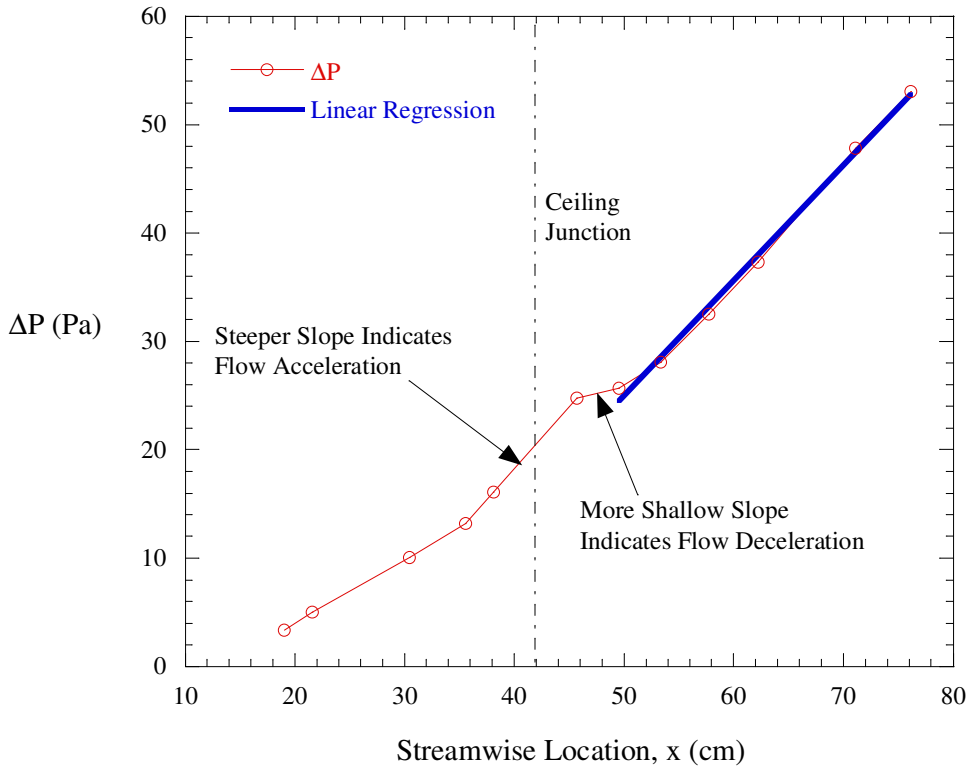

Figure A.2. Plot of the static pressure difference down the length of the channel for a Re = 13,000 flow [15].

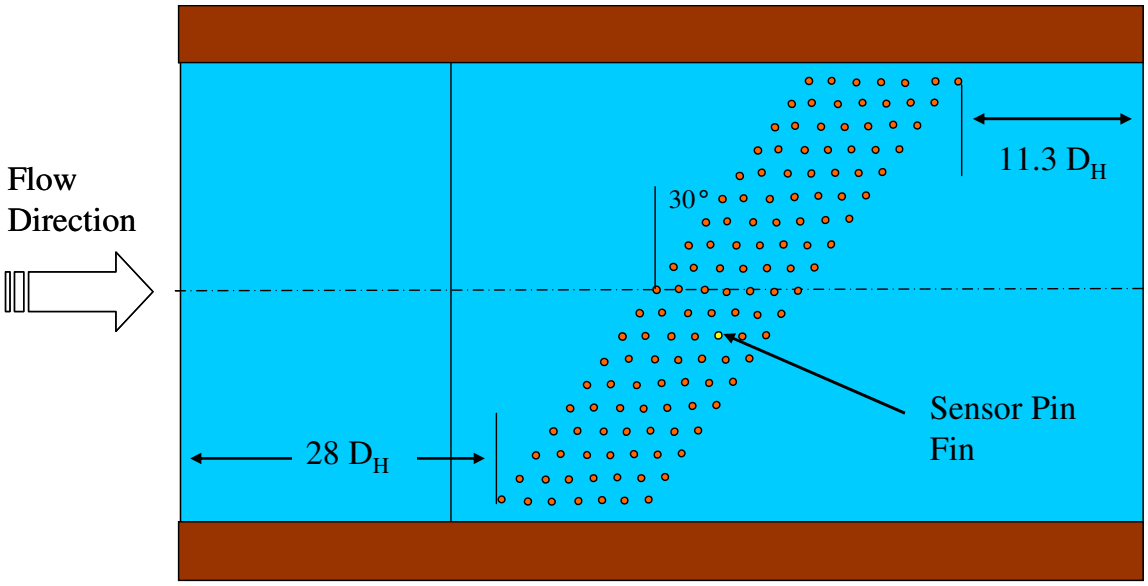

Figure A.3. Schematic of a staggered pin fin array layout for an S1/d = 4, S2/d = 3.46, 7 row array, angled at 30° to the incoming flow with the force sensor pin fin in the 5th row.

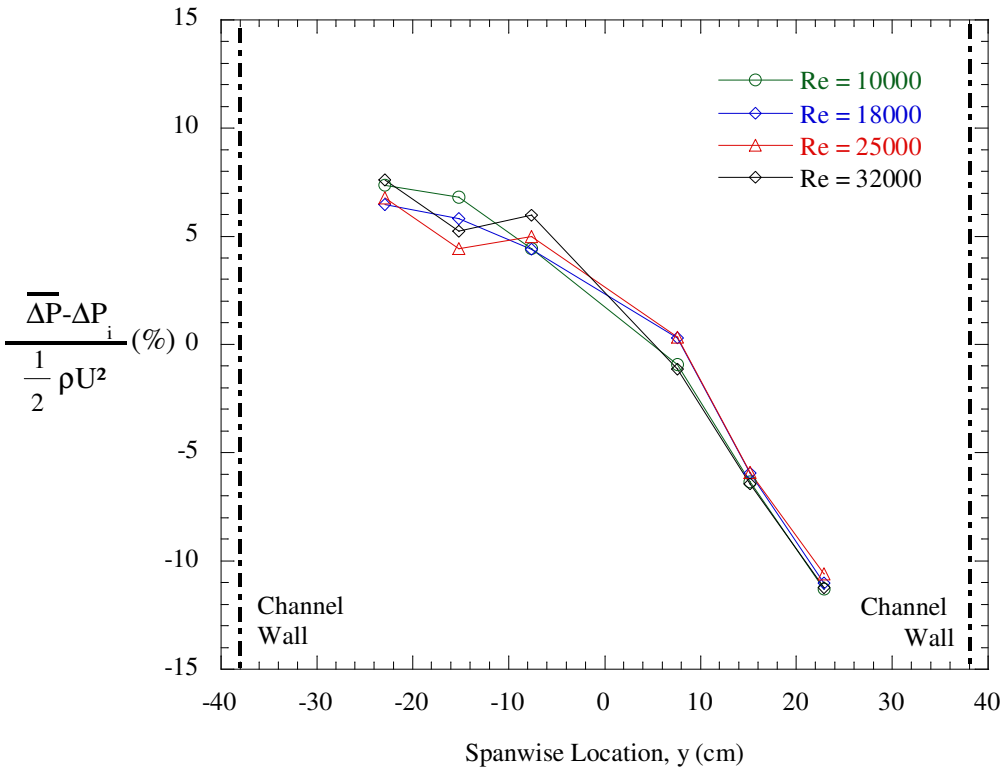

Figure A.4. Plot of the spanwise static pressure distributions upstream of an S1/d = 4, S2/d = 3.46, 7 row, staggered array angled at 30º to the incoming flow.

Appendix B: DSC-6 Force Sensor and Calibration Methodology

While several force sensors, shown in Table B.1, were used during calibration and investigation of the DSC-6 force sensors behavior, only one sensor was used for obtaining pin fin force measurements. The DSC-6 force sensor with serial number 5121 was chosen based on the overall performance of the force sensor during use and calibration. Unless otherwise noted all sensor output and force measurement results shown were produced using this particular two axis force sensor.

The DSC-6 force sensor is sensitive to several environmental factors. First, the semiconductor strain gauges used on the DSC-6 are extremely temperature sensitive. The manufacturer reports that the temperature sensitivity of the DSC-6 is approximately 0.054%/°C/full scale loading [16]. Fortunately, the sensor is submerged in a silicone oil bath which, as verified by a thermocouple within the silicone reservoir cup, keeps temperature changes under 0.05°C over the time period required for force measurement testing. Temperature effects also indirectly limit the sensitivity of the DSC-6 force sensor as related to the excitation voltage, V_e in Equation 3. Although Equation 3 shows that increasing the bridge excitation voltage increases the sensitivity of the force sensor, increased excitation voltage also means increased power dissipation manifested in the form of heat generation within the sensor strain gauge resistors. This leads to temperature increase so it is by no coincidence that calibration tests conducted with a single axis DSC-6 force sensor using three different excitation voltages (2V, 5V, and 10V) showed that the lowest excitation voltage yielded the better results as shown in Figure B.1. For this reason the DSC-6 force sensor was powered with 2V of excitation for each axis throughout testing.

A second environmental effect on the force sensor output is light exposure. Changing intensities in light level result in changing output voltages from each axis of the force sensor. Conversely, the degree of light sensitivity appears to be independent of the bridge excitation voltage. To illustrate the effect of light on the force sensor output, Figure B.2 plots the force sensor output from the two axis force sensor with serial number 5120 versus time for what was considered a drift test since the force sensor was not loaded. The test was conducted by covering the force sensor with a sheet, turning off the lights, and allowing the force sensor to drift over night. The next morning, the lights were turned on and the cover sheet removed. Figure B.2

shows that the sensor jumps by 7.0 X 10^{-4} N and 9.1 X 10^{-4} N, respectively, when the force sensor is covered and uncovered with the sheet. Removing the cover sheet changes the sensor output by 30% of the lowest drag force measured on a single pin fin during testing.

Although this sensitivity is currently neither documenter nor understood it is unlikely that it is related to electrical noise or heating effects. This was proven by shining a battery operated flashlight on the DSC-6 force sensor. The flash light is a DC circuit; therefore it cannot impose electrical noise on the DSC-6 force sensor. Passing the flashlight beam over the sensor results in an output voltage change where the polarity of the voltage change could be switched by switching which side of the force sensor the light beam was incident upon. This phenomenon was observed to occur with the flash light greater than 5 m away from the sensor, eliminating the possibility that the heat generated by the incident light caused the voltage change. Regardless as long as the light level is constant during use of the force sensor, the light presents only a bias error that can be nulled before conducting a force measurement or calibration test.

The final parameter affecting sensor performance is the sensor's forcing history. Kistler Morse suggest deflecting the DSC-6 force sensor to full scale ten times in each direction prior to conducting a test. This exercise is intended to minimize hysteresis effects in the sensor. Consequently, significant drift in the sensor output is experienced for up to 1.5 hrs after completion of the anti-hysteresis exercise. Figure B.3 provides a representative sensor output immediately following a full scale deflection exercise on the DSC-6 force sensor with serial number 5117. The drift rate is relatively high (1 X 10^{-4} N/min) immediately after the load is released from the force sensor. The rate then steadies to a value of 4.4 X 10^{-6} N/min after approximately 12 minutes. Drift testing of the sensor output as described above was conducted on several different force sensors. Once the previously mentioned environmental factors were eliminated, no sensor was found to drift at steady state by more than 7.0 X 10^{-6} N/min. Equivalently, the drift rate was less than 0.25% per minute of the smallest drag force measured on a single pin fin during testing.

To eliminate the detrimental environmental effects, all calibration tests were conducted inside of a wooden calibration shelter. The shelter was effective in maintaining a constant light level and also provided a mechanical damping for air currents which could have caused a swaying of the mass basket hanging from the DSC-6 force sensor. Additionally the shelter provided thermal damping of small fluctuations in the ambient air temperature.

Figure B.4 shows a schematic of the calibration setup inside the shelter. The DSC-6 force sensor was mounted to a circular Lexan plate by means of the same adjustable mount used to attach the force sensor to the test section floor plate, as shown in Figure 3, with the sensor beam protruding through a clearance hole in the Lexan plate. The force sensor and mount were also encased within the same silicone oil reservoir well in order to replicate test conditions as much as possible. The circular Lexan plate was mounted vertically to a metal frame which was suspended on a vibration isolation system. The isolation system was constructed of layers of felt and foam pads which aided in damping the ground borne vibrations present within the testing laboratory. In the same way the sensor pin fin was threaded onto the end of the force sensor an aluminum calibration beam, with multiple grooves cut around the circumference of the beam, was threaded onto the DSC-6 force sensor. A mesh basket, constructed of fish netting and nylon string, was then hung from the calibration beam in one of the grooves. In this way the effective length of the sensor cantilever beam could be varied by hanging the mesh basket in different grooves. The weight of the calibration beam (0.83 g) and the mesh basket (0.52 g) were nulled from the sensor output by re-balancing the Wheatstone Bridge via the potentiometer.

To sample d_x and ψ, masses were hung from the sensor with the x-axis aligned vertically with gravity. Conversely, d_y and ξ were obtained by aligning the sensor y-axis with gravity. Tests conducted with both axes rotated askew to gravity, or with different effective beam lengths, were used to gain confidence in the calibrated values of d_x, d_y, ξ, and ψ. Figure B.5 provides a flow chart detailing the steps used to conduct a calibration test. Note that the flowchart in Figure B.5 specifics that 360 seconds are allowed to elapse between placing the calibration mass on the sensor calibration beam and the start of data collection. Experimentally, it was found during force measurement testing that ordinarily up to 360 seconds were required to allow the force sensor output to come to a steady state. Again this dwell time was duplicated in calibration testing for the sole purpose of replicating testing conditions.

The DSC-6 force sensor was calibrated by hanging ANSI/ASTM E617 Class 6 masses from the sensor calibration beam. The masses were selected and applied per the guidelines of ASTM E74. Table B.2 provides the sequence of 17 masses that were applied to the DSC-6 force sensor in ascending order during one calibration test. ASTM E74 recommends calibration by ascending mass application only if the sensor is to measure forces that are applied in a similar manner. In actual force measurement testing this was the case because the pin fin force

increased as the blower accelerated to the steady state frequency. Calibration tests were conduced at least twice. Figure B.6 provides a flowchart for the data reduction methodology used in calculating d_x, while Figure B.7 depicts the methodology for calculating ψ. The calculation of d_y and ξ can be determined similar to d_x and ψ by switching the x and y variables in Figures B.6 and B.7. The sensor proportionality constant for a given axis was obtained by performing a linear regression of that axis' sensor output with respect to the applied masses when that axis was aligned with gravity. The cross axis correction coefficient for a given axis was calculated at each mass application according to Equation 5 when the axis was aligned perpendicular to gravity. The median value of the cross axis correction coefficient was selected as the representative test value from the test sequence since the median is a better indicator of central tendency than the mean. The calculated value of the cross axis correction coefficient constant was generally skewed at the low end of the force range due to measurement resolution as mentioned earlier. These outlying values may distort the mean but the median remains unaffected.

Table B.3 summarizes the 7 calibration tests that were performed on the DSC-6 force sensor with serial number 5121. Table B.4 summarizes the values obtained for ξ and ψ from tests 4-6 and 1-3 respectively. Averaging the results from all tests, ξ was measured to be 0.0237, and ψ was measured to be 0.1309. Test 7 was performed at a 45° angle with a slightly longer beam length than was used in previous calibration tests. For this calibration test, the values of ξ and ψ obtained in tests 1-6 were used to correct for cross axis effects. Table B.5 summarizes the d_x coefficients obtained from all calibration tests. Similarly, Table B.6 lists all d_y coefficients obtained from testing. Averaging the sum of all values, d_x was calculated to be 0.1143 (V/V-kg-cm) ± 0.61% while d_y was found to be 0.1109 (V/V-kg-cm) ± 1.19%. Both values are reported at a 95% confidence level. The relatively small confidence interval for each coefficient provides assurance that calibration tests are repeatable while an R^2 value of 1.000 for each calibration tests supports the linearity of the sensor output with applied force.

Plots of relative error between the measured force and the calibration force are provided in Figures B.8 and B.9. Figure B.8 plots the absolute relative error as a function of applied force for the force sensor x-axis. Similarly, Figure B.9 plots the absolute relative error for the y-axis calibration tests as a function of applied force. Each plot shows that the relative error between the measured force and the actual force is never more than 2% for forces above the lowest

measured pin fin drag force. Also the measurement error decreases monotonically towards zero for each sensor axis as the calibration forces are increased. These results are intended to provide the reader with a sense of the quality of calibration that can be achieved with the DSC-6 force sensor when the environmental factors are properly controlled.

The ability to make accurate force measurements on a pin fin in a channel after successful calibration of a sensor hinged largely on the alignment of the sensor pin fin within the channel clearance hole. Ideally, the force sensor pin fin would be placed coaxially in the clearance hole and orthogonal to the flow direction. Figure B.10 provides a detailed schematic of the force sensor mount used to meet these requirements. The mount allowed for two degrees of translation in the plane of the channel floor as well as three degrees of rotation of the force sensor. Once properly mounted the centering of the force sensor pin fin in the channel ceiling and floor clearance holes was checked by deflecting the force sensor in the two perpendicular axis directions and checking the sensor output. In this way, the location of the force sensor pin fin could be verified.

Table B.1. Summary of Two-Axis DSC-6 Force Sensors [15].

S/N	X-Axis			Y-Axis		
	R_1 (Ω)	R_3 (Ω)	GF	R_2 (Ω)	R_4 (Ω)	GF
5117	1046	1076	6.9	1053	1046	6.6
5118	1073	1043	6.4	1070	1082	6.7
5119	1059	1065	6.6	1069	1043	6.3
5120	1057	1042	6.7	1057	1038	6.6
5121	1071	1021	6.6	1087	1055	6.7
5122	1091	1057	6.9	1086	1050	6.8
5123	1092	1075	6.3	1069	1083	6.5
5124	1099	1082	6.3	1051	1071	7.2

Table B.2. Force Sensor Calibration Mass Application Sequence [15].

Sequence	Nominal Applied Mass (g)	Nominal Applied Force (N)
1	0.05	4.90E-04
2	0.1	9.81E-04
3	0.2	1.96E-03
4	0.5	4.90E-03
5	0.7	6.86E-03
6	1	9.81E-03
7	2	1.96E-02
8	4	3.92E-02
9	5	4.90E-02
10	6	5.88E-02
11	8	7.85E-02
12	10	9.81E-02
13	12	1.18E-01
14	14	1.37E-01
15	16	1.57E-01
16	18	1.77E-01
17	20	1.96E-01

Table B.3. Summary of Calibration Tests Performed on Sensor 5121.

Index	Angle from Vertical (°)		Effective Beam Length (cm)	Notes / Objectives
	x	y		
1	0	90	2.76	Sample d_x and ψ
2	0	90	2.76	Sample d_x and ψ
3	0	90	2.76	Sample d_y and ψ
4	90	0	2.76	Sample d_y and ξ
5	90	0	2.76	Sample d_y and ξ
6	90	0	2.76	Sample d_y and ξ
7	45	45	3.22	Sample d_x and d_y with known ξ and ψ

Table B.4. Summary of ξ and ψ Results for Sensor 5121.

ξ				ψ		
Index	**ξ_{median}**	**$\%\triangle\xi_{avg}$**		**Index**	**ψ_{median}**	**$\%\triangle\psi_{avg}$**
4	0.0228	-3.81%		1	0.1298	-0.83%
5	0.0226	-4.61%		2	0.1306	-0.19%
6	0.0257	8.42%		3	0.1322	1.02%
ξ_{avg}:	**0.0237**			**ψ_{avg}:**	**0.1309**	

Table B.5. Summary of d_x Results for Sensor 5121.

Index	Angle from Vertical (°)	Beam Length (cm)	d_x (V/V-kg-cm)	$\%\triangle d_{x,avg}$	R^2
1	0	2.76	0.1146	0.28%	1.000
2	0	2.76	0.1143	0.00%	1.000
3	0	2.76	0.1146	0.26%	1.000
7	45	3.22	0.1136	-0.54%	1.000
		$d_{x,avg}$ (V/V-kg-cm)	**0.1143**		
		95 % Confidence Interval (±%)	**0.61%**		

Table B.6. Summary of d_y Results for Sensor 5121.

Index	Angle from Vertical (°)	Beam Length (cm)	d_y (V/V-kg-cm)	$\%\Delta d_{y,avg}$	R^2
4	0	2.76	0.1114	0.49%	1.000
5	0	2.76	0.1112	0.31%	1.000
6	0	2.76	0.1112	0.32%	1.000
7	45	3.22	0.1096	-1.12%	1.000
		$d_{y,avg}$ (V/V-kg-cm)	**0.1109**		
		95 % Confidence Interval (±%)	**1.19%**		

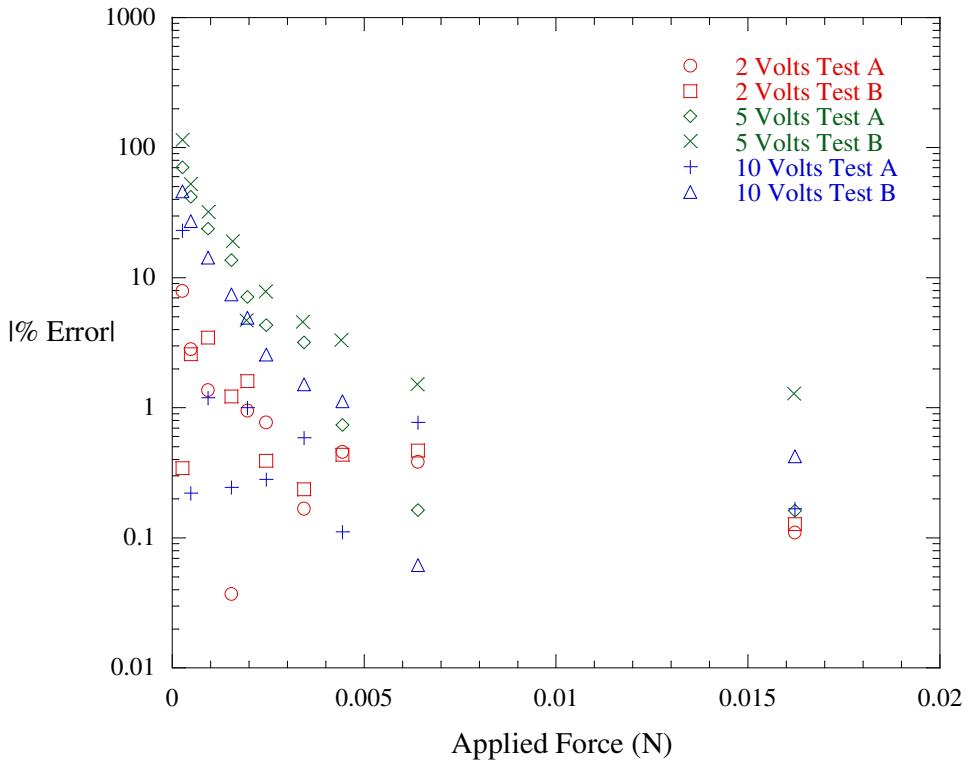

Figure B.1. The scatter plot summarizes the results of a one axis DSC-6 force sensor calibration test with a variety of excitation voltages [15].

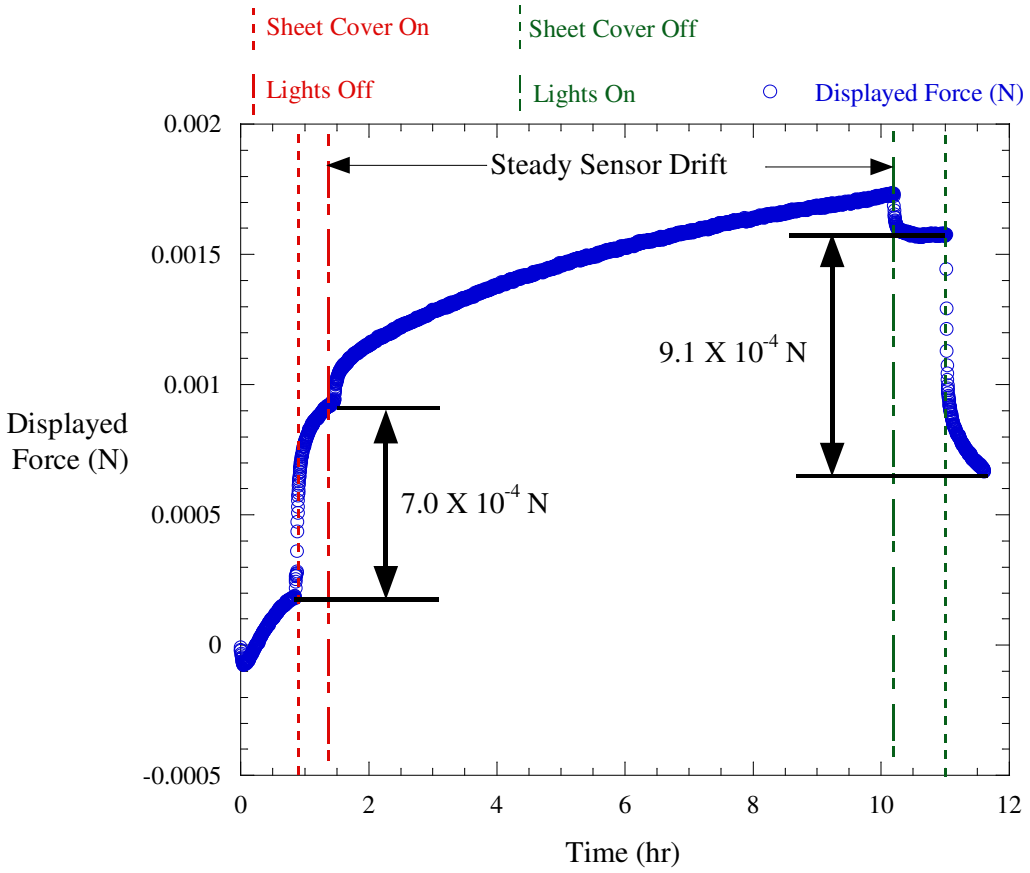

Figure B.2. Sensor output from an overnight drift test. The figure shows the effect of changing light intensity on the sensor output [15].

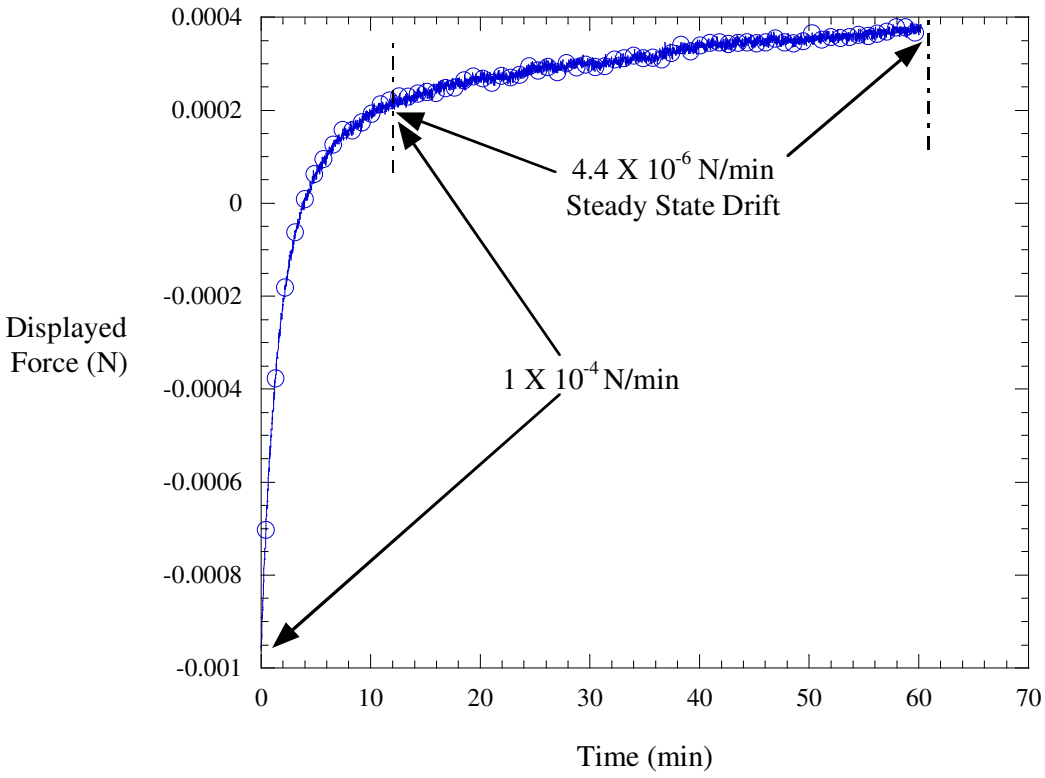

Figure B.3. Plot illustrating increased sensor drift rates after exercising the sensor to full scale [15].

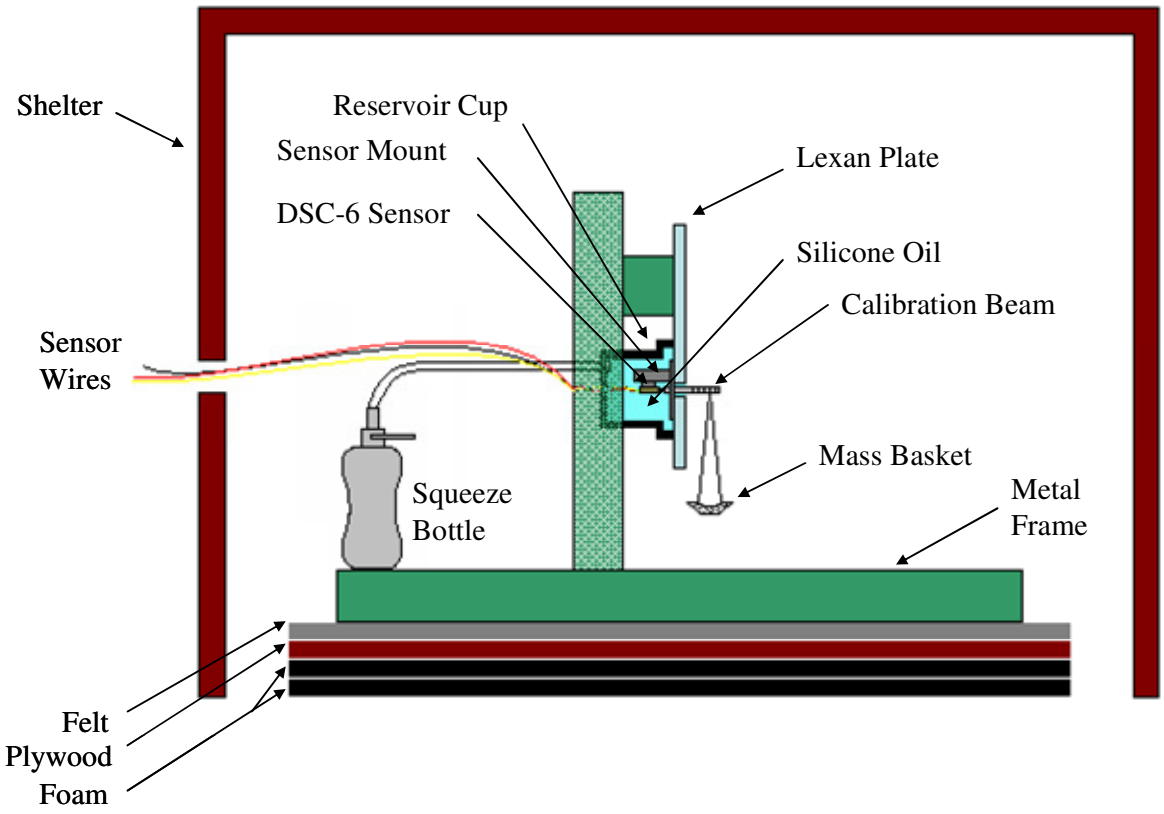

Figure B.4. Schematic of the setup used to perform calibration tests on the DSC-6 force sensors.

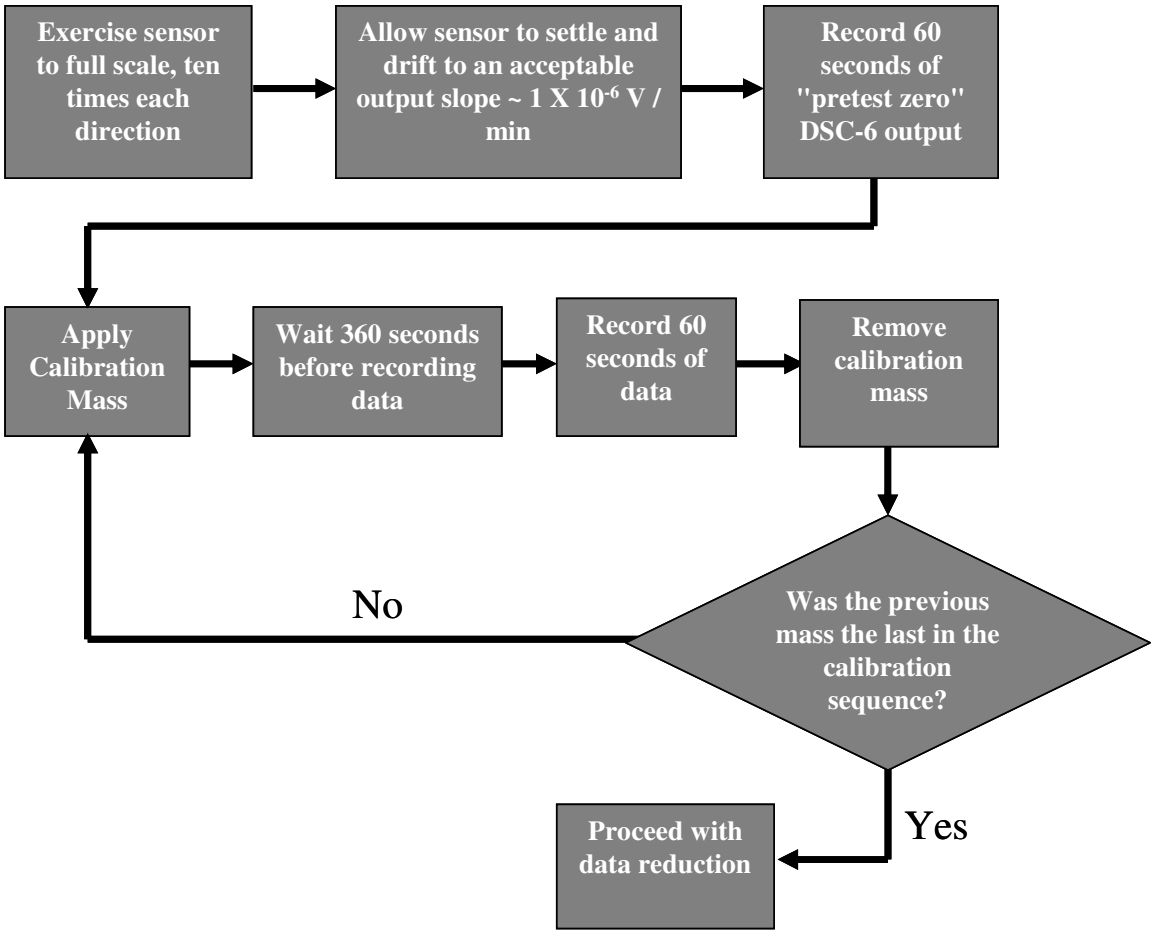

Figure B.5. Flowchart describing the execution of a calibration test [15].

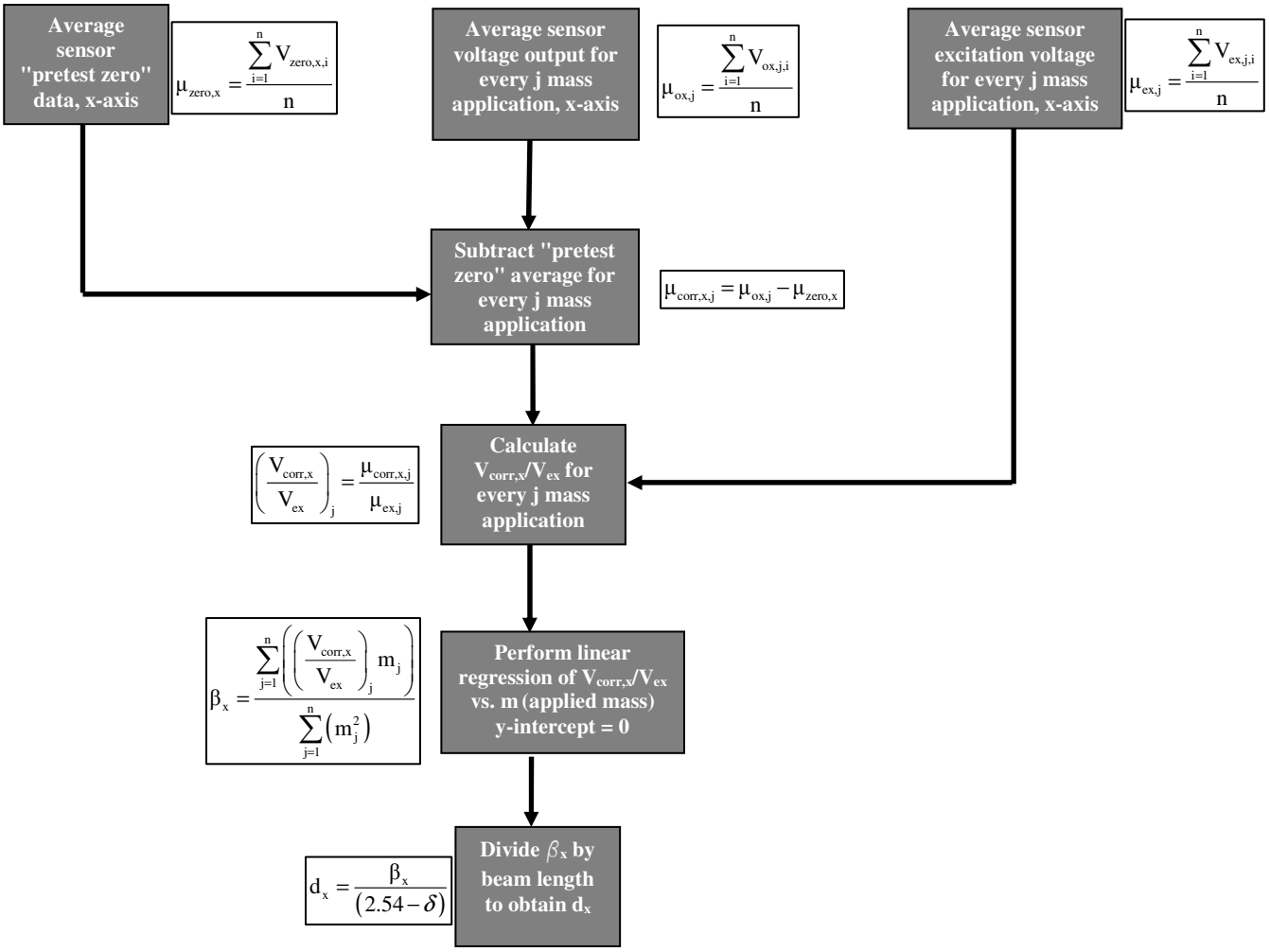

Figure B.6. Flowchart describing the calibration data reduction methodology for d_x [15].

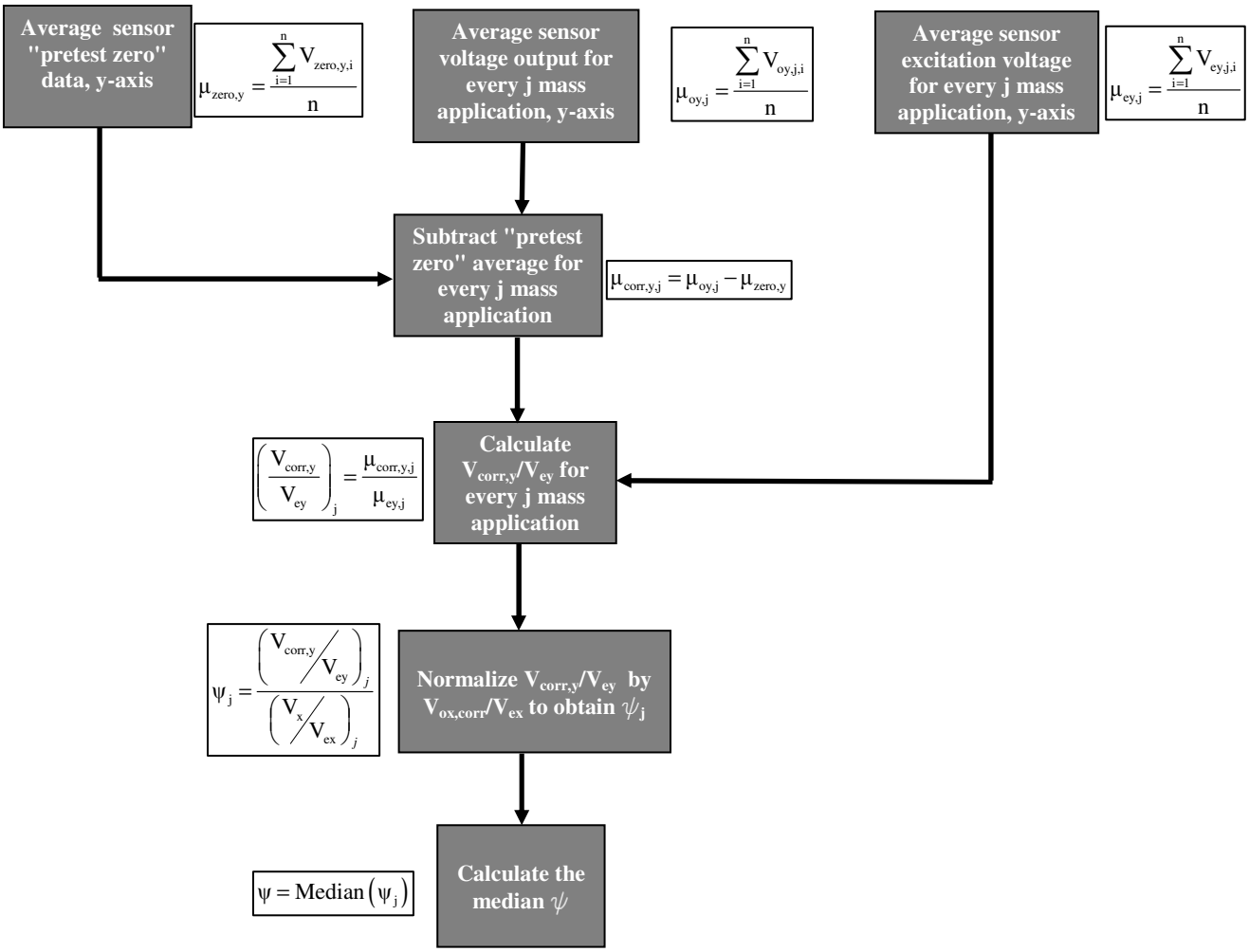

Figure B.7. Flowchart describing the calibration data reduction methodology for ψ [15].

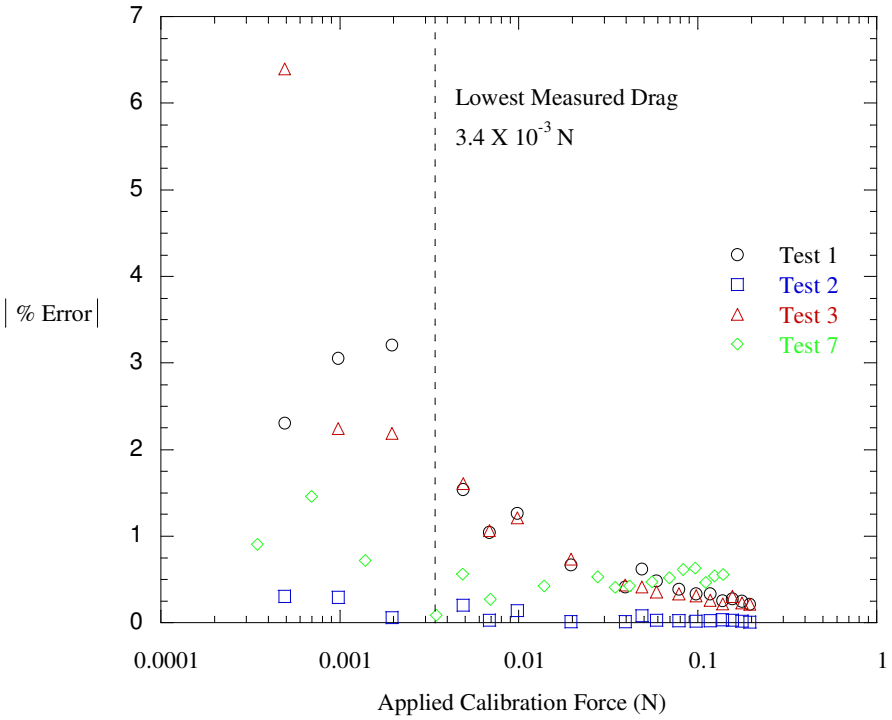

Figure B.8. Summary of the relative error between the x-axis sensor output and the applied calibration force.

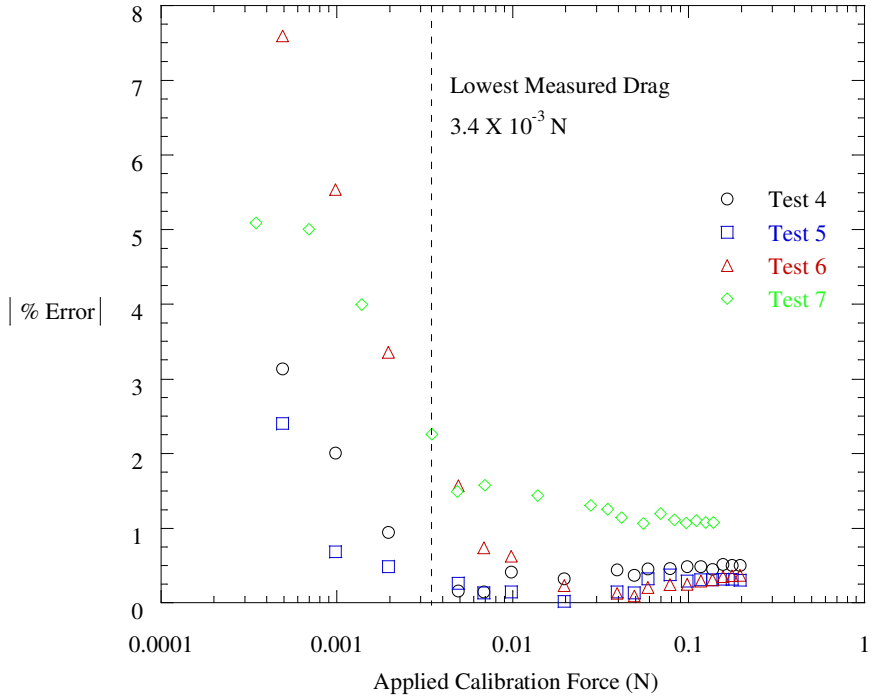

Figure B.9. Summary of the relative error between the y-axis sensor output and the applied calibration force.

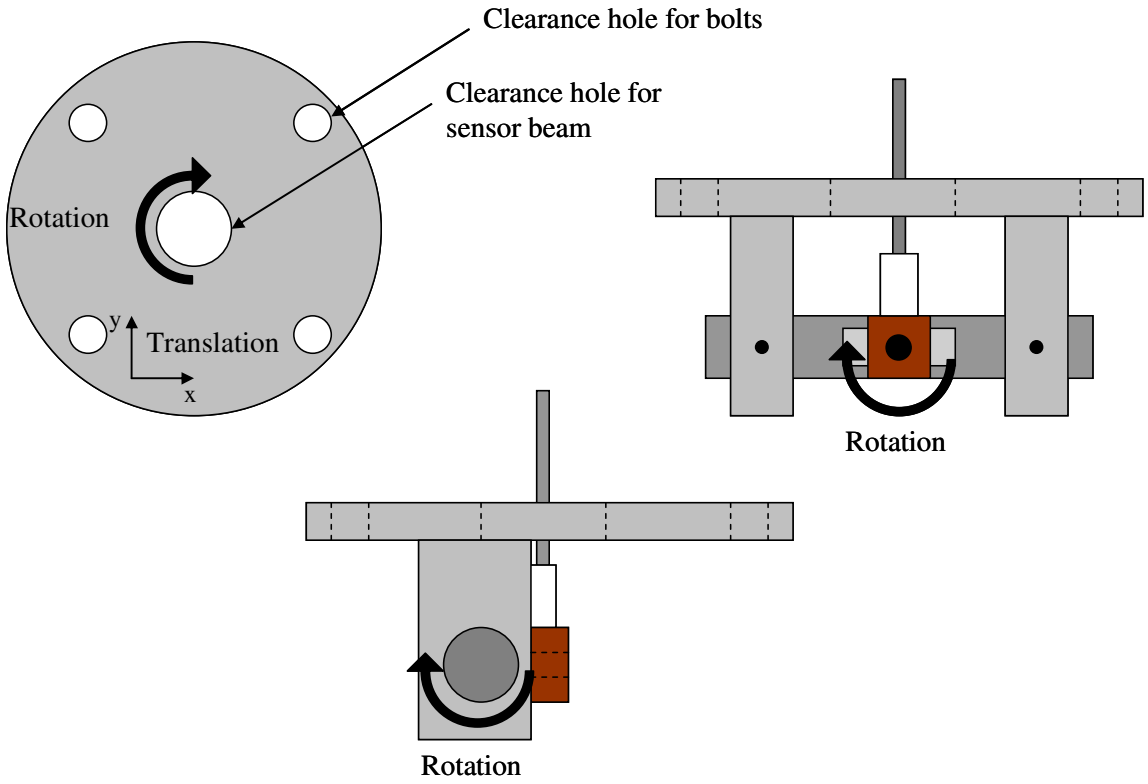

Figure B.10. Schematic of the force sensor mounting bracket.

Appendix C: Force Testing Methodology and Data Reduction

While the extension piece was detached the, first step before conducting a force test was the inspection of the silicone oil in both the top and bottom reservoirs. It was important that there be no air bubbles in either reservoir. Bubbles rising through the silicone oil applied a dynamic force to the sensor pin fin that could be observed in the sensor output during testing. Additionally, static bubbles in contact with the sensor pin fin presented a bias error due to the imbalance of the hydro-static pressure around the pin fin. This particular phenomenon usually occurred in the floor silicone reservoir when the silicone oil level, due to leakage into the test channel, became low enough for the silicone oil to be depressed down from the floor clearance gap by the stagnation pressure on the front of the sensor pin fin causing an air bubble to form against the sensor pin fin at the inner ceiling of the channel floor counterbore.

The effect of a static bubble in the floor silicone reservoir during a flow test can be seen in Figure C.1. Figure C.1 plots the DSC-6 sensor output for a Re = 18,000 flow, specifically for a single row of pin fins with a S1/d = 12. Approximately 135 seconds into the test, a large air bubble expanded into the clearance gap between the clearance hole and the sensor pin fin and down into the floor counterbore at the front of the pin fin, evident by the sudden change in sensor output in Figure C.1. The drag force decreased by approximately 2.5×10^{-3} N, while the lift force increased by approximately 5.0×10^{-4} N. In every instance of this occurrence, a bubble at the front of the sensor pin fin was found to decrease the drag force measurement, while a bubble at the rear of the sensor pin fin increased the drag force measurement. This effect is expected due to the imbalance in hydro-static pressure with the formation of an air bubble against the sensor pin fin. The bubble serves to alleviate the hydro-static pressure force of the silicone oil on one side of the sensor pin fin, correspondingly, the measured drag force is increased in the opposing direction. Similarly, the lift force is also affected by which side of the sensor pin fin the air bubble is positioned to.

Static bubbles in the floor silicone reservoir were removed by squeezing excess silicone oil from the plastic squeeze bottle into the reservoir. Unfortunately, this process invariably resulted in excess silicone oil leakage into the test channel through the gap between the floor clearance hole and the sensor pin fin. Due to capillary forces, which tended to draw the silicone oil up from the bottom reservoir into the channel, several hours were often required for the

silicone oil level within the clearance gap to reach equilibrium with the level of the channel floor. During this time the silicone oil was wiped away from the sensor pin fin and removed from the test channel using paper cloth attached to a small circular rod, which was small enough fit into the channel. Unlike the floor silicone reservoir, silicone leakage from the ceiling silicone reservoir was usually insignificant as the addition of a hydro-static force, due to the height of the silicone in the ceiling reservoir, was effective in balancing out the interactions between the capillary and gravitational forces leaving the silicone oil level in the ceiling clearance gap in equilibrium with the level of the channel ceiling.

It was very important that the silicone oil not continue to leak into the channel and around the sensor pin fin during a force test as the measurements would be affected. The airflow inherently shears some silicone oil from the clearance gaps, but if there was additionally leakage then enough silicone oil would be present to affect the flow field around the sensor pin fin, therefore altering the measured drag force. The characteristic shape of the sheared silicone oil depended on the Reynolds number of the flow and exhibited a very interesting pattern, indicative of the strong vortex shedding from the backside of the pin fin. At Reynolds number flows less than Re = 10,000 the silicone oil simply formed a fillet around the backside of the pin fin, as shown in Figure C.2 for a single row of pin fins with an S1/d = 2. Figure C.3 shows how the silicone oil was swept from around the sensor pin fin by the airflow where it was collected into a small puddle at the backside of the pin fin and then drawn upwards to form a single bulb like shape for a Re = 12,000 flow. With increasing Reynolds number the bulb began to split into two separate bulbs as shown in Figure C.4 for a Re = 15,000 flow. Eventually the two silicone oil bulbs completely separated and formed two distinct silicone oil mounds on the back side of the sensor pin fin as shown in Figure C.5 for a Re = 18,000 flow. At Reynolds number flows above approximately Re = 20,000 the silicone oil mounds were unable to hold a distinct shape and instead were twisted and ripped away by the vortices shedding from the trailing edge of the sensor pin fin as shown in Figure C.6.

In any case, the effect of the excess silicone oil on the backside of the sensor pin fin was to create a more airfoil shape, retarding the separation point on the pin fin and reducing the drag force. Figure C.7 shows how the excess silicone oil affected the sensor output for a single row of pin fins with an S1/d = 12 at a flow of Re = 35,000. The silicone bulb began to form at approximately 100 seconds into the test and initiation of the flow. As the bulb grew in size, the

measured drag decreased while the lift force stayed relatively constant. The bulb continued to grow until approximately 500 seconds, when the bulb began to break up and oscillate before it was sheared away. Note that the oscillation of the silicone bulb affected both the drag and lift force measurements.

While it was important that there not be an excess amount of silicone oil within the test channel and around the sensor pin fin it was also essential that the silicone oil level not be to low within the clearance gap between the sensor pin fin and the clearance hole. As mentioned previously, this can result in the formation of an air bubble during a test, usually occurring at the front side of the pin fin due to the stagnation pressure present there. Regardless if an air bubbles formed, a low silicone oil level still proved to be detrimental to the measured drag forces. In most cases it was observed that the sensor output would not reach a steady state over the 15 minute testing period, instead the sensor drag output would continually rise over the duration of the test.

From the above discussion, it should apparent that the condition of the silicone oil in each reservoir is extremely important to the validity of the force measurements. Once the silicone oil reached this steady state and all excess silicone was removed from around the sensor pin fin, the extension piece was reattached to connect the test section back to the flow measurement section. Dark cloth sheets were then placed over the test section to provide additional shielding from the ambient lighting, as small disturbances in the light intensity tended to cause jumps in the sensor output, as discussed previously. The sensor was then allowed to reach an acceptable drift rate before turning the blower on to the required frequency corresponding to the desired Reynolds number flow. Figure C.8 provides a flow chart detailing the execution of a force measurement test. After recording 15 minutes of data from the force sensor, the blower was turned off. At the conclusion of the test the test channel was inspected to examine the condition of the silicone oil within each reservoir and the amount of silicone that may have leaked into the channel around the sensor pin fin. Tests that showed excessive silicone oil in the test channel, or a bubble in the reservoirs, were discarded.

Once a test was completed where the sensor output reached a steady state value and the condition of the silicone oil was acceptable the recorded raw voltages from the force sensor were reduced to provide drag and lift coefficients. The drag and lift force were calculated according to Equation 3 after applying the cross axis corrections defined by Equation 4. In order to obtain

the drag and lift coefficients the forces were normalized by the product of the dynamic pressure head, based on the velocity through the open flow area, and the projected frontal area of the sensor pin fin. The volume flow rate of the flow was calculated from the pressure drop measurements made across the flow measurement device during testing. The volume flow rate, along with the average temperature of the channel flow, was used to calculate the Reynolds number of the flow. Figure C.9 provides a flow chart for the data reduction methodology of the drag force component and the corresponding Reynolds numbers. Here again, the lift coefficient can be found by simply substituting y for x, and ψ for ξ in Figure C.9.

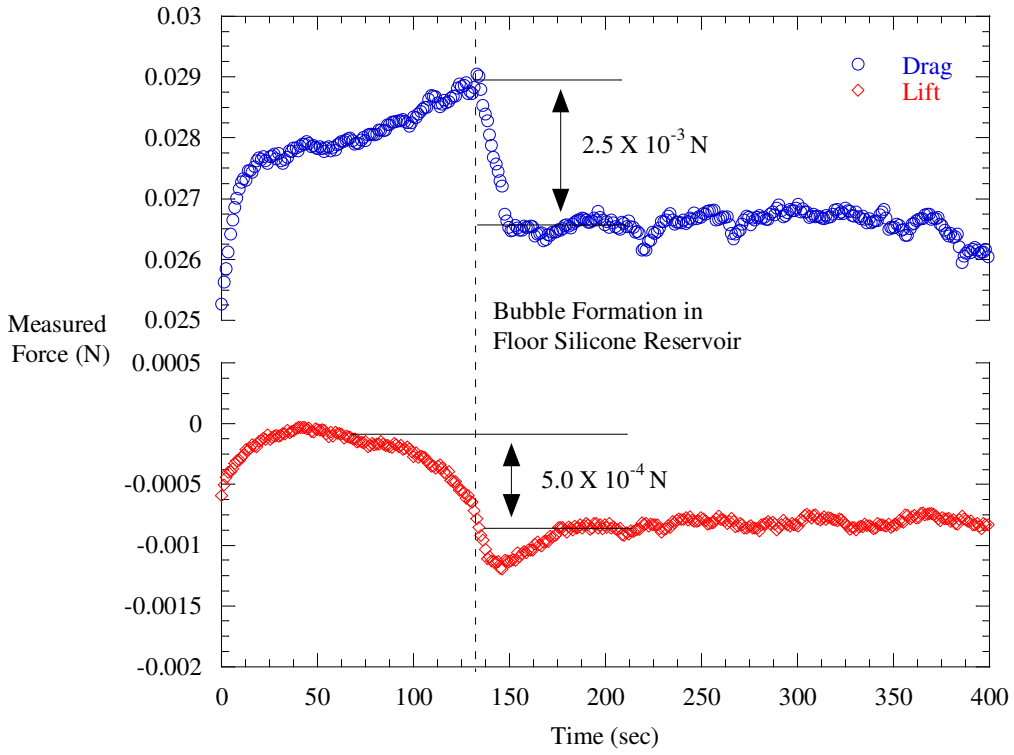

Figure C.1. Plot of the sensor output showing the effect of a static air bubble in the floor silicone reservoir at the leading edge of the sensor pin fin [15].

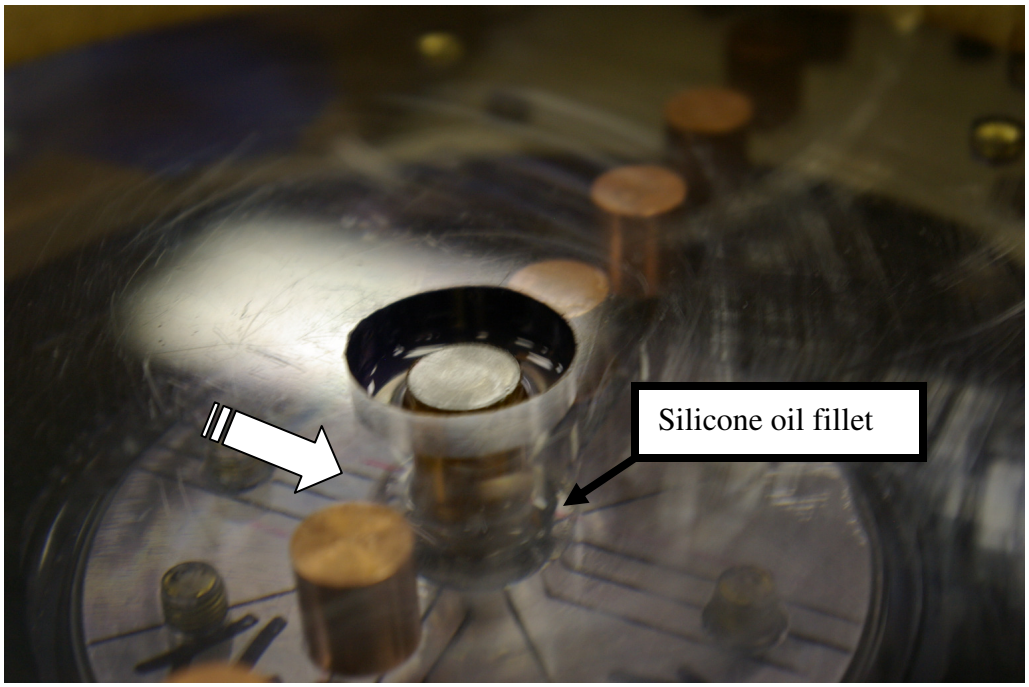

Figure C.2. Annotated photograph showing the formation of a small silicone oil fillet on the trailing edge of the sensor pin fin.

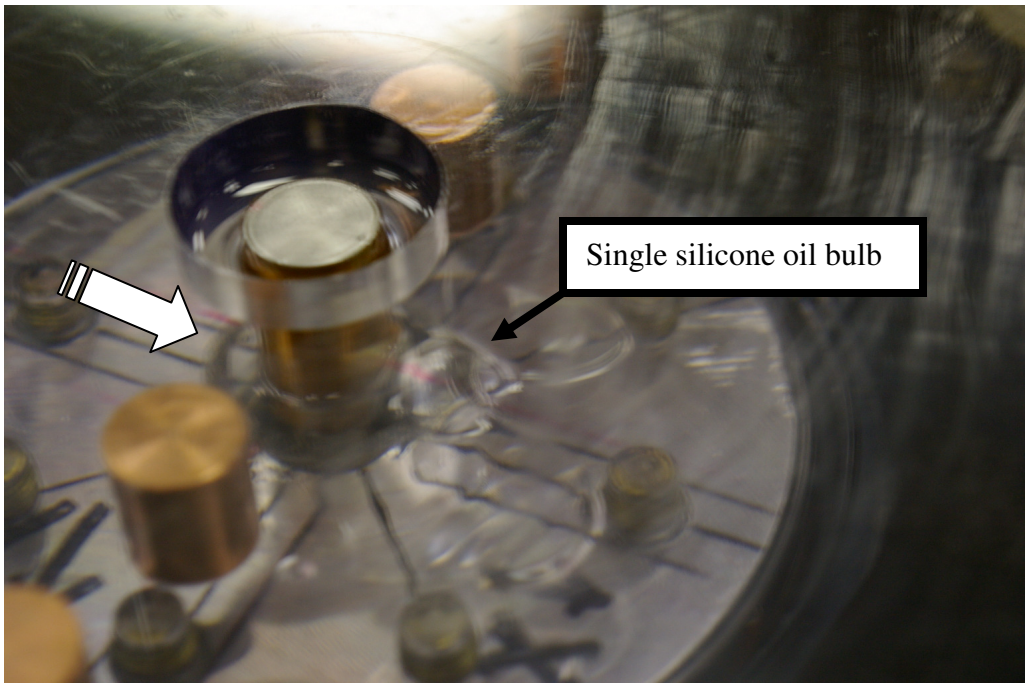

Figure C.3. Annotated photograph showing the formation of a single silicone oil bulb on the trailing edge of the sensor pin fin.

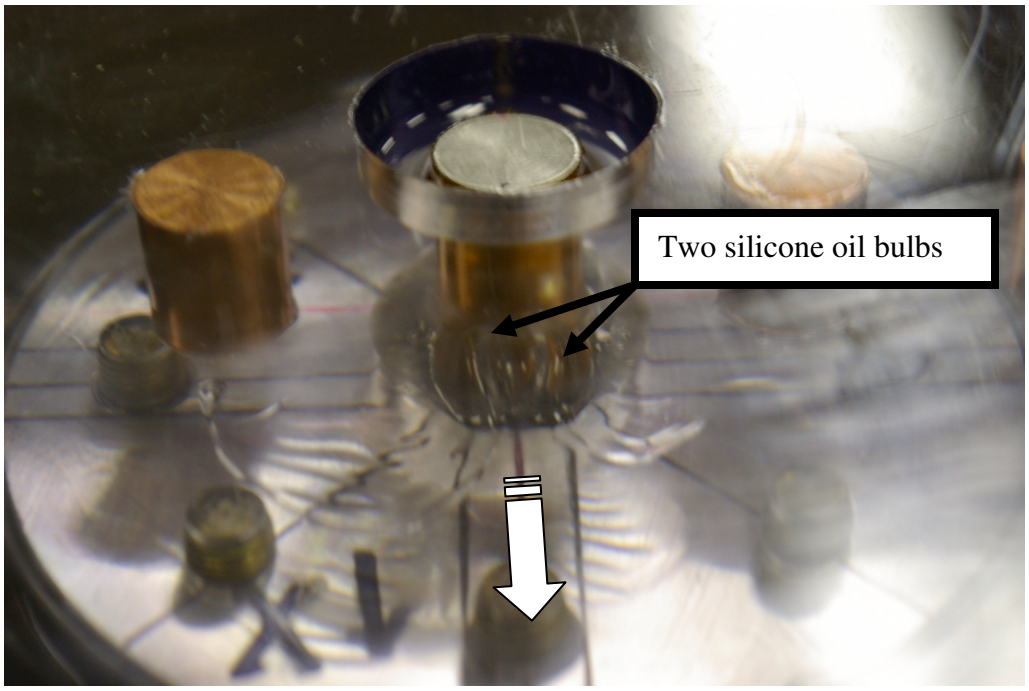

Figure C.4. Annotated photograph showing two separate silicone oil bulbs formed from the split of a single silicone oil bulb on the trailing edge of the sensor pin fin.

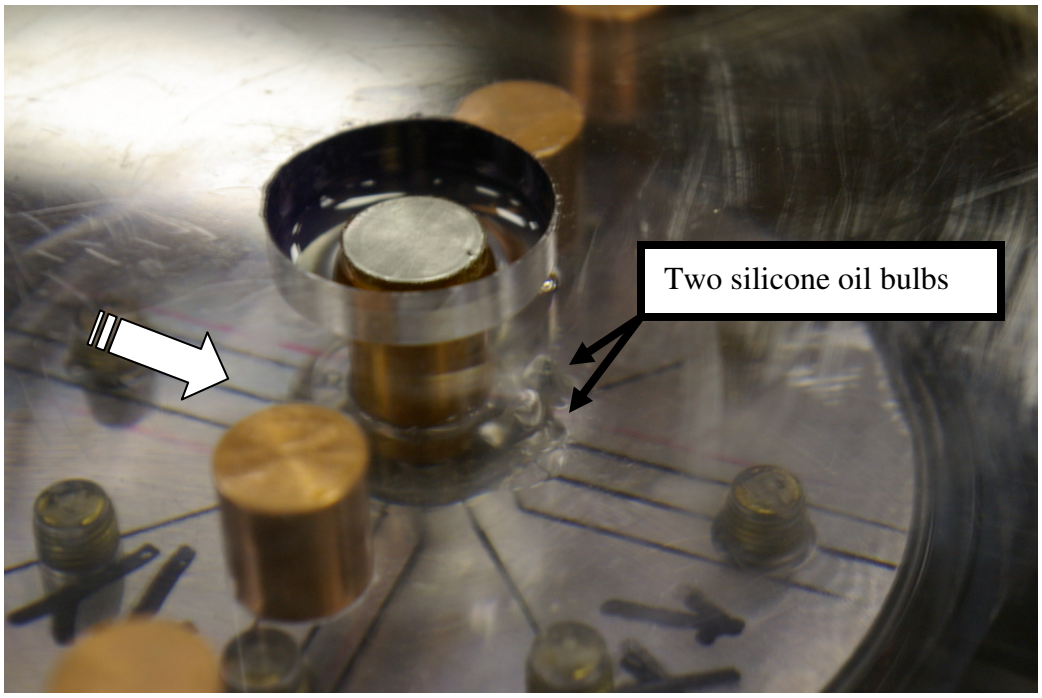

Figure C.5. Annotated photograph showing two distinctly separate silicone oil bulbs on the trailing edge of the sensor pin fin.

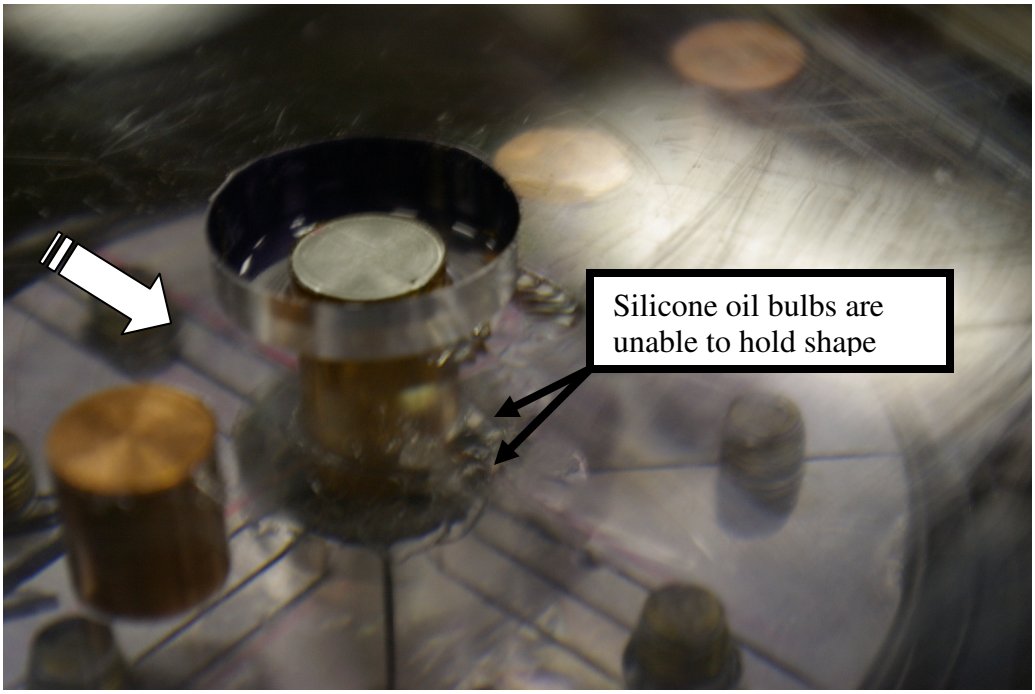

Figure C.6. Annotated photograph showing the collapse and separation of the two separate silicone oil bulbs on the trailing edge of the sensor pin fin.

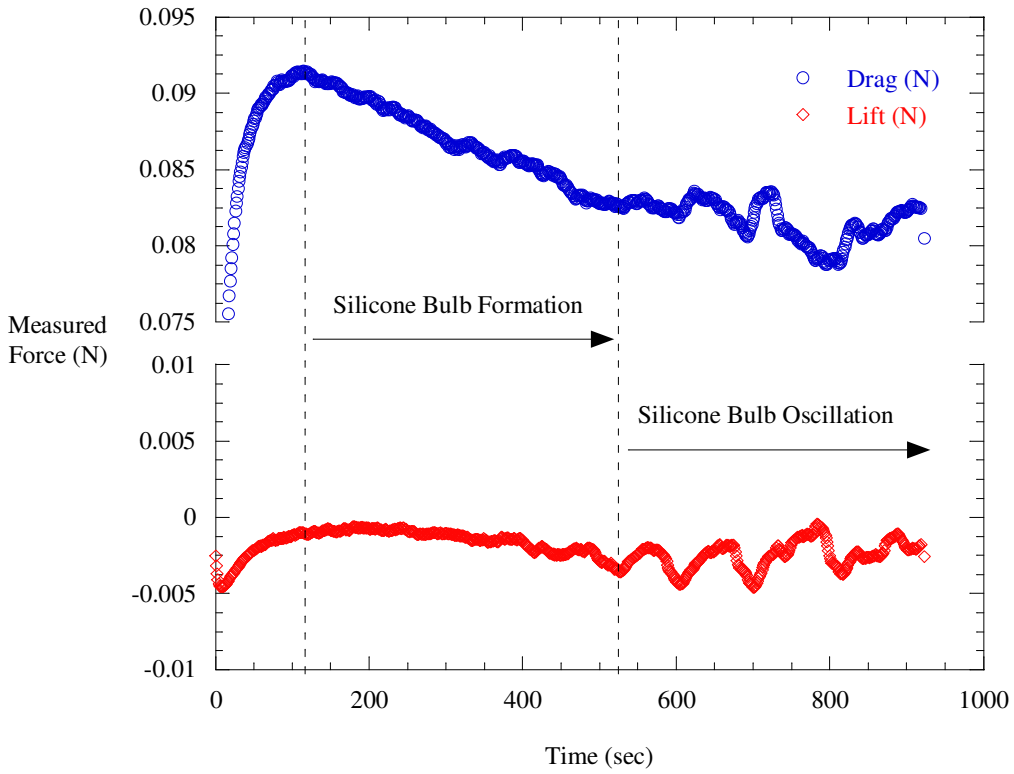

Figure C.7. Plot of the sensor output showing the effect of silicone oil leakage and collection on the trailing edge of the sensor pin fin [15].

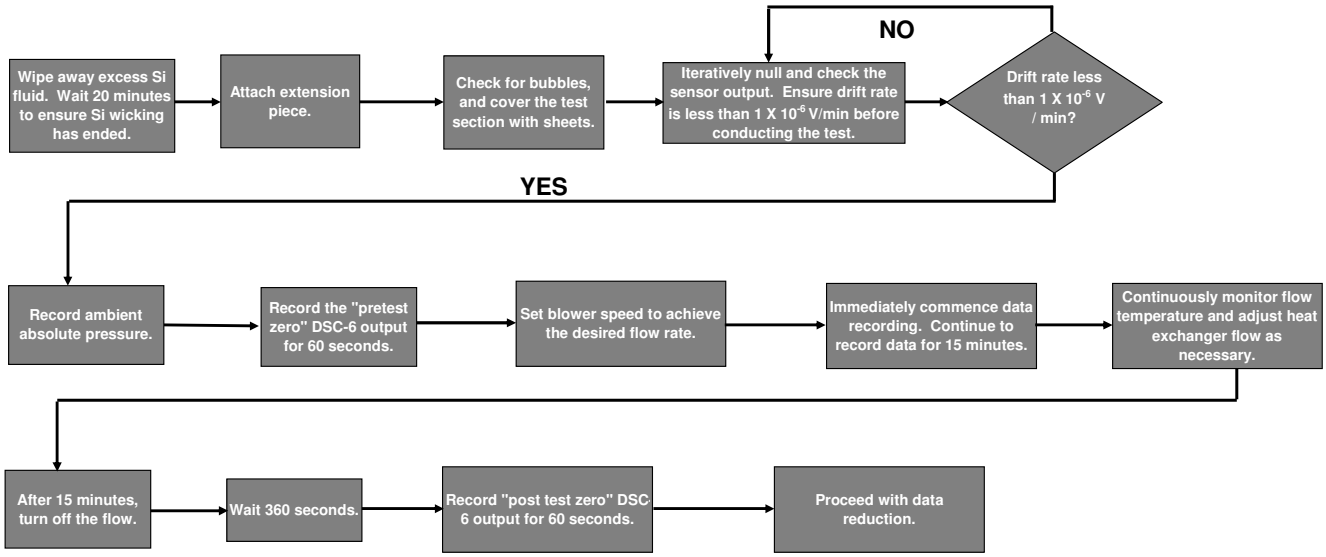

Figure C.8. Flow chart detailing the execution of a force measurement test [15].

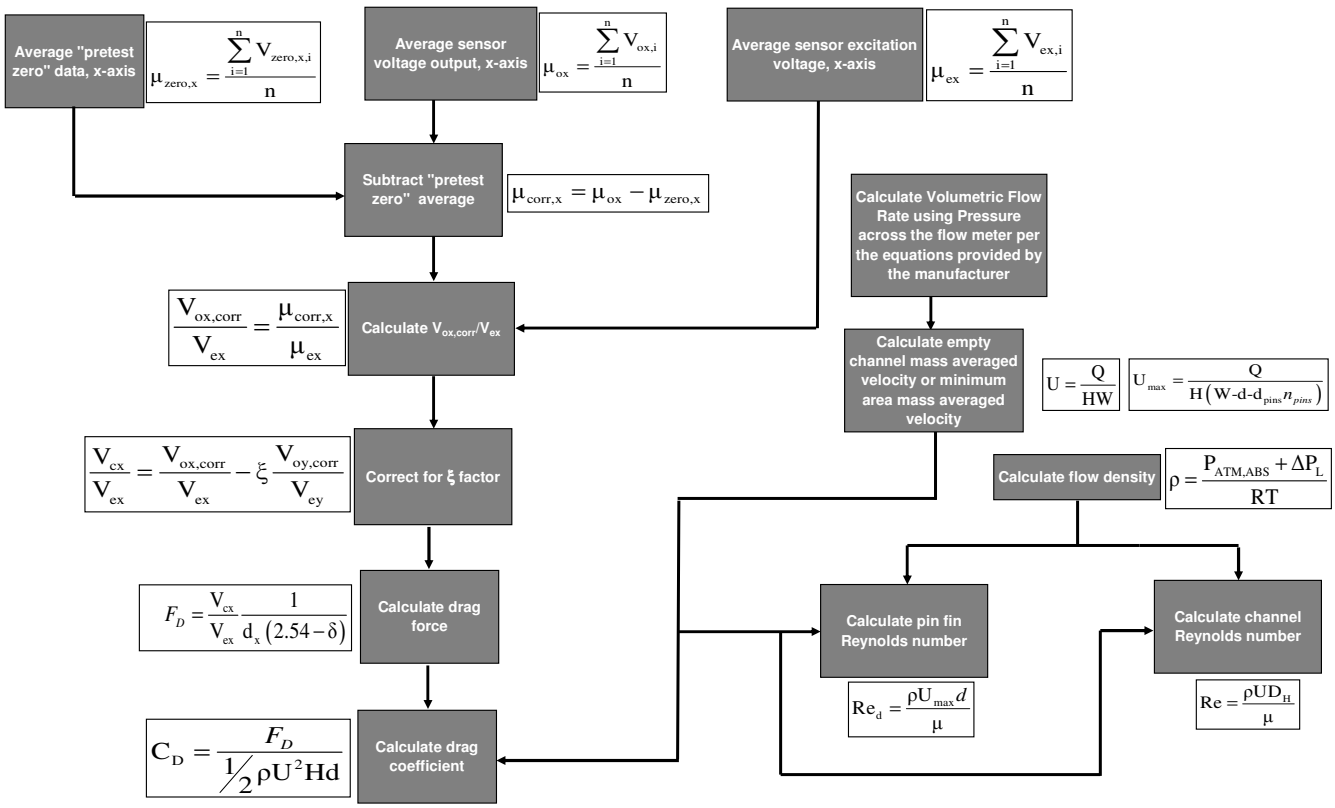

Figure C.9. Flow chart detailing the drag coefficient data reduction methodology [15].

Appendix D: Experimental Uncertainty Calculations

Uncertainty for Drag Coefficient, C_D

$$C_D = \frac{2*g*H*W^2*V_{cx}/V_{ex}}{d_x*d*Q^2*(2.54-\delta)\rho}$$

$$u_{CD} = \sqrt{\left(\frac{\partial C_D}{\partial\left(\frac{V_{cx}}{V_{ex}}\right)}u_{V_{cx}/V_{ex}}\right)^2 + \left(\frac{\partial C_D}{\partial(d_x)}u_{d_x}\right)^2 + \left(\frac{\partial C_D}{\partial(\delta)}u_{\delta}\right)^2 + \left(\frac{\partial C_D}{\partial(W)}u_W\right)^2 + \left(\frac{\partial C_D}{\partial(H)}u_H\right)^2 + \left(\frac{\partial C_D}{\partial(\rho)}u_{\rho}\right)^2 + \ldots}$$
$$\sqrt{\ldots + \left(\frac{\partial C_D}{\partial(Q)}u_Q\right)^2 + \left(\frac{\partial C_D}{\partial(d)}u_d\right)^2 + u_{Rotation}^2 + u_{Perpendicularity}^2 + u_{Linear,\mathrm{Re}gression}^2 + u_{Temperature}^2 + u_{Drift}^2}$$

Volumetric Flow Rate

$$Q = \left(\frac{\rho_{STD}}{\rho}\right)\frac{5.9816*(D^2)*K*Y\sqrt{dp}*\sqrt{\frac{2.703*P_L}{460+T_L}}}{\frac{2.703*14.7}{460+60}} * \frac{4.71936*10^{-4}\mathrm{m^3/sec}}{1\,\mathrm{CFM}}$$

$$u_Q = \sqrt{\left[\frac{\partial Q}{\partial(dp)}*u_{dp}\right]^2 + \left[\frac{\partial Q}{\partial(T_L)}*u_{TL}\right]^2 + \left[\frac{\partial Q}{\partial(P_L)}*u_{PL}\right]^2 + u_{meter}^2}$$

Sensor Voltage Ratio

$$\frac{V_{cx}}{V_{ex}} = \frac{(V_{ox}-V_{zero,x})}{V_{ex}} - \xi\frac{(V_{oy}-V_{zero,y})}{V_{ey}}$$

$$u_{\frac{V_{cx}}{V_{ex}}} = \sqrt{\left[\frac{\partial\left(\frac{V_{cx}}{V_{ex}}\right)}{\partial(V_{ox})}*u_{V_{ox}}\right]^2 + \left[\frac{\partial\left(\frac{V_{cx}}{V_{ex}}\right)}{\partial(V_{ex})}*u_{V_{ex}}\right]^2 + \left[\frac{\partial\left(\frac{V_{cx}}{V_{ex}}\right)}{\partial(V_{zero,x})}*u_{V_{zero,x}}\right]^2 + \left[\frac{\partial\left(\frac{V_{cx}}{V_{ex}}\right)}{\partial(\xi)}*u_{\xi}\right]^2 + \ldots}$$
$$\sqrt{\left[\frac{\partial\left(\frac{V_{cx}}{V_{ex}}\right)}{\partial(V_{oy})}*u_{V_{oy}}\right]^2 + \left[\frac{\partial\left(\frac{V_{cx}}{V_{ex}}\right)}{\partial(V_{ey})}*u_{V_{ey}}\right]^2 + \left[\frac{\partial\left(\frac{V_{cx}}{V_{ex}}\right)}{\partial(V_{zero,y})}*u_{V_{zero,y}}\right]^2}$$

Table D.1. Experimental Uncertainty Contributions to the Drag Coefficient for a Single Row Array with S1/d = 2 at the Low Reynolds number.

Variable	Value	Precision Uncertainty	Bias Uncertainty	Total Uncertainty	u_{CD}	% C_D
C_D	4.04	0.064	0.146	0.160	**0.160**	**3.95%**
V_{cx}/V_{ex}	2.85E-04	5.142E-07	0	5.14E-07	7.29E-03	0.18%
d_x (V/V-kg-cm)	0.11	0	1.16E-03	1.16E-03	4.09E-02	1.01%
δ (cm)	-0.19	0	1.27E-02	1.27E-02	1.88E-02	0.47%
W (m)	0.61	0	7.94E-04	7.94E-04	1.05E-02	0.26%
H (m)	9.60E-03	0	2.54E-04	2.54E-04	1.07E-01	2.65%
ρ (kg/m^3)	1.11	2.59E-05	1.42E-03	1.42E-03	5.17E-03	0.13%
Q (m^3/s)	0.038	1.25E-05	3.70E-04	3.70E-04	7.84E-02	1.94%
d (m)	0.010	0	5.08E-05	5.08E-05	2.11E-02	0.52%
Rotation (°)	0	0	5	5	1.54E-02	0.38%
Perpendicularity (°)	0	0	5	5	1.54E-02	0.38%
Linear Regression Uncertainty	N/A	6.38E-02	0	6.38E-02	6.38E-02	1.58%
Temperature Uncertainty (g)	N/A	0	3.30E-03	3.30E-03	1.46E-02	0.36%
Sensor Drift (g)	N/A	0	5.02E-03	5.02E-03	2.22E-02	0.55%

Table D.2. Experimental Uncertainty Contributions to the Drag Coefficient for a Single Row Array with S1/d = 2 at the High Reynolds number.

Variable	Value	Precision Uncertainty	Bias Uncertainty	Total Uncertainty	u_{CD}	% C_D
C_D	4.03	0.005	0.142	0.142	**0.142**	**3.51%**
V_{cx}/V_{ex}	5.30E-03	3.133E-06	0	3.13E-06	2.38E-03	0.06%
d_x (V/V-kg-cm)	0.11	0	1.16E-03	1.16E-03	4.08E-02	1.01%
δ (cm)	-0.19	0	1.27E-02	1.27E-02	1.88E-02	0.47%
W (m)	0.61	0	7.94E-04	7.94E-04	1.05E-02	0.26%
H (m)	9.60E-03	0	2.54E-04	2.54E-04	1.07E-01	2.65%
ρ (kg/m^3)	1.11	8.92E-05	1.42E-03	1.42E-03	5.14E-03	0.13%
Q (m^3/s)	0.165	3.74E-05	1.51E-03	1.51E-03	7.40E-02	1.84%
d (m)	0.010	0	5.08E-05	5.08E-05	2.10E-02	0.52%
Rotation (°)	0	0	5	5	1.53E-02	0.38%
Perpendicularity (°)	0	0	5	5	1.53E-02	0.38%
Linear Regression Uncertainty	N/A	3.72E-03	0	3.72E-03	3.72E-03	0.09%
Temperature Uncertainty (g)	N/A	0	4.46E-02	4.46E-02	1.06E-02	0.26%
Sensor Drift (g)	N/A	0	1.08E-03	1.08E-03	2.55E-04	0.01%

Table D.3. Experimental Uncertainty Contributions to the Drag Coefficient for a Seven Row Array with S1/d = 4 and S2/d = 3.46 at the Low Reynolds number.

Variable	Value	Precision Uncertainty	Bias Uncertainty	Total Uncertainty	u_{CD}	% C_D
C_D	2.16	0.041	0.260	0.264	**0.264**	**12.20%**
V_{cx}/V_{ex}	2.38E-04	4.106E-07	0	4.11E-07	3.73E-03	0.17%
d_x (V/V-kg-cm)	0.11	0	1.16E-03	1.16E-03	2.18E-02	1.01%
δ (cm)	-0.19	0	1.27E-02	1.27E-02	1.01E-02	0.47%
W (m)	0.61	0	7.94E-04	7.94E-04	5.62E-03	0.26%
H (m)	9.60E-03	0	2.54E-04	2.54E-04	5.71E-02	2.65%
ρ (kg/m³)	1.10	3.63E-05	1.40E-03	1.40E-03	2.74E-03	0.13%
Q (m³/s)	0.048	2.39E-05	2.80E-03	2.80E-03	2.52E-01	11.68%
d (m)	0.010	0	5.08E-05	5.08E-05	1.12E-02	0.52%
Rotation (°)	0	0	5	5	8.22E-03	0.38%
Perpendicularity (°)	0	0	5	5	8.22E-03	0.38%
Linear Regression Uncertainty	N/A	4.08E-02	0	4.08E-02	4.08E-02	1.89%
Temperature Uncertainty (g)	N/A	0	8.68E-04	8.68E-04	2.46E-03	0.11%
Sensor Drift (g)	N/A	0	1.08E-03	1.08E-03	3.05E-03	0.14%

Table D.4. Experimental Uncertainty Contributions to the Drag Coefficient for a Seven Row Array with S1/d = 4 and S2/d = 3.46 at the High Reynolds number.

Variable	Value	Precision Uncertainty	Bias Uncertainty	Total Uncertainty	u_{CD}	% C_D
C_D	1.79	0.008	0.063	0.064	**0.064**	**3.55%**
V_{cx}/V_{ex}	2.37E-03	9.216E-06	0	9.22E-06	6.97E-03	0.39%
d_x (V/V-kg-cm)	0.11	0	1.16E-03	1.16E-03	1.81E-02	1.01%
δ (cm)	-0.19	0	1.27E-02	1.27E-02	8.34E-03	0.47%
W (m)	0.61	0	7.94E-04	7.94E-04	4.67E-03	0.26%
H (m)	9.60E-03	0	2.54E-04	2.54E-04	4.74E-02	2.65%
ρ (kg/m³)	1.09	4.61E-05	1.39E-03	1.39E-03	2.29E-03	0.13%
Q (m³/s)	0.167	4.36E-05	1.53E-03	1.53E-03	3.29E-02	1.83%
d (m)	0.010	0	5.08E-05	5.08E-05	9.33E-03	0.52%
Rotation (°)	0	0	5	5	6.82E-03	0.38%
Perpendicularity (°)	0	0	5	5	6.82E-03	0.38%
Linear Regression Uncertainty	N/A	3.46E-03	0	3.46E-03	3.46E-03	0.19%
Temperature Uncertainty (g)	N/A	0	3.27E-02	3.27E-02	7.72E-03	0.43%
Sensor Drift (g)	N/A	0	1.08E-03	1.08E-03	2.54E-04	0.01%

Table D.5. Experimental Uncertainty Contributions to the Drag Coefficient for an Inline Seven Row Array with S1/d = 4 and S2/d = 3.46 at the Low Reynolds number.

Variable	Value	Precision Uncertainty	Bias Uncertainty	Total Uncertainty	u_{CD}	% C_D
C_D	1.55	0.024	0.114	0.117	**0.117**	**7.55%**
V_{cx}/V_{ex}	3.00E-04	7.231E-07	0	7.23E-07	3.73E-03	0.24%
d_x (V/V-kg-cm)	0.11	0	1.16E-03	1.16E-03	1.56E-02	1.01%
δ (cm)	-0.19	0	1.27E-02	1.27E-02	7.20E-03	0.47%
W (m)	0.61	0	7.94E-04	7.94E-04	4.03E-03	0.26%
H (m)	9.60E-03	0	2.54E-04	2.54E-04	4.09E-02	2.65%
ρ (kg/m³)	1.13	3.58E-05	1.45E-03	1.45E-03	1.98E-03	0.13%
Q (m³/s)	0.063	2.11E-05	2.12E-03	2.12E-03	1.05E-01	6.76%
d (m)	0.010	0	5.08E-05	5.08E-05	8.05E-03	0.52%
Rotation (°)	0	0	5	5	5.88E-03	0.38%
Perpendicularity (°)	0	0	5	5	5.88E-03	0.38%
Linear Regression Uncertainty	N/A	2.32E-02	0	2.32E-02	2.32E-02	1.50%
Temperature Uncertainty (g)	N/A	0	1.97E-03	1.97E-03	3.17E-03	0.21%
Sensor Drift (g)	N/A	0	1.08E-03	1.08E-03	1.73E-03	0.11%

Table D.6. Experimental Uncertainty Contributions to the Drag Coefficient for an Inline Seven Row Array with S1/d = 4 and S2/d = 3.46 at the High Reynolds number.

Variable	Value	Precision Uncertainty	Bias Uncertainty	Total Uncertainty	u_{CD}	% C_D
C_D	1.49	0.005	0.052	0.052	**0.052**	**3.51%**
V_{cx}/V_{ex}	2.04E-03	4.300E-06	0	4.30E-06	3.15E-03	0.21%
d_x (V/V-kg-cm)	0.11	0	1.16E-03	1.16E-03	1.51E-02	1.01%
δ (cm)	-0.19	0	1.27E-02	1.27E-02	6.96E-03	0.47%
W (m)	0.61	0	7.94E-04	7.94E-04	3.89E-03	0.26%
H (m)	9.60E-03	0	2.54E-04	2.54E-04	3.95E-02	2.65%
ρ (kg/m³)	1.08	6.38E-05	1.37E-03	1.38E-03	1.90E-03	0.13%
Q (m³/s)	0.170	4.39E-05	1.55E-03	1.55E-03	2.72E-02	1.82%
d (m)	0.010	0	5.08E-05	5.08E-05	7.78E-03	0.52%
Rotation (°)	0	0	5	5	5.69E-03	0.38%
Perpendicularity (°)	0	0	5	5	5.69E-03	0.38%
Linear Regression Uncertainty	N/A	3.34E-03	0	3.34E-03	3.34E-03	0.22%
Temperature Uncertainty (g)	N/A	0	1.42E-02	1.42E-02	3.25E-03	0.22%
Sensor Drift (g)	N/A	0	1.08E-03	1.08E-03	2.46E-04	0.02%

Uncertainty for Lift Coefficient, C_L

$$C_L = \frac{2*g*H*W^2*{V_{cy}}/{V_{ey}}}{d_y*d*Q^2*(2.54-\delta)\rho}$$

$$u_{CL} = \sqrt{\left(\frac{\partial C_L}{\partial\left(\frac{V_{cy}}{V_{ey}}\right)}u_{V_{cy}/V_{ey}}\right)^2 + \left(\frac{\partial C_L}{\partial(d_y)}u_{d_y}\right)^2 + \left(\frac{\partial C_L}{\partial(\delta)}u_{\delta}\right)^2 + \left(\frac{\partial C_L}{\partial(W)}u_W\right)^2 + \left(\frac{\partial C_L}{\partial(H)}u_H\right)^2 + \left(\frac{\partial C_L}{\partial(\rho)}u_{\rho}\right)^2 + \ldots}$$
$$\sqrt{\ldots + \left(\frac{\partial C_L}{\partial(Q)}u_Q\right)^2 + \left(\frac{\partial C_L}{\partial(d)}u_d\right)^2 + u_{Rotation}^2 + u_{Perpendicularity}^2 + u_{Linear,\mathrm{Re}gression}^2 + u_{Temperature}^2 + u_{Drift}^2}$$

Volumetric Flow Rate

$$Q = \left(\frac{\rho_{STD}}{\rho}\right)\frac{5.9816*\left(D^2\right)*K*Y\sqrt{dp}*\sqrt{\frac{2.703*P_L}{460+T_L}}}{\frac{2.703*14.7}{460+60}} * \frac{4.71936*10^{-4}\mathrm{m^3/sec}}{1\,\mathrm{CFM}}$$

$$u_Q = \sqrt{\left[\frac{\partial Q}{\partial(dp)}*u_{dp}\right]^2 + \left[\frac{\partial Q}{\partial(T_L)}*u_{TL}\right]^2 + \left[\frac{\partial Q}{\partial(P_L)}*u_{PL}\right]^2 + u_{meter}^2}$$

Sensor Voltage Ratio

$$\frac{V_{cy}}{V_{ex}} = \frac{\left(V_{oy}-V_{zero,y}\right)}{V_{ey}} - \psi\frac{\left(V_{ox}-V_{zero,x}\right)}{V_{ex}}$$

$$u_{\frac{V_{cy}}{V_{ey}}} = \sqrt{\left[\frac{\partial\left(\frac{V_{cy}}{V_{ey}}\right)}{\partial\left(V_{oy}\right)}*u_{V_{ox}}\right]^2 + \left[\frac{\partial\left(\frac{V_{cy}}{V_{ey}}\right)}{\partial\left(V_{ey}\right)}*u_{V_{ey}}\right]^2 + \left[\frac{\partial\left(\frac{V_{cy}}{V_{ey}}\right)}{\partial\left(V_{zero,y}\right)}*u_{V_{zero,y}}\right]^2 + \left[\frac{\partial\left(\frac{V_{cy}}{V_{ey}}\right)}{\partial(\psi)}*u_{\psi}\right]^2 + \ldots}$$
$$\sqrt{\left[\frac{\partial\left(\frac{V_{cy}}{V_{ey}}\right)}{\partial\left(V_{ox}\right)}*u_{V_{ox}}\right]^2 + \left[\frac{\partial\left(\frac{V_{cy}}{V_{ey}}\right)}{\partial\left(V_{ex}\right)}*u_{V_{ex}}\right]^2 + \left[\frac{\partial\left(\frac{V_{cy}}{V_{ey}}\right)}{\partial\left(V_{zero,x}\right)}*u_{V_{zero,x}}\right]^2}$$

Table D.7. Experimental Uncertainty Contributions to the Lift Coefficient for an Inline Seven Row Array with S1/d = 4 and S2/d = 3.46 at the Low Reynolds number.

Variable	Value	Precision Uncertainty	Bias Uncertainty	Total Uncertainty	u_{CL}	% C_L
C_L	0.71	0.013	0.053	0.054	**0.054**	**7.64%**
V_{cy}/V_{ey}	1.34E-04	6.586E-07	0	6.59E-07	3.50E-03	0.49%
d_y (V/V-kg-cm)	0.11	0	1.12E-03	1.12E-03	7.21E-03	1.01%
δ (cm)	-0.19	0	1.27E-02	1.27E-02	3.32E-03	0.47%
W (m)	0.61	0	7.94E-04	7.94E-04	1.86E-03	0.26%
H (m)	9.60E-03	0	2.54E-04	2.54E-04	1.89E-02	2.65%
ρ (kg/m³)	1.13	3.58E-05	1.45E-03	1.45E-03	9.13E-04	0.13%
Q (m³/s)	0.063	2.11E-05	2.12E-03	2.12E-03	4.82E-02	6.76%
d (m)	0.010	0	5.08E-05	5.08E-05	3.71E-03	0.52%
Rotation (°)	0	0	5	5	2.71E-03	0.38%
Perpendicularity (°)	0	0	5	5	2.71E-03	0.38%
Linear Regression Uncertainty	N/A	1.28E-02	0	1.28E-02	1.28E-02	1.80%
Temperature Uncertainty (g)	N/A	0	2.03E-03	2.03E-03	3.27E-03	0.46%
Sensor Drift (g)	N/A	0	1.11E-03	1.11E-03	1.78E-03	0.25%

Table D.8. Experimental Uncertainty Contributions to the Lift Coefficient for an Inline Seven Row Array with S1/d = 4 and S2/d = 3.46 at the High Reynolds number.

Variable	Value	Precision Uncertainty	Bias Uncertainty	Total Uncertainty	u_{CL}	% C_L
C_L	0.61	0.004	0.022	0.022	**0.022**	**3.58%**
V_{cy}/V_{ey}	8.09E-04	4.218E-06	0	4.22E-06	3.18E-03	0.52%
d_y (V/V-kg-cm)	0.11	0	1.12E-03	1.12E-03	6.17E-03	1.01%
δ (cm)	-0.19	0	1.27E-02	1.27E-02	2.84E-03	0.47%
W (m)	0.61	0	7.94E-04	7.94E-04	1.59E-03	0.26%
H (m)	9.60E-03	0	2.54E-04	2.54E-04	1.61E-02	2.65%
ρ (kg/m³)	1.08	6.38E-05	1.37E-03	1.38E-03	7.75E-04	0.13%
Q (m³/s)	0.170	4.39E-05	1.55E-03	1.55E-03	1.11E-02	1.82%
d (m)	0.010	0	5.08E-05	5.08E-05	3.18E-03	0.52%
Rotation (°)	0	0	5	5	2.32E-03	0.38%
Perpendicularity (°)	0	0	5	5	2.32E-03	0.38%
Linear Regression Uncertainty	N/A	1.82E-03	0	1.82E-03	1.82E-03	0.30%
Temperature Uncertainty (g)	N/A	0	1.47E-02	1.47E-02	3.35E-03	0.55%
Sensor Drift (g)	N/A	0	1.11E-03	1.11E-03	2.53E-04	0.04%

Uncertainty for Array Friction Factor, f_{array}

$$f_{array} = \frac{\frac{1}{2}(W - N_{pin}d_{pin} - d)^2\left(H^3W^3\Delta P_{measured} - \frac{1}{4}fWL\rho Q^2 - \frac{1}{4}fHL\rho Q^2\right)}{\rho * H * N * Q^2 * W^3}$$

$$u_{f_{array}} = \sqrt{\begin{aligned}&\left(\frac{\partial f_{array}}{\partial \rho}u_\rho\right)^2 + \left(\frac{\partial f_{array}}{\partial Q}u_Q\right)^2 + \left(\frac{\partial f_{array}}{\partial W}u_W\right)^2 + \left(\frac{\partial f_{array}}{\partial H}u_H\right)^2 + \left(\frac{\partial f_{array}}{\partial d}u_d\right)^2 + \left(\frac{\partial f_{array}}{\partial d_{pin}}u_{d_{pin}}\right)^2 + \ldots \\ &\ldots + \left(\frac{\partial f_{array}}{\partial f}u_f\right)^2 + \left(\frac{\partial f_{array}}{\partial \Delta P_{measured}}u_{\Delta P_{measured}}\right)^2 + \left(\frac{\partial f_{array}}{\partial L}u_L\right)^2\end{aligned}}$$

Volumetric Flow Rate

$$Q = \left(\frac{\rho_{STD}}{\rho}\right)\frac{5.9816 * \left(D^2\right) * K * Y\sqrt{dp} * \sqrt{\frac{2.703 * P_L}{460 + T_L}}}{\frac{2.703 * 14.7}{460 + 60}} * \frac{4.71936 * 10^{-4}\,\text{m}^3/\text{sec}}{1\,\text{CFM}}$$

$$u_Q = \sqrt{\left[\frac{\partial Q}{\partial(dp)} * u_{dp}\right]^2 + \left[\frac{\partial Q}{\partial(T_L)} * u_{TL}\right]^2 + \left[\frac{\partial Q}{\partial(P_L)} * u_{PL}\right]^2 + u_{meter}^2}$$

Measured Pressure Drop

$$\Delta P_{measured} = \Delta P_{downstream} - \Delta P_{upstream}$$

$$u_{\Delta P_{measured}} = \sqrt{\left[\frac{\partial \Delta P_{measured}}{\partial\left(\Delta P_{upstream}\right)} * u_{\Delta P_{upstream}}\right]^2 + \left[\frac{\partial \Delta P_{measured}}{\partial\left(\Delta P_{downstream}\right)} * u_{\Delta P_{downstream}}\right]^2}$$

Turbulent Flow Darcy Friction Factor Correlations for Rectangular Duct

$$f = \frac{4 * 0.1268}{\text{Re}^{0.3}} \quad \text{for } 5.0 \text{ X } 10^3 \leq \text{Re} \leq 3.0 \text{ X } 10^4$$

$$f = \frac{4 * 0.0868}{\text{Re}^{0.25}} \quad \text{for } 1.2 \text{ X } 10^4 \leq \text{Re} \leq 1.2 \text{ X } 10^6$$

$$u_f = \sqrt{\left[\frac{\partial f}{\partial(\text{Re})} * u_{\text{Re}}\right]^2}$$

Table D.9. Experimental Uncertainty Contributions to the Array Friction Factor for a Single Row Array with S1/d = 2 at the Low Reynolds number.

Variable	Value	Precision Uncertainty	Bias Uncertainty	Total Uncertainty	u_{farray}	% f_{array}
f_{array}	0.11	1.73E-04	0.022	0.022	**0.022**	**20.74%**
W (m)	0.61	0	7.94E-04	7.94E-04	6.41E-04	0.60%
H (m)	9.60E-03	0	2.54E-04	2.54E-04	8.25E-03	7.77%
ρ (kg/m³)	1.13	4.35E-05	1.46E-03	1.46E-03	1.80E-04	0.17%
Q (m³/s)	0.038	2.38E-05	2.80E-03	2.80E-03	2.04E-02	19.17%
d (m)	0.010	0	5.08E-05	5.08E-05	3.06E-05	0.03%
d_{pins} (m)	0.010	0	2.54E-06	2.54E-06	4.74E-05	0.04%
L (m)	0.292	0	1.27E-02	1.27E-02	1.45E-03	1.37%
$\Delta P_{measured}$ (Pa)	54.238	0.084	4.40E+00	4.55E+00	6.03E-05	0.06%
f	0.035	0	-1.04E-04	1.04E-04	1.00E-04	0.09%

Table D.10. Experimental Uncertainty Contributions to the Array Friction Factor for a Single Row Array with S1/d = 2 at the High Reynolds number.

Variable	Value	Precision Uncertainty	Bias Uncertainty	Total Uncertainty	u_{farray}	% f_{array}
f_{array}	0.11	6.20E-05	0.008	0.008	**0.008**	**7.56%**
W (m)	0.61	0	7.94E-04	7.94E-04	6.29E-04	0.58%
H (m)	9.60E-03	0	2.54E-04	2.54E-04	7.69E-03	7.10%
ρ (kg/m³)	1.11	1.19E-04	1.42E-03	1.42E-03	1.71E-04	0.16%
Q (m³/s)	0.166	3.73E-05	1.51E-03	1.51E-03	2.43E-03	2.24%
d (m)	0.010	0	5.08E-05	5.08E-05	3.12E-05	0.03%
d_{pins} (m)	0.010	0	2.54E-06	2.54E-06	4.84E-05	0.04%
L (m)	0.292	0	1.27E-02	1.27E-02	1.08E-03	1.00%
$\Delta P_{measured}$ (Pa)	948.039	8.29	4.40E+00	9.38E+00	7.02E-06	0.01%
f	0.026	0	-6.46E-04	6.46E-04	6.23E-04	0.57%

Table D.11. Experimental Uncertainty Contributions to the Array Friction Factor for a Seven Row Array with S1/d = 4 and S2/d = 3.46 at the Low Reynolds number.

Variable	Value	Precision Uncertainty	Bias Uncertainty	Total Uncertainty	u_{farray}	% f_{array}
f_{array}	0.07	8.11E-05	0.011	0.011	**0.011**	**15.13%**
W (m)	0.61	0	7.94E-04	7.94E-04	2.89E-04	0.41%
H (m)	9.60E-03	0	2.54E-04	2.54E-04	5.01E-03	7.04%
ρ (kg/m³)	1.11	2.99E-05	1.40E-03	1.40E-03	1.10E-04	0.15%
Q (m³/s)	0.051	2.38E-05	2.80E-03	2.80E-03	9.52E-03	13.37%
d (m)	0.010	0	5.08E-05	5.08E-05	1.43E-05	0.02%
d_{pins} (m)	0.010	0	2.54E-06	2.54E-06	1.07E-05	0.02%
L (m)	0.455	0	1.27E-02	1.27E-02	4.31E-04	0.61%
$\Delta P_{measured}$ (Pa)	183.809	1.18	4.40E+00	4.55E+00	1.50E-06	0.00%
f	0.032	0	-9.61E-05	9.61E-05	4.64E-05	0.07%

Table D.12. Experimental Uncertainty Contributions to the Array Friction Factor for a Seven Row Array with S1/d = 4 and S2/d = 3.46 at the High Reynolds number.

Variable	Value	Precision Uncertainty	Bias Uncertainty	Total Uncertainty	u_{farray}	% f_{array}
f_{array}	0.06	3.99E-05	0.005	0.005	**0.005**	**7.24%**
W (m)	0.61	0	7.94E-04	7.94E-04	2.54E-04	0.40%
H (m)	9.60E-03	0	2.54E-04	2.54E-04	4.35E-03	6.85%
ρ (kg/m³)	1.09	7.34E-05	1.39E-03	1.40E-03	9.70E-05	0.15%
Q (m³/s)	0.167	4.35E-05	1.53E-03	1.53E-03	1.40E-03	2.20%
d (m)	0.010	0	5.08E-05	5.08E-05	1.25E-05	0.02%
d_{pins} (m)	0.010	0	2.54E-06	2.54E-06	9.39E-06	0.01%
L (m)	0.455	0	1.27E-02	3.49E-04	5.49E-03	0.55%
$\Delta P_{measured}$ (Pa)	1692.436	10.41	4.40E+00	3.54E-07	5.57E-06	0.00%
f	0.026	0	-6.47E-04	3.12E-04	4.91E-03	0.49%

Uncertainty for Channel Reynolds Number, Re

$$\mathrm{Re} = \frac{2\rho Q}{\mu(W+H)}$$

$$u_{\mathrm{Re}} = \sqrt{\left(\frac{\partial \mathrm{Re}}{\partial \rho}u_\rho\right)^2 + \left(\frac{\partial \mathrm{Re}}{\partial Q}u_Q\right)^2 + \left(\frac{\partial \mathrm{Re}}{\partial \mu}u_\mu\right)^2 + \left(\frac{\partial \mathrm{Re}}{\partial W}u_W\right)^2 + \left(\frac{\partial \mathrm{Re}}{\partial H}u_H\right)^2}$$

Volumetric Flow Rate

$$Q = \left(\frac{\rho_{STD}}{\rho}\right)\frac{5.9816*\left(D^2\right)*K*Y\sqrt{dp}*\sqrt{\frac{2.703*P_L}{460+T_L}}}{\frac{2.703*14.7}{460+60}} * \frac{4.71936*10^{-4}\mathrm{m^3/sec}}{1\,\mathrm{CFM}}$$

$$u_Q = \sqrt{\left[\frac{\partial Q}{\partial(dp)}*u_{dp}\right]^2 + \left[\frac{\partial Q}{\partial(T_L)}*u_{TL}\right]^2 + \left[\frac{\partial Q}{\partial(P_L)}*u_{PL}\right]^2 + u_{meter}^2}$$

Table D.13. Experimental Uncertainty Contributions to the Low Channel Reynolds number.

Variable	Value	Precision Uncertainty	Bias Uncertainty	Total Uncertainty	u_{Re}	% Re
Re	9313	4.65	544.18	544.20	**544.20**	**5.84%**
W (m)	0.61	0	7.94E-04	7.94E-04	1.19E+01	0.13%
H (m)	9.60E-03	0	2.54E-04	2.54E-04	3.82E+00	0.04%
ρ (kg/m³)	1.10	3.63E-05	1.40E-03	1.40E-03	1.18E+01	0.13%
Q (m³/s)	0.048	2.39E-05	2.80E-03	2.80E-03	5.44E+02	5.84%

Table D.14. Experimental Uncertainty Contributions to the High Channel Reynolds number.

Variable	Value	Precision Uncertainty	Bias Uncertainty	Total Uncertainty	u_{Re}	% Re
Re	32129	8.49	300.54	300.66	**300.66**	**0.94%**
W (m)	0.61	0	7.94E-04	7.94E-04	4.12E+01	0.13%
H (m)	9.60E-03	0	2.54E-04	2.54E-04	1.32E+01	0.04%
ρ (kg/m³)	1.09	4.61E-05	1.39E-03	1.39E-03	4.10E+01	0.13%
Q (m³/s)	0.167	4.36E-05	1.53E-03	1.53E-03	2.95E+02	0.92%

Uncertainty for Pin Reynolds Number, Re_d

$$\mathrm{Re}_d = \frac{\rho * Q * d}{H * \mu * \left(W - N_{pins} d_{pins} - d\right)}$$

$$u_{\mathrm{Re}_d} = \sqrt{\left(\frac{\partial \mathrm{Re}_d}{\partial \rho} u_\rho\right)^2 + \left(\frac{\partial \mathrm{Re}_d}{\partial Q} u_Q\right)^2 + \left(\frac{\partial \mathrm{Re}_d}{\partial \mu} u_\mu\right)^2 + \left(\frac{\partial \mathrm{Re}_d}{\partial W} u_W\right)^2 + \left(\frac{\partial \mathrm{Re}_d}{\partial H} u_H\right)^2 + \ldots + \left(\frac{\partial \mathrm{Re}_d}{\partial d} u_d\right)^2 + \left(\frac{\partial \mathrm{Re}_d}{\partial d_{pin}} u_{d_{pin}}\right)^2}$$

Volumetric Flow Rate

$$Q = \left(\frac{\rho_{STD}}{\rho}\right) \frac{5.9816 * \left(D^2\right) * K * Y \sqrt{dp} * \sqrt{\frac{2.703 * P_L}{460 + T_L}}}{\frac{2.703 * 14.7}{460 + 60}} * \frac{4.71936 * 10^{-4} \mathrm{m^3/sec}}{1\,\mathrm{CFM}}$$

$$u_Q = \sqrt{\left[\frac{\partial Q}{\partial (dp)} * u_{dp}\right]^2 + \left[\frac{\partial Q}{\partial (T_L)} * u_{TL}\right]^2 + \left[\frac{\partial Q}{\partial (P_L)} * u_{PL}\right]^2 + u_{meter}^2}$$

Table D.15. Experimental Uncertainty Contributions to the Low Pin Reynolds number.

Variable	Value	Precision Uncertainty	Bias Uncertainty	Total Uncertainty	u_{Red}	% Re_d
Re_d	6410	3.19	412.61	412.62	**412.62**	**6.44%**
W (m)	0.61	0	7.94E-04	7.94E-04	1.11E+01	0.17%
H (m)	9.60E-03	0	2.54E-04	2.54E-04	1.70E+02	2.65%
ρ (kg/m³)	1.10	3.63E-05	1.40E-03	1.40E-03	8.13E+00	0.13%
Q (m³/s)	0.048	2.38E-05	2.80E-03	2.80E-03	3.74E+02	5.84%
d (m)	0.010	0	5.08E-05	5.08E-05	3.41E+01	0.53%
d_{pins} (m)	0.010	0	2.54E-06	2.54E-06	5.34E-01	0.01%

Table D.16. Experimental Uncertainty Contributions to the High Pin Reynolds number.

Variable	Value	Precision Uncertainty	Bias Uncertainty	Total Uncertainty	u_{Red}	% Re_d
Re_d	22113	5.83	632.01	632.04	**632.04**	**2.86%**
W (m)	0.61	0	7.94E-04	7.94E-04	3.84E+01	0.17%
H (m)	9.60E-03	0	2.54E-04	2.54E-04	5.85E+02	2.65%
ρ (kg/m³)	1.09	4.61E-05	1.39E-03	1.39E-03	2.82E+01	0.13%
Q (m³/s)	0.167	4.35E-05	1.53E-03	1.53E-03	2.03E+02	0.92%
d (m)	0.010	0	5.08E-05	5.08E-05	1.18E+02	0.53%
d_{pins} (m)	0.010	0	2.54E-06	2.54E-06	1.84E+00	0.01%